Quantum phase transitions and fluctuations in space charge doped one unit-cell Bi2Sr2CaCu2O8+x

Fang Wang

Fang Wang. Quantum phase transitions and fluctuations in space charge doped one unit-cell Bi2Sr2CaCu2O8+x. Superconductivity [cond-mat.supr-con]. Sorbonne Université, 2021. English. NNT : 2021SORUS436 . tel-03783515

HAL Id: tel-03783515
https://theses.hal.science/tel-03783515v1

Submitted on 22 Sep 2022

Sorbonne Université

École doctorale 397 - Physique et Chimie des Matériaux

Institut de minéralogie, de physique des matériaux et de cosmochimie

Quantum phase transitions and fluctuations in space charge doped one unit-cell $Bi_2Sr_2CaCu_2O_{8+x}$

Par Fang WANG
Thèse de doctorat de Physique

Dirigée par Abhay SHUKLA

Présentée et soutenue publiquement le 10/09/2021

Devant un jury composé de :

Mme. BROUET Véronique	Paris-Saclay Université	Rapportrice
M. RENNER Christophe	University of Geneva	Rapporteur
Mme. LERIDON Brigitte	ESPCI Paris	Examinatrice
M. CIVELLI Marcello	Paris-Saclay Université	Examinateur
M. SHUKLA Abhay	Sorbonne Université	Directeur de thèse
M. BISCARAS Johan	Sorbonne Université	Co-encadrant, invité

Acknowledgement

First of all, I would like to thank my supervisor professor Abhay Shukla for providing me the chance of studying in our lab as an intern during my master study in UPMC and then as a Ph.D student. I feel really gratitude to work with such a nice professor, who can always provide me with considerate suggestions. Even during the confinement, which I think is the most difficult part of the work, he is always positive and enthusiastic, and gives us a lot of encouragement. He is like a patriarch of the group, and treat everyone like a child with great patience.

I want to thank Johan Biscaras, my associate professor, who is very capable and genius. He knows everything about the instruments, the programs and the theories of our work. He always explains everything with patience. It's my pleasure to work with and learn from him. And of course, it's also my great pleasure to drink beer with him in the bar outside our university. I found that he is lovely in his heart when I saw the cats cartoon pasted on the wall behind his chair, even though he would be angry with us when we broke things in the lab.

I want to thank the group members, even though a lot of them has graduated and left the lab. Dr. Edoardo Sterpetti has taught me everything he knows about BSCCO, and he told me always use the best thing in the lab for BSCCO, which is absolutely a good idea. Dr. Ali Fakih, Dr. Onkar Shinder and Hugo Kowalczyk, who have encouraged me a lot when sometimes I'm low in mood. Dr. Wenyi WU, who comes from the same country as me. Johan usually stops us when we talk in chinese. Even though, we have talked a lot in chinese. And he's going to be a father, I wish him a very happy life with his family.

I want to thank the China Scholarship Council (CSC) for supporting my four years of study and life in France, and thanks also to the distribution of goods during the COVID confinement.

I also want to thank the "association des boursiers CSC en ile de France", where I have made a lot of friends. We have participated in a lot of activities and had a pretty good time.

I want to thank my cute two cats, who have accompany me for two and three years respectively. I hope both of them can have a happy cat life with me.

I want to thank my boyfriend, who has been playing mobile games with me. He has taken me for a lot of beautiful trips in Europe. And life becomes much more interesting with him.

I want to thank my parents who always show respect to my choice, even though I, myself, don't know if the choice is right or wrong. Hope they can be happy forever.

Abstract

English Version

The superconductor-insulator transition in two dimensions is a continuous quantum phase transition at absolute zero temperature driven by external parameters like disorder, magnetic field, or carrier concentration. Such transitions have been induced in a variety of two dimensional superconductors by tuning different external parameters and studied with a finite-size scaling analysis. There is however not much uniformity in the findings as both the superconducting systems and the tuning parameters are diverse. In this thesis, we first fabricated high quality of one unit-cell BSCCO-2212 samples with anodic bonding technique, an original method of exfoliation developed in our laboratory for preparing high quality 2D crystals from layered bulk materials. Then we revealed the superconductor-insulator transition in the fabricated one unit-cell $Bi_{2.1}Sr_{1.9}CaCu_2O_{8+x}$ by space charge doping, which in an effective field effect electrostatic doping technique. We determined the related critical parameters and develop a reliable way to estimate doping in the non-superconducting region, a crucial and central problem in these materials. Finite-size scaling analysis yields a critical doping of 0.057 holes/Cu, a critical resistance of ~ 6.85 kΩ and a scaling exponent product $\nu z \sim 1.57$. These results, together with earlier work in other materials, provide a coherent picture of the superconductor-insulator transition and its bosonic nature in the underdoped regime of emerging superconductivity in high critical temperature superconductors.

Then in the latter part of this thesis, we also investigated the effects of inhomogeneity and fluctuations on superconducting transition on mesoscopic and nanoscopic scale both with simulation and with simulations and with analysis of transport measurements. The use of an ultra-thin sample also facilitates analysis on two fronts. Firstly, in two dimensions fluctuation phenomena related to the superconducting transition are exacerbated, making the analysis of changes in widths easier. Secondly aspects related to percolation and clustering can be easily simulated and compared with analytical models. Especially, the effects of fluctuations on the overdoped and underdoped side of the phase diagram of one unit-cell BSCCO-2212 are discussed. We discovered that the fluctuation regime in the underdoped part of the phase diagram is fundamentally different from that in the part where $p > 0.19$. We discussed the possible behaviour of cooper pairs related to our experimental results, as well as one existing theoretical explanation (BEC-BCS transition).

Version française

La transition supraconducteur-isolant en deux dimensions est une transition de phase quantique continue à la température du zéro absolu provoquée par des paramètres externes tels que le désordre, le champ magnétique ou la concentration de porteurs. De telles transitions ont été induites dans une variété de supraconducteurs bidimensionnels en ajustant différents paramètres externes et étudiées avec une analyse de renormalization de taille finie. Il y a cependant assez peu d'uniformité dans les résultats car à la fois les systèmes supraconducteurs et les paramètres externes sont divers. Dans cette thèse, nous avons d'abord fabriqué des échantillons BSCCO-2212 d'épaisseur d'une cellule unité et de grande qualité avec la technique de collage anodique, une méthode originale d'exfoliation développée dans notre laboratoire pour préparer des cristaux 2D de haute qualité à partir de matériaux lamellaires massifs. Ensuite, nous avons provoqué la transition supraconducteur-isolant dans les échantillons fabriqués de $\mathrm{Bi}_{2.1}\mathrm{Sr}_{1.9}\mathrm{CaCu}_2\mathrm{O}_{8+x}$ monocouche par dopage par charge d'espace, qui est une technique efficace de dopage électrostatique à effet de champ. Nous avons déterminé les paramètres critiques associés et développé un moyen fiable d'estimer le dopage dans la région non supraconductrice, un problème crucial et central dans ces matériaux. L'analyse par renormalisation de taille finie donne un dopage critique de 0,057 trous/Cu, une résistance critique de ~ 6.85 kΩ et un produit d'exposant critiques $\nu z \sim 1{,}57$. Ces résultats, ainsi que des travaux antérieurs sur d'autres matériaux, fournissent une image cohérente de la transition supraconducteur-isolant et de sa nature bosonique dans le régime sous-dopé de la supraconductivité émergente dans les supraconducteurs à haute température critique.

Ensuite, dans la dernière partie de cette thèse, nous avons également étudié les effets de l'inhomogénéité et des fluctuations sur la transition supraconductrice à l'échelle mésoscopique et nanoscopique à la fois avec des simulations et des mesures de transport. L'utilisation d'un échantillon ultra-mince facilite également l'analyse sur deux fronts. Tout d'abord, en deux dimensions, les phénomènes de fluctuation liés à la transition supraconductrice sont exacerbés, facilitant l'analyse des changements de largeurs. Deuxièmement, les aspects liés à la percolation et au clustering peuvent être facilement simulés et comparés à des modèles analytiques. En particulier, les effets des fluctuations sur le côté surdopé et sous-dopé du diagramme de phase d'une monocouche de BSCCO-2212 sont discutés. Nous avons découvert que le régime de fluctuation dans la partie sous-dopée du diagramme de phase est fondamentalement différent de celui dans la partie où $p > 0{,}19$. Nous avons discuté du comportement possible des paires de Cooper liées à nos résultats expérimentaux, ainsi que d'une des théories pouvant l'expliquer (transition BEC-BCS).

Résumé

Les cuprates supraconducteurs à haute température ont été découverts pour la première fois en 1986 et font depuis l'objet d'intenses recherches. Le diagramme de phase riche et complexe de ces oxydes a déclenché une pléthore de travaux expérimentaux et théoriques visant à dévoiler le mécanisme de la supraconductivité à haute température. Malgré tous ces efforts, un consensus scientifique n'a pas encore été établi, notamment concernant le mécanisme d'appariement supraconducteur, et sa relation avec l'insaisissable pseudo-gap dans la partie sous-dopé du diagramme de phase. Dans cette thèse, nous revisitons ces questions dans la limite bidimensionnelle en exploitant la nature lamellaire du cuprate $\mathrm{Bi_{2.1}Sr_{1.9}CaCu_2O_{8+x}}$ et en utilisant une technique originale de dopage électrostatique à haute densité de porteurs. Nous décrivons d'abord la transition supraconducteur-isolant du côté extrêmement sous-dopé du diagramme de phase. Ensuite, nous utilisons des expériences et des simulations pour discuter de l'effet des fluctuations et des inhomogénéités dans ce matériau 2D.

La transition supraconducteur-isolant en deux dimensions est une transition de phase quantique continue à la température du zéro absolu provoquée par des paramètres externes tels que le désordre, le champ magnétique ou la concentration de porteurs. De telles transitions ont été induites dans une variété de supraconducteurs bidimensionnels en ajustant différents paramètres externes et étudiées avec une analyse de renormalisation de taille finie. Il y a cependant assez peu d'uniformité dans les résultats car à la fois les systèmes supraconducteurs et les paramètres externes sont divers. Le contrôle de la densité des porteurs est un moyen efficace de réaliser cette transition par des méthodes de dopage chimique ou électrostatique. Le dopage chimique, la méthode habituelle et la seule possible dans les échantillons massifs, a été largement utilisé dans les supraconducteurs à haute température critique, à la fois en matériaux massifs et en chouche mince. Cependant, cela dépend de l'échantillon et peut entraîner du désordre et des changements de structure. Le dopage électrostatique est la méthode de choix pour obtenir un résultat continu et sans défaut de dopage dans un même échantillon ultra-mince à l'aide d'un dispositif de type transistor à effet de champ. La longueur de corrélation ϵ et le temps de corrélation τ, correspondant à une transition de phase, dépendent de la variation d'un

paramètre externe x par rapport à un valeur x_c. Dans notre cas, il s'agit de la variation de la concentration en porteurs p par rapport au dopage critique à la phase transition p_c avec, $\epsilon \propto |p - p_c|^{-\nu}$ et $\tau \propto \epsilon^z$ où ν est l'exposant de longueur de corrélation et z est l'exposant de corrélation dynamique. La variation de grandeurs physiques comme la résistance de surface à travers la transition de phase dans une mesure de transport peut être exprimée en termes de ces formes asymptotiques et d'une seule ≪ loi d'échelle ≫ dépendant de $|p - p_c|^{-\nu}$. Si les effets de la transition de phase quantique persistent à des températures expérimentalement accessibles, faibles mais non nulles, il peut être caractérisé par sa classe d'universalité donnée par la valeur numérique de νz, le produit des exposants à échelle finie. Cette valeur, ainsi que les valeurs critiques du paramètre moteur (dopage) et la grandeur physique mesurée (résistance de couche mince), constitue l'information fondamentale qui peut être glanée à partir de la transition de phase quantique en dimensions réduites.

Dans cette thèse, nous établissons et étudions la nature de la transition supraconducteur-isolant en fonction du dopage en $\mathrm{Bi_{2.1}Sr_{1.9}CaCu_2O_{8+x}}$ (BSCCO) monocouche par dopage par charge d'espace, qui est une technique efficace de dopage électrostatique à effet de champ. D'abord, Les précurseurs de BSCCO ont été exfoliés à partir de cristaux massifs, et déposé sur verre sodocalcique d'une épaisseur de 0,5 mm. Ensuite, la technique de collage anodique a été utilisée pour fabriquer des échantillons de BSCCO en chouche mince. Le précurseur sur le substrat de verre est placé entre deux électrodes et chauffé à ∼180 °C pour activer la mobilité de $\mathrm{Na^+}$. Lors de l'application d'une tension de grille négative (∼ 500 V) à l'arrière du substrat de verre, les ions $\mathrm{Na^+}$ dans le verre s'éloignent de l'interface verre-échantillon, formant une charge d'espace O_{2-} à l'interface échantillon-verre. Cet espace de charge colle électrostatiquement les premiers nanomètres du précurseur sur le substrat de verre. Du ruban adhésif est ensuite utilisé pour exfolier le précurseur. Un échantillon BSCCO ultramince de grande surface, dont l'épaisseur est évaluée par microscopie à force atomique et le contraste optique, est laissé sur la surface du verre. L'échantillon est ensuite recuit sous air à 350 °C pendant 1 min pour réduire son niveau de dopage par perte d'oxygène.

Alors, des contacts en or de soixante-dix nanomètres d'épaisseur ont été évaporés sur l'échantillon à travers un masque de type pochoir en acier pour obtenir un dispositif de géométrie van der Pauw après le processus de recuit. Nous avons découvert que les procédés de lithographie à base de résine ainsi que les couches d'accroche en chrome dégradent la qualité de l'échantillon. La qualité de l'échantillon et l'absence de contamination sont vérifiées par la mesure de la résistance de la couche ultramince. Le substrat de verre et le dispositif ont ensuite été collé sur une électrode de grille à l'arrière du substrat par de la laque d'argent. Sur un échantillon sous-dopé par perte d'oxygène, la résistance de la couche mince à quatre points mesurée à température ambiante a augmenté à 7 $\mathrm{k\Omega/\square^{-1}}$ contre 2 $\mathrm{k\Omega/\square^{-1}}$ mesurée dans des échantillons similaires préparés sans recuit. Le niveau de dopage a été contrôlé à l'intérieur d'un cryostat à vide poussé par dopage par charge d'espace. Au-dessus de la température ambiante (350-380 K), la mobilité des ions Na^+ à l'intérieur du substrat de verre est activée. En appliquant une tension de grille positive (ou négative) à l'arrière du substrat de verre, les ions Na^+ mobiles dérivent vers (ou loin de) l'interface échantillon-substrat, créant une charge positive (ou négative) et un dopage en électrons (ou en trous) correspondant dans l'échantillon. Le temps de dopage pour le passage entre deux niveaux de dopage variait de 10 à 110 min selon le niveaux de dopage initial et final. Cette charge d'espace est gelée lors du refroidissement à température ambiante ou en dessous par la perte de mobilité des ions Na^+. Dans certaines expériences antérieures, il a été démontré que les effets de dopage par liquide ioniques induisent une dérive de l'oxygène dans des échantillons et qu'il en résulte un dopage chimique, peut-être plus qu'un effet électrostatique. Dans les monochouches BSCCO fortement sous-dopé, ce mécanisme n'est pas probable en raison de l'absence d'oxygène faiblement lié ou interstitiel. De plus, la méthode de dopage par charge d'espace fonctionne aussi très bien dans les matériaux sans oxygène.

Le défi immédiat, complexe même dans les supraconducteurs massifs à haute température critique, est de déterminer le niveau de dopage. Dans un modèle simple à bande unique, le coefficient de Hall R_H et la charge élémentaire q donnent directement la concentration de porteurs de charge (de niveau de dopage) $p = 1/qR_H$. Les supraconducteurs à haute température critique ne peuvent certainement pas être classés comme tels et en effet R_H est anormalement dépendant de la température. Une autre estimation possible est le modèle classique de Drude où la conductivité est donnée par le produit de la charge élémentaire, de la mobilité et de la concentration en porteurs. Sur cette base, des tentatives ont été faites pour déterminer la concentration de porteurs en utilisant $p = S/R_S(T_f)$ où S est une constante déterminée empiriquement et $R_S(T_f)$ la résistance de couche mine à une température fixe bien au-dessus de T_c. La constante S est déterminée par le maximum du supraconducteur dôme qui est nominalement réglé à 0,16 trous/Cu. Cependant, la forme générique du dôme s'avère aplatie et asymétrique avec cette estimation pour monochouche de BSCCO, avec une supraconductivité commençant à un faible dopage de 0,028 et s'étirant au-dessus de $p = 0{,}3$, bien au-delà des limites du diagramme de phase générique. Nous concluons que cette estimation de charge dopée n'est pas satisfaisante.

Une autre approche souvent utilisée cherche à estimer les trous dopés (p) par atome de Cu avec une relation empirique $T_c(p)$ pour la région du dôme supraconducteur. $\frac{T_c}{T_{c(max)}} = 1 - 82.6(p - 0.16)^2$, où $T_c(p_{opt})$ est la température critique maximale mesurée correspondant au niveau de dopage optimal et Z est un facteur d'échelle déterminé empiriquement à 82,6. Dans cette approche, en accord avec le diagramme de phase générique, la supraconductivité existe dans la région $p \sim 0{,}05$ à $p \sim 0{,}27$ trous/Cu. La forme de dôme impliquée par cette relation est vérifiée expérimentalement, en particulier pour monochouche de BSCCO. Le problème dans notre cas est que le dopage doit être déterminé pour les régions non supraconductrices ainsi que supraconductrices. Pour surmonter cet obstacle, nous nous inspirons des approches plus simples décrites ci-dessus. Tout d'abord, nous remarquons que lorsque la T_c dans la région supraconductrice est tracée en fonction de la résistance de couche inverse à 200 K, une relation linéaire simple est trouvée. En extrapolant cette relation à la région non supraconductrice voisine, nous remplaçons T_c par $S/R_S(200K)$ dans la formule empirique où S est la valeur de la pente de cette dépendance linéaire. Nous avons ainsi une estimation cohérente et continue de p à travers la transition supraconducteur-isolant qui est compatible avec le diagramme de phase générique à haute T_c. Cette méthode devrait être applicable à d'autres matériaux à haute T_c. Pour BSCCO monocouche, la supraconductivité se développe selon cette estimation à un dopage critique de $p \sim$ 0,057, qui est compatible avec le diagramme de phase générique par construction et présente une variation douce avec un dopage optimal de 0,16 trous/Cu.

Avec ces observations importantes, nous pouvons commencer à rechercher l'existence de relations d'échelle possibles correspondant à une transition de phase quantique dans notre BSCCO monocouche dispositif à la transition supraconducteur-isolant. Cela implique que toutes les courbes de résistance de couche de notre BSCCO monocouche devrait se ramener à une seule fonction d'échelle de taille finie $R_S = R_c f(\mid x{-}xc \mid T^{-1/\nu z})$, où R_c est la résistance critique à la limite $x \rightarrow x_c$ et $T \rightarrow 0$. f est la fonction d'échelle universelle et x est le paramètre de contrôle, dans notre cas le niveau de dopage p. L'exposant de longueur de corrélation ν et l'exposant critique dynamique z, ainsi que la résistance critique R_c codent la nature de cette transition. Dans notre cas, l'analyse par renormalisation de taille finie donne un dopage critique de 0,057 trous/Cu, une résistance critique de $\sim$ 6.85 kΩ et un produit d'exposant critiques $\nu z \sim$ 1,57. Quelle est la nature de la transition supraconducteur-isolant trouvée ici ? L'état supraconducteur est caractérisé par un paramètre d'ordre complexe. Une transition de phase quantique continue est caractérisée par le changement continu de ce paramètre d'ordre à travers la transition (donnant lieu à des lois de puissance et d'échelle) et des fluctuations critiques de l'amplitude ou de la phase du paramètre d'ordre à la transition. Les fluctuations d'amplitude impliquent la rupture de l'appariement au-dessus de la température critique et la transformation des bosons de la paire de Cooper en fermions comme dans les supraconducteurs décrits par le scénario de Bardeen-Cooper-Schieffer (BCS). L'état du fermion peut être un métal ou même un isolant si dans cette dernière éventualité les fermions sont localisés par désordre ou interactions. Les fluctuations de phase dans les supraconducteurs sont généralement décrites dans le scénario Berezinskii-Kosterlitz-Thouless par la dualité entre les paires de Cooper et les vortex qui sont tous deux des bosons. Dans l'état supraconducteur, les tourbillons (associés aux ≪ glissements ≫ de phase et à la dissipation), sont liés par paires et localisés tandis que les paires de Cooper sont mobiles. La situation inverse prévaut au-dessus de la température critique et le système est isolant. Si cette dualité est parfaite, un argument simple établit le seuil critique de résistance entre les états supraconducteur et isolant à la résistance quantique avec charge de paire : $R_Q = h/(2e)^2 = 6,45\ k\Omega.\square^{-1}$. Cependant, des écarts par rapport à la dualité parfaite générés par la nature de l'interaction ou des facteurs tels que le désordre sont à prévoir. Ainsi, la mesure de la résistance critique et des exposants d'échelle finie de la transition de phase quantique continue peut nous renseigner sur la nature primordiale de l'état supraconducteur. Des modèles simples existent pour certains cas et sont utilisés pour définir la classe d'universalité, par exemple $\nu z = 4/3$ dans le modèle de percolation classique, 7/3 dans le modèle de percolation quantique (Steiner, M. A. et al. 2008) et 2/3 dans le modèle 3D XY (Li, Y.-H. et al. 1989). Notre résultat de $R_c = 6,85k\Omega \pm 0,10\ k\Omega$, qui est raisonnablement proche de R_Q trouvé dans LSCO (Bollinger, A. T. et al 2011), favorise l'image d'une transition entraînée par fluctuation de phase et une forte interaction d'appariement de couplage pour une supraconductivité à T_c élevée à la limite sous-dopée par opposition à la scénario de couplage faible dans les supraconducteurs BCS. On trouve $\nu z = 1,57 \pm 0,10$ pour le produit d'exposant à échelle finie décrivant la transition mesurée. Cela se compare à nouveau favorablement à la valeur de 1,5 dans LSCO (Bollinger, A. T. et al. 2011) et de 1,53 dans un dispositif BSCCO (Yu, Y. et al. 2019), ce qui implique la même classe d'universalité pour ces composés. Un point critique quantique devrait impliquer que les données aux températures les plus basses sont les plus indicatives de la physique en question, donc la mise à l'échelle des données à des températures plus élevées doit être traitée avec prudence. Tout comme les fluctuations quantiques critiques peuvent être effacés par les fluctuations thermiques, l'état fondamental peut également être éclipsé à des températures plus basses par des effets tels que la localisation faible. Cependant, la séparation claire dans nos données entre les régimes isolant et supraconducteur à la conductivité critique correspondant à $R_Q = h/(2e)^2$ fournit un support pour l'existence de la transition de phase quantique et du point critique.

De plus, les mesures de transport sont macroscopiques mais la transition supraconductrice dépend inévitablement des détails mésoscopiques et nanoscopiques. Les simulations de la transition supraconductrice, couplées à des mesures de transport, peuvent-elles permettre de comprendre les phénomènes se déroulant à ces échelles ? Pour répondre à cette question, nous nous sommes basés sur des mesures de la transition supraconductrice en fonction du dopage électrostatique dans des échantillons de BSCCO monochouche et l'analyse de la largeur et de la forme de cette transition. L'épaisseur de 3 nm permet un dopage électrostatique uniforme qui est un moyen pratique de provoquer un changement continu du dopage dans le même échantillon sans induire de défauts. L'utilisation d'un échantillon ultra-mince facilite également l'analyse sur deux fronts. Tout d'abord, en deux dimensions, les phénomènes de fluctuation liés à la transition supraconductrice sont exacerbés, facilitant l'analyse des changements de largeurs. Deuxièmement, les aspects liés à la percolation et au clustering peuvent être facilement simulés et comparés à des modèles analytiques. La transition supraconductrice typique mesurée dans nos échantillons, comme on le voit dans la dépendance à la température de la résistance de couche $R_S(T)$, a une largeur clairement visible à partir de la courbe dérivée dR_S/dT. Les principales contributions mésoscopiques ou locales à cette largeur sont les fluctuations et l'inhomogénéité. L'inhomogénéité de l'échantillon peut provenir de défauts ou de dopage hétérogène entraînant une distribution mesoscopique du dopage et une variation locale de la température critique. Dans le cas extrême, l'échantillon peut également comprendre des régions non supraconductrices. Nous avons établi sur la base de comparaisons systématiques entre l'expérience et les simulations de supraconductivité 2D que les mesures de résistance de couche de la transition sont marquées de manière indélébile par l'inhomogénéité et les fluctuations quantiques. Nous avons en outre constaté que la dérivée de la résistance de couche normalisée en fonction de la température (que nous abrégerons simplement par « dérivée ») présente un pic asymétrique à la transition supraconductrice. La moitié LT (basse température) de ce pic est dominée par des effets d'inhomogénéité tandis que la moitié HT (haute température) du pic, notamment la queue asymétrique HT, est dominée par des fluctuations quantiques.

Nous avons fait une analyse de l'effet de l'inhomogénéité en comparant des échantillons homogènes et inhomogènes d'une part et un échantillon homogène dans lequel nous introduisons l'inhomogénéité sous la forme d'un réseau ordonné de régions non supraconductrices par l'application d'un champ magnétique. Pour étudier les effets des fluctuations, nous nous sommes concentrés sur la partie HT de la courbe dérivée. Nous avons présenté 5 échantillons monochouche de BSCCO-2212 (dont 2 du côté surdopé et 3 du côté sous-dopé) et avons montré que le régime de fluctuation dans la partie sous-dopée du diagramme de phase est fondamentalement différent de celui dans la partie où $p > 0{,}19$. Nous l'avons établi en analysant l'étendue de la partie HT du pic dérivé (étendue de T_C à T_f comme indiqué au chapitre 5) en fonction du dopage. Nous avons ensuite discuté de la différence de régime de fluctuation pouvant être causée par la nature différente de la transition supraconductrice. A $p < 0{,}19$, il semble que les fluctuations s'étendent sur une large plage de température qui semble augmenter à mesure que le dopage et la température critique diminuent. Pour $p > 0{,}19$, la plage de température de fluctuation semble être constante même si T_c diminue à nouveau. Ce dernier pourrait être compatible avec un scénario où des fluctuations d'amplitude sont présentes dans une région limitée au-dessus de la transition. Cependant la transition supraconducteur-isolant induite par dopage établie dans cette thèse est compatible avec un scénario où la transition supraconducteur-isolant est une transition de boson où les paires de Cooper existant à une température bien supérieure à T_c deviennent cohérentes en phase lorsque la supraconductivité apparaît. Le grand domaine d'existence de fluctuations bien au-dessus de T_c dans la partie sous-dopée du diagramme de phase peut être compris dans ce scénario. De tels régimes différents pourraient être imaginés à la lumière de la transition BEC-BCS discutée dans l'introduction, bien qu'on ne pense généralement pas à l'heure actuelle qu'une supraconductivité à haute T_c pourrait être le système où une telle transition pourrait être observée.

Contents

Chapter 1

High Critical Temperature 2D Superconductors

In this chapter, I will first give a brief introduction on the history of 2D superconductors as well as experimental technique related. Then I will concentrate on the high critical temperature cuprates and $\mathrm{Bi_2Sr_2CaCu_2O_{8+x}}$ which is the material studied in this thesis.

1.1 High critical temperature 2D materials

Superconductivity was first discovered in mercury at 4 K by H. Kamerlingh Onnes in 1911 in Leiden [1]. The phenomenon was described phenomenologically by Vitaly Ginzburg and Lev Landau in 1950 with the Ginzburg-Landau (GL) theory [1, 2]. The GL theory defines a mathematical complex valued scalar field akin to a quantum wavefunction with non-zero average values below a critical temperature and responsible for superconductivity, however at first without explaining the physical meaning of this wavefunction. Indeed, the microscopic mechanism of the phenomenon stayed unexplained until the proposition of the "Bardeen–Cooper–Schrieffer (BCS) theory" in 1957 [3]. From the microscopic point of view, the BCS theory explains superconductivity by the condensation of 'Cooper' pairs of electrons at low temperature in a non-dissipative quantum ground state due to a weak effective attractive interaction between electrons. This interaction is mediated by phonons in what is known as conventional superconductivity. Superconductivity has seen several breakthroughs in the last few decades. First when High Temperature Superconductivity (HTS or high-T_c) was discovered in 1986 [4] and identified as non-conventional because of still unresolved questions about the nature of the effective attractive interaction. The related material are called high temperature superconductors (HTSC). Then when several intriguing results were obtained in interface [5, 6] and two dimensional (2D) superconductivity [7, 8, 9, 10]. And finally with the discovery of other non-conventional superconductors [11, 12, 13, 14, 15]. The study of superconductivity in two dimensions has greatly benefited from advanced techniques of material fabrication technology like molecular beam epitaxy (MBE), mechanical exfoliation and field effect devices.

1.1.1 Conventional and highly crystalline 2D superconductors

Superconductors with a thickness d much smaller than the coherence length of the quantum mechanical wave-function in the superconductor ξ_{GL} are known as 2D superconductors [16]. The GL length at 0 K $\xi_{GL}(0K)$ is of the magnitude of a few hundred nanometres for conventional superconductors. A two dimensional conventional superconductor is thus relatively easy to make in the form of a thin film. In the case of unconventional superconductors with high transition temperature, the ξ_{GL} can be as small as a few nanometres, often corresponding to the thickness of one unit-cell layer [16]. So the fabrication of large samples of ultra-thin superconducting materials is of great significance for studying unconventional superconductivity in two dimensions. Superconductivity in thin films was first measured by Shalnikov in 1938 [17]. Pb and Sn thin films were condensed from vapour at 4.2 K on glass in a rather high vacuum pressure. This method was adopted during the next decades for the fabrication of thin layer samples which were amorphous or granular [18, 19, 20]. New fabrication techniques, including molecular beam epitaxy (MBE), interface reconstruction and mechanical exfoliation have flourished in the 21st century [21]. Fig. 1.1 shows the evolution of film thickness and morphology fabricated by different techniques since the 1980s [21]. Highly crystalline 2D samples are now regularly obtained for all kinds of materials.

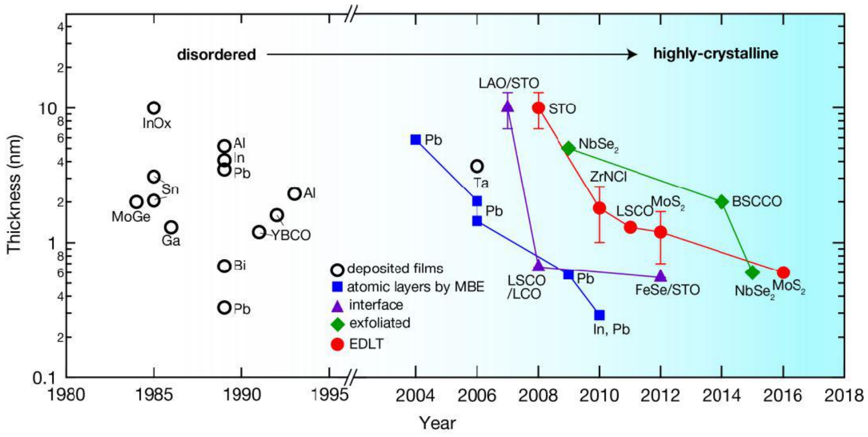

Figure 1.1: Thickness of 2D superconducting materials vs year [21].

A fascinating example of unconventional 2D superconductivity is that of one unit-cell FeSe films grown on $SrTiO_3$ by MBE with a superconducting transition around 77 K [14], while T_c for bulk FeSe is only 8 K [22]. Soon after, a T_c over 100 K was announced in this FeSe/STO system by means of $in-situ$ four-point probe electrical transport measurements [23], but unfortunately these results have not been confirmed since. This also points to the delicate nature, both of 2D samples and the measurements connected with them, calling for great care in sample fabrication and in measurement.

High temperature superconductivity (high-T_c or HTS) was observed in 1986 in cuprate compounds by Bednorz and Müller [4], for which they have been awarded the Nobel Prize in 1987. Since then numerous different kinds of cuprate superconductors with increasing transition temperatures have been discovered. Fig. 1.2 from the reference [24] shows the date of discovery and critical temperatures of superconductors from 1904 to 2000.

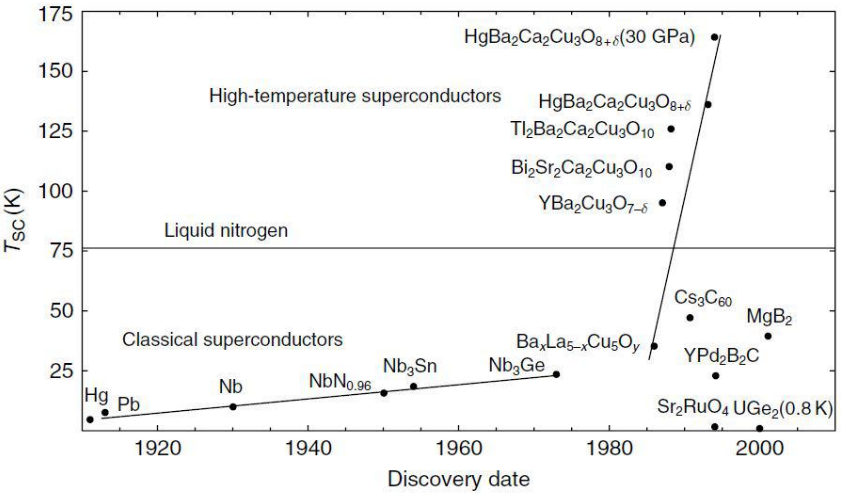

Figure 1.2: Development of the critical temperature vs year since the discovery of superconductivity [24].

1.1.2 High critical temperature cuprates

The discovery of HTS in the La-Sr-Cu-O (LSCO) system with an onset critical temperature at $\sim$ 35 K in 1986 by Bednorz and Müller [4] not only largely increased the transition temperature, higher than any previously known superconductor, but also introduced a class of copper oxide superconducting materials named cuprates. During the next decade, high transition temperature has been observed in other cuprate composites $YBa_2Cu_3O_{7-x}$ [25, 26, 27, 28, 29], $BiSrCaCu_2O_x$ [30] and Ti-Ca/Ba-Cu-O [31]. Since then researchers have been working on the fabrication of ultrathin cuprate superconductors. We also note that with the advent of fabrication techniques like molecular beam epitaxy (MBE) with ultrahigh vacuum (UHV) and mecanical exfoliation researchers were able to fabricate highly crystalline superconducting cuprates on the atomic scale [6, 32, 33]. This progress lead to a qualitative understanding of the nature of superconducting phenomenon and the nature of 2D physics.

Crystal structure and electronic properties

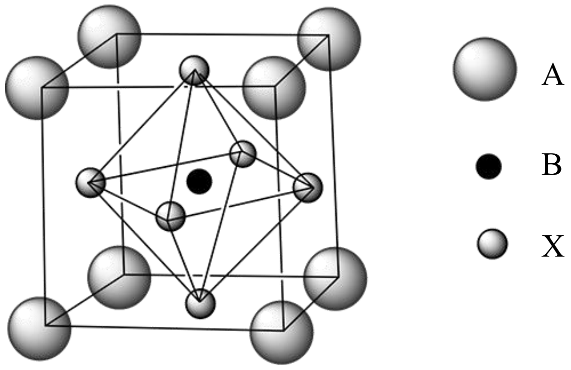

Figure 1.3: Crystal structure of perovskite with the universal formula ABX_3. Each cation B is surrounded by an anion octahedron.

Cuprates are complex oxides that have layered perovskite structure. A perovskite structure adopts a general formula ABX_3 as shown in Fig. 1.3, A and B representing cations, X an anion (often oxide) that bonds to both cations. For cuprates, the universal composition formula can be given as

$$B^{b+}[(CuO_2)^{2-\delta}-]_n C^{c+}_{n-1} \tag{1.1}$$

where $n = 1,2,3,...$, $c = 2$ or 3, $b = c + n(2 - \delta - c)$ and δ represents the doping level , which can be positive (hole doping) or negative (electron doping) [34]. The cationic metal oxide layer B, together with either a single layer $(CuO_2)^{2-\delta}$ or a couple consisting of n such layers, sandwiches the cations C in the middle. The cation C can be Ca^{2+} or Y^{3+}, La^{3+}, or any trivalent cation of the lanthanides.

Fig. 1.4 from reference [35] shows the atomic structure of some high temperature superconductor (HTSC) cuprates. As shown in the figure cuprates are consituted of stacks of alternating doped conducting copper oxide planes, separated from each other by varied insulating layers[16, 34]. The direction of stacking is usually considered as the crystallographic c-direction.

Figure 1.4: Crystal structures for cuprates. **a** Crystal structures of four different cuprates. The way of varying their hole concentration of this four kinds of cuprate is different. The hole concentration in the CuO_2 layers of Hg1201 YBCO and Tl2201 is modified by varying the density of interstitial oxygen atoms (each interstitial oxygen atom provides maximum two holes into nearby CuO_2 layers); while for LSCO, the hole concentration is altered by means of replacing La^{3+} with Sr^{2+}, so that its doping level $p = x$ in this case. **b** Planar Cu $(3d_{x^2+y^2})$ and O $(2p_x$ and $2p_y)$ orbitals are shown in the CuO_2 layer. [35]

The CuO_2 2D planes (Fig. 1.4**b**) with in-plane Cu $(3d_{x^2-y^2})$ and O $(2p_x$ and $2p_y)$ orbitals define the relevant electronic structure. In the undoped state this electronic structure is characterized by strong electronic correlations leading to strong on-site Coulomb repulsion between charge carriers [36, 37] despite what should be a half filled energy band near the Fermi energy [36, 38]. As a consequence, an insulating energy gap of 2 eV in the undoped cuprates leads to an antiferromagnetic insulator [24, 36, 37, 38]. "Hole doping" (or "electron-doping") is achieved by removing (or adding) electrons. The phase diagram as a function of doping level p, defined as the number of holes per Cu atom, and of critical temperature T_c, defined as the temperature at which the resistivity vanishes, is shown in Fig. 1.5. All hole doped cuprates have the same generic phase diagram. At the optimal doping level $p_{opt} \sim 0.16$ [37, 38], we have the highest critical temperature. For doping levels $p < 0.16$, the material is underdoped and for $p > 0.16$, the material is overdoped (Fig. 1.5). As seen in Fig. 1.5, an antiferromagnetic phase exists at $p < 0.02$-0.05 [37]; As doping increases, this phase is replaced by a 'pseudo-gap' phase. As doping increases, at low temperature superconductivity appears. Superconductivity exists from $p \sim 0.05$ to below $p \sim 0.3$ [37]. At very high doping $p > 0.3$, a normal metal phase (or Fermi liquid phase) appears [37]. At temperatures higher than those characterized by the existence of superconductivity, the succession of phases is roughly that of the pseudo-gap phase in the underdoped region, a 'strange metal' phase in the optimally doped region and the normal metal phase in the overdoped region. The pseudo-gap phase is characterized by the suppression of low energy excitations as if a gap or 'pseudo-gap' existed in the electronic structure while the strange metal phase possess some exotic properties like linear resistivity as a function of temperature. These properties can be used in spectroscopic or transport measurements for delimiting the corresponding regions of the phase diagram.

Phase diagram

Antiferromagnetic (AF) phase The stoichiometric undoped parent cuprate compounds are "Mott insulators" with strong electron correlations in the CuO_2 planes [39], which means that a large energy (the Hubbard U [40]) is required to move an electron from one site to another. These well localized electrons finally result in a strong AF interaction between adjacent spins, thus representing an AF arrangement below a finite Néel temperature [36, 41]. However, the AF phase is rapidly destroyed by increasing hole doping in the copper oxides 2D layers. As mentioned before, the AF state just exists at $p < 0.02$-0.05 (Fig. 1.5).

Pseudo-gap (PG) phase The "pseudo-gap" phase is observed in the underdoped region above T_c [42]. Despite the fact that this regime is still not well understood, the PG phenomenon has been observed in electronic spectra measured in Angle Resolved Photoemission Spectroscopy (ARPES) as shown in Fig. 1.6, and Scanning Tunneling Microscope (STM) as shown in Fig. 1.7. These experiments suggest that the pseudo-gap is well distinguished from the superconducting gap, notably because it persists above T_c and reaches values much higher than the superconducting gap. The superconducting gap is characterized by its $d_{x^2-y^2}$ symmetry which implies a maximum value for

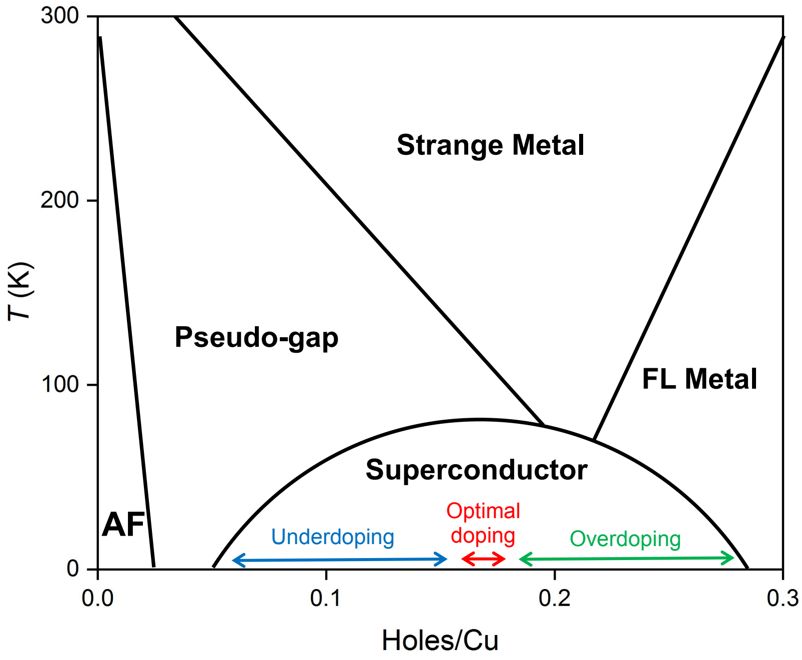

Figure 1.5: Generic phase diagram of hole doped high temperature cuprate superconductors.

the gap along the crystallographic axes and a vanishing value on the nodes. Tunneling experiments also verify the nodal-antinodal gap dichotomy and notably associate the pseudo-gap with local inhomogeneities on the nanoscopic scale[43].

Superconducting (SC) phase The SC phase is identified with a critical temperature T_c, below which the sheet resistivity of a superconductor falls to zero. However, this T_c depends on the hole concentration p of copper atoms. There is a maximum critical temperature $T_{c(max)}$ that appears at the doping level $\sim$ 0.16, which is generally taken as the optimal doping level p_{opt} [24]. The T_c decreases smoothly in both directions away from p_{opt} (Fig. 1.5), thus creating a superconducting dome which is empirically defined by the formula:

$$\frac{T_c}{T_{c(max)}} = 1 - 82.6(p - 0.16)^2 \tag{1.2}$$

This empirical formula, introduced by Presland and co-workers in 1991 [45], reveals the relation between T_c and doping level p.

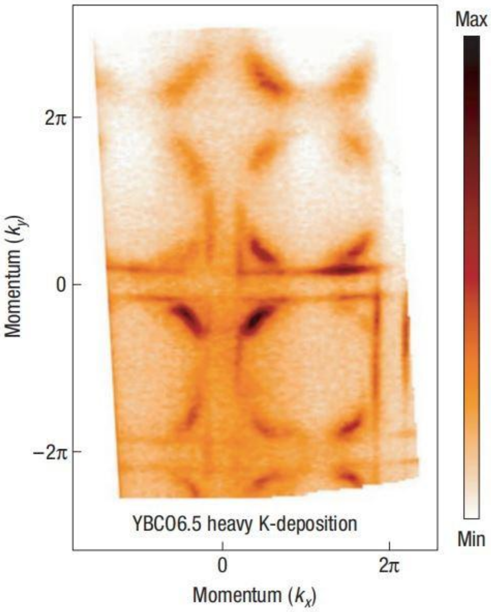

Figure 1.6: ARPES Fermi surface of $YBa_2Cu_3O_6$.5 (< 1 monolayer) with an effective hole doping $p = 0.11$ per planar Cu atom by evaporating potassium on the as-cleaved sample. The Fermi energy E_F ARPES intensity appears to be the 1D CuO-chain Fermi surface and four disconnected nodal CuO2 Fermi arcs. [44].

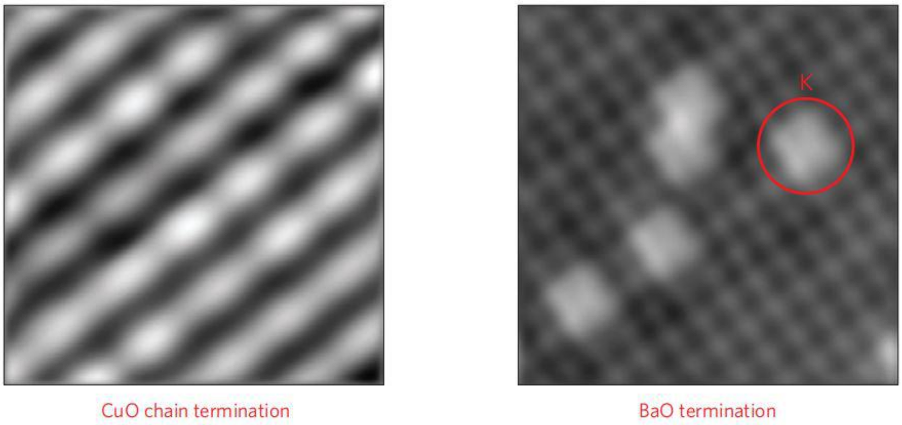

Figure 1.7: STM images (4×4 nm^2) from ortho-II $YBa_2Cu_3O_6$.5 confirm the ∼50–50 % CuO–BaO termination of the cleaved surface, the ortho-II alternation of full and empty chains, and the preferential location on BaO of evaporated K (red circle). [43]

Strange metal (SM) phase and Fermi liquid phase In the strange metal phase, transport measurements show that there is a linear dependence between resistivity and temperature, which is different from Fermi liquid behaviour. This phenomenon has inspired many theoretical models, for example the so-called "marginal" Fermi liquid (MFL) model, introduced by Varma et al. in 1989 [46]. This particular theory supposes that the temperature dependence can be explained by electrons scattering off bosonic quasiparticles because the bosonic spectrum increases linearly in energy up to a characteristic high energy scale T and is then constant above it [38, 46].

At higher doping in the overdoped region, the material transits to a Fermi liquid phase, which is also known as the normal metal phase. According to the ARPES measurements, the FL phase is characterized by a transition from a "Fermi-arc" type small Fermi surface to a "normal" large Fermi surface [39].

1.1.3 2D $Bi_2Sr_2CaCu_2O_{8+\delta}$

Crystal structure and electronic properties

Bismuth strontium calcium copper oxide, discovered in 1988 as a general class [30], is the first HTSC without rare earth element. For Bi-Sr-Ca-Cu-O, there are three superconducting phases, forming a general formula $Bi_2Sr_2Ca_{n-1}Cu_nO_{4+2n+\delta}$ (n=1,2 and 3) with transition temperatures 20 K, 85 K and 110 K respectively [47]. The compound $Bi_2Sr_2CaCu_2O_{8+\delta}$ (BSCCO-2212, Bi2212) is one of the most studied high temperature cuprate superconductors, and is also the object of this thesis. Thus I will concentrate on the introduction of BSCCO-2212 (BSCCO below) in the following. The crystal structure of BSCCO is shown in Fig. 1.8 with the space group Fmmm [48]. The lattice parameters are respectively $a = b = 5.4$ Å and $c = 30.8$ Å [48]. There are two CuO_2 layers in the unit cell of BSCCO, with the Ca atoms forming a layer within the interior. This "CuO_2-Ca-CuO_2" structure, which is what we call a half unit-cell of BSCCO in this thesis, are separated by insulating SrO and BiO layers. The BiO layers are typically where the BSCCO crystal cleaves due to the weak coupling, caused by the large distance ∼3 Å, between BiO layers [39, 49]. Different methods, including epitaxy, sputtering and pulsed laser deposition [48, 50], have been used for the fabrication of thin film BSCCO samples. During the last decades, inspired by the exfoliation fabrication method of graphene [51] and the layer structure of BSCCO, mechanical exfoliation techniques with "scotch tape" have been applied to get thin film BSCCO samples [52].

BSCCO is very anisotropic which makes it interesting for studying superconductivity. The magnitude of out-of-plane (c-axis) resistivity ρ_c is several orders (up to 10^5) larger than that of in-plane (ab-plan) resistivity ρ_{ab} [52]. Fig. 1.9 ([52]) shows the in-plane resistivity ρ_c and the out-of-plane resistivity ρ_{ab} of 30 nm-thick BSCCO and bulk BSCCO samples. Before the superconducting transition, the temperature dependence of in-plane resistivity ρ_{ab} shows a metallic behaviour ($d\rho_{ab}/dT > 0$), while that of out-of-plane resistivity ρ_c shows an insulating behaviour ($d\rho_{ab}/dT < 0$). Then ρ_c falls steeply

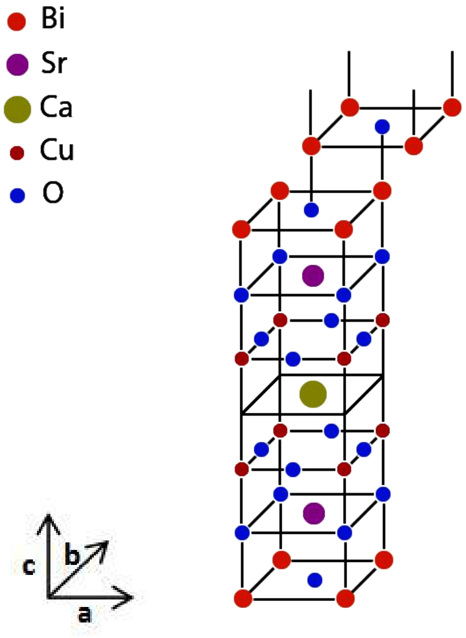

Figure 1.8: The unit cell structure of $Bi_2Sr_2CaCu_2O_{8+\delta}$.

and together with ρ_{ab} becomes superconducting at T_c. We can also observe a suppression of T_c for thin BSCCO layer compared to that for bulk, which can be explained by the loss of oxygen when reduced to few layer BSCCO samples. However recent research [32] has reported the fabrication of exfoliated half-unit-cell BSCCO covered by graphene with a sharp superconducting transition above 88 K. Another paper [53] obtained superconducting half-unit-cell BSCCO by mechanical exfoliation on a cold stage (- 40 °C) in an Ar-filled glove box and observed a superconducting transition at up to 91 K at the optimal doping level ($p = 0.16$). A Superconductor-Insulator-Transition (SIT) was also observed and this will be discussed in detail later. This thesis has focused on the study of 1 unit-cell (3 nm-thick) BSCCO samples. We also adopted the mechanical exfoliation technique to fabricate samples of good quality, and aim to study their properties with the techniques in our lab.

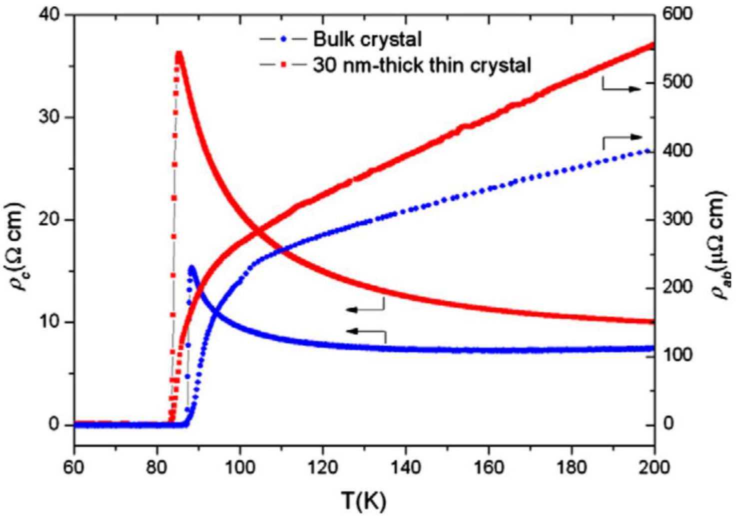

Figure 1.9: Temperature dependence of in-plane and out-of-plane resistivity for bulk and exfoliated 30-nm-thick Bi2212 single crystals, with T_c = 87.2 K and 83.1 K respectively [52].

1.2 High Critical Temperature 2D physics

1.2.1 Electron correlation and superconductivity

Classic BCS theory

In 1957, the Bardeen–Cooper–Schrieffer (BCS) theory of superconductivity was proposed by Bardeen, Cooper and Schrieffer to explain the mechanism of conventional superconductors [3]. This theory is based on the assumption that electrons are bound into a pair (Cooper pair with opposite spins and zero orbital momentum for singlet s-wave pairing) as a result of a weak retarded attraction induced by the exchange of phonons between quasi-particles [54, 55]. In the weak coupling limit ($kT_c << \hbar\omega$), the BCS theory proposes the critical temperature T_c to be

$$kT_c = 1.14\hbar\omega e^{-\frac{1}{N(0)V}} \tag{1.3}$$

where $N(0)$ is the density of electron states at the Fermi level, V is the electron-phonon coupling potential, and $\hbar\omega$ is an energy shell around the Fermi surface, inside which the electron-phonon coupling potential is non zero [3, 24, 39]. This formula introduces the critical temperature T_c, below which the normal state electrons are unstable compared to the formation of the condensate of Cooper pairs [39]. The proportional dependence between T_c and $\hbar\omega$ is coherent with the isotope effect measured in conventional superconductors (T_c is inversely proportional to the mass of the isotope of the material) [3, 56]. The classical BCS theory is ideal for conventional superconductors and the predicted range of critical temperature is compatible with conventional superconductivity and low critical temperature of the order of 1-10K. For HTSC, which have a critical temperature which is an order of magnitude higher, classical BCS theory is not valid. Consequently mechanisms have been sought for interactions with higher energy scales than the electron-phonon interaction, like for example, electronic correlation [24]. However the basic common feature of correlation of the critical temperature with the energy scale of the interaction that induces electron pairing remains unknown [57].

Strong electron correlated system

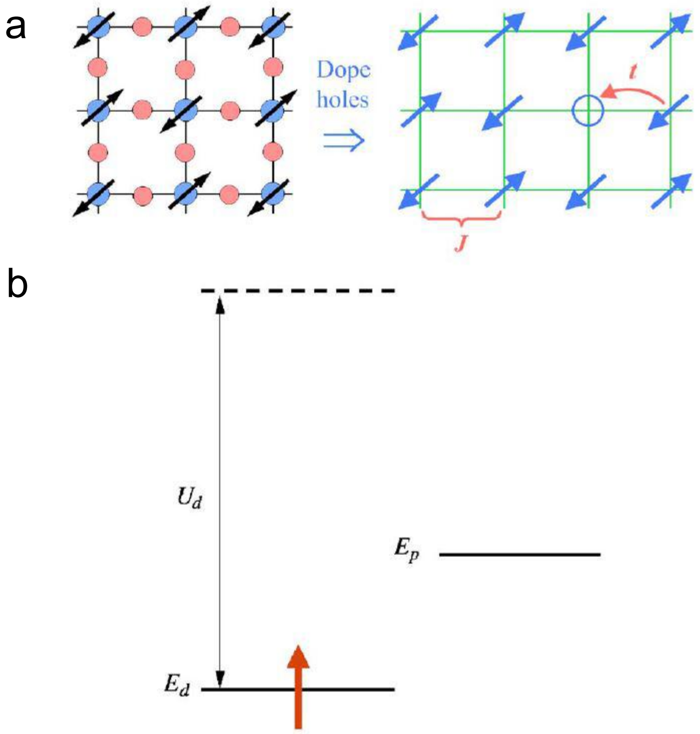

Figure 1.10: Electronic structure of copper oxygen layer **a** CuO_2 layer (left) and its single-band model (right); Blue and red circles represent respectively copper atom and oxygen atom. U_d is the energy deeded to doubly occupy E_d. **b** The copper d and oxygen p orbitals; A single hole of $S = 1/2$ occupies the copper d orbital in the antiferromagnetic insulator [58].

The high-Tc cuprates are correlated electron systems [57, 58]. The parent (undoped) compound is generally classified as a “Mott insulator”. For a Mott insulator, the conducting state is blocked by strong electron-electron repulsion instead of the Pauli exclusion principle in the case of a conventional insulator [59]. In other words a conventional insulator is characterized by a fully filled highest occupied electronic band and a Fermi level in a gap while a Mott insulator may be insulating with a partially filled band because of localization due to Coulomb repulsion. In the case of CuO_2 layer in cuprates, the copper ion, doubly ionized, is in d^9 configuration, which means that there is an odd number of electrons and a single hole in the d shell per unit cell. Thus to put two electrons on the same site, there is a strong repulsive energy. When this electron-electron Coulomb repulsion (usually named U) dominates over the hopping energy t, the electron motion is hindered and the ground state is an insulator [58, 59, 60]. Besides, neighbouring spins are oppositely aligned so that the cuprates should be antiferromagnetic and an electron acquires an exchange energy $J = 4t^2/U$ by virtual hopping (Fig. 1.10) [58]. However doping can provide sites for electrons to hop without cost of Coulomb repulsion energy [59].

Although the mechanism of HTSC is not yet well understood, there are models which are used as prototypes. One of the widely used simplified models is the single-band Hubbard model on a 2D square lattice (Fig. 1.10) [57, 61, 62, 63, 64, 65]. In the case of this single-band model, the Cu $d_{x^2+y^2}$ is hybridized by the O anion network (Fig. 1.4**b**), which results in a single $d_{x^2+y^2}$ band. The Hamiltonian for this single-band model is written as

$$H = -\sum_{ijs} t_{ij}(d^+_{is}d_{js} + d^+_{js}d_{is}) + U\sum_i n_{i\uparrow}n_{i\downarrow} \tag{1.4}$$

where t_{ij} is the tight binding one-electron hopping energy between sites i and j, and d^+_{is}/d_{is} creates/annihilates an electron with spin s on site i, and $n_{i\uparrow} = d^+_{i\uparrow}d_{i\uparrow}$ is the occupation number of electrons with spin up at lattice site i [65].

In this simple model, one ignores other orbital (e.g. p) degrees of freedom, long-range Coulomb interaction, or electron-phonon coupling [66] but for Anderson this 2D single-band Hubbard model on a square lattice is a minimal model that contains the essential cuprate physics [67]. There are some investigations with variational cluster perturbation theory [68, 69] which indicate that the ground-state phase diagram of the single-band model, with consideration of second and third neighbour hopping (t' and t'' respectively), is qualitatively similar to that of hole- (electron-) doped cuprates (Fig. 1.11). Also, in weak coupling limit (where $U/t \to 0$), the doped single-band Hubbard model can lead to a $d_{x^2+y^2}$ superconducting phase [70, 71]. Recent publications [57, 72] have shown that a superconducting phase in the ground state exists for the 2D single-band model.

Bose-Einstein condensation

Bose-Einstein condensation (BEC) was proposed as a mechanism of superfluidity in ^{4}He and superconductivity by Fritz London in 1938 [73]. BEC which describes the low temperature ground state of bosons or paired fermion systems, is a common phenomenon appearing in physics on all scales, including condensed matter, nuclear, elementary particles and astrophysics [74]. Compared with the BCS theory, the BEC is a model of superconductivity which considers the electron pairs as bosons with a charge of $2e$. The

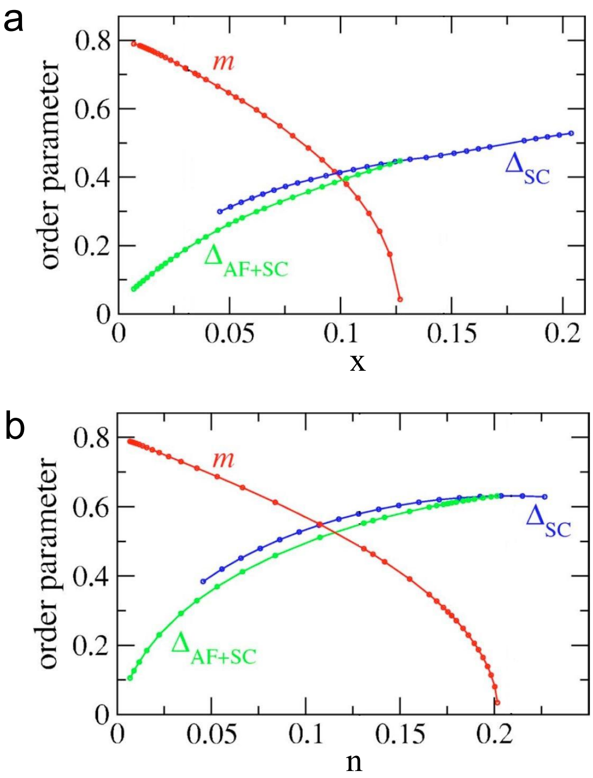

Figure 1.11: (Color online) Antiferromagnetic (AF) and superconducting (SC) order parameters m and Δ. **a** Hole doping x dependence of AF and SC order parameters m and Δ. Δ, which is scaled by a factor of 5 for convenience, is plotted for the AF+SC (green) and for pure SC homogeneous solutions (blue). For low doping, both AF and SC order parameters m and Δ are non-zero, indicating a coexistence of AF and d-wave SC order; The system tends to separate as doping goes higher; And a homogeneous pure SC phase (m=0 and Δ¿0) is attained or larger doping. **b** Same as **a** but for electron doping n. [66]

BCS theory accounts for superconductivity phenomenon in the weak-coupling or high-density limit and is effectively observed in condensed systems with these charcteristics. Conversely, BEC is valid for strong-coupling and low-density limit and is observed typically in low density, ultra-low temperature atomic gases [75]. From the GL point of view the wave function of the condensed ground state is characterized by an amplitude (proportional to the density of the bosons or the fermion pairs) and to a phase (which characterize the existence of long-range coherence). In the BCS model both the amplitude and the phase become non-zero at the same critical temperature. In the BEC model bosons exist on both sides of the superconducting transition, which means that the electrons first form pairs (bosons) and then undergo the BEC with the advent of phase coherence, to the superconducting state. The pseudo-gap state of some exotic superconductors has been linked to formation of electron pairs above T_c [76]. In the case of BCS theory, the electrons condense into the equilibrium concentration of pairs only below T_c [75, 76].

In 1969, Eagles [77] discussed the possibility of the BCS-BEC crossover and electron binding above the superconducting transition temperature for a low density of carriers in bulk and thin-film Zr-doped $SrTiO_3$. Since then, numerous works, both experimental and theoretical, have been done with this aim [78, 79]. Nowadays, it is widely accepted that the BCS and BEC are two extrema of one continuum [79], which can be explored by tuning the interaction strength. Fig. 1.12 qualitatively shows the BCS-BEC crossover phase diagram [79].

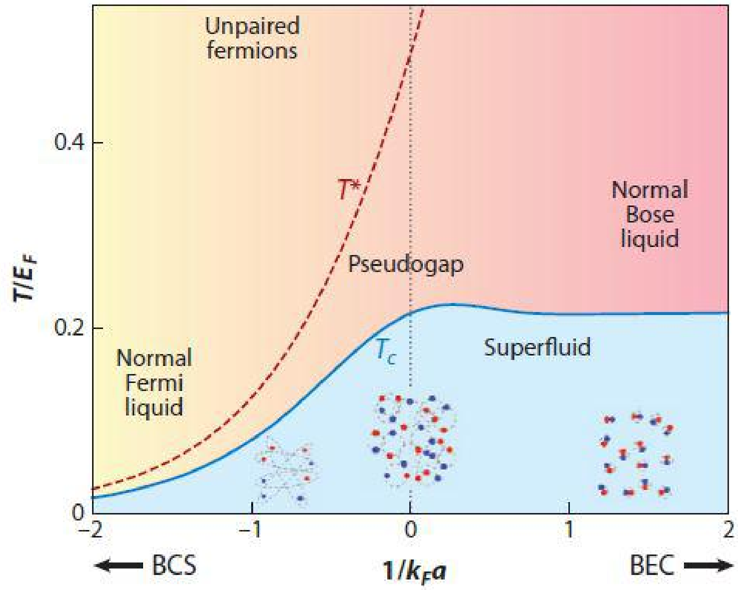

Figure 1.12: The qualitative BCS-BEC crossover phase diagram as a function of T/E_F, where E_F is the Fermi energy, and of coupling $1/k_F a$, where k_F is the Fermi momentum and a is the scattering length. The evolution of the BCS limit with weak-coupling Cooper pairs to the BEC limit with strong-coupling Cooper pairs is represented. T_c indicates the transition temperature, below which the *blue* region shows the superfluid state. T^* signifies the pair-formation crossover scale, which diverges away from T_c as the attraction increases. [79]

1.2.2 Superconductor-Insulator Transition

When the electronic wave function in the ground state at the Fermi level is localized an insulator is obtained. When the electronic wave function is delocalized a metallic state results. Superconductivity appears in a metallic state as temperature is lowered, but at zero (or very low) temperature, another parameter (e.g. magnetic field) may be varied, localizing the electronic wavefunction and thus leading to a phase transition from a superconductor directly to an insulator. This is called a a quantum phase transition (QPT) as opposed to a phase transition accompanied by thermal fluctuations [76, 9],

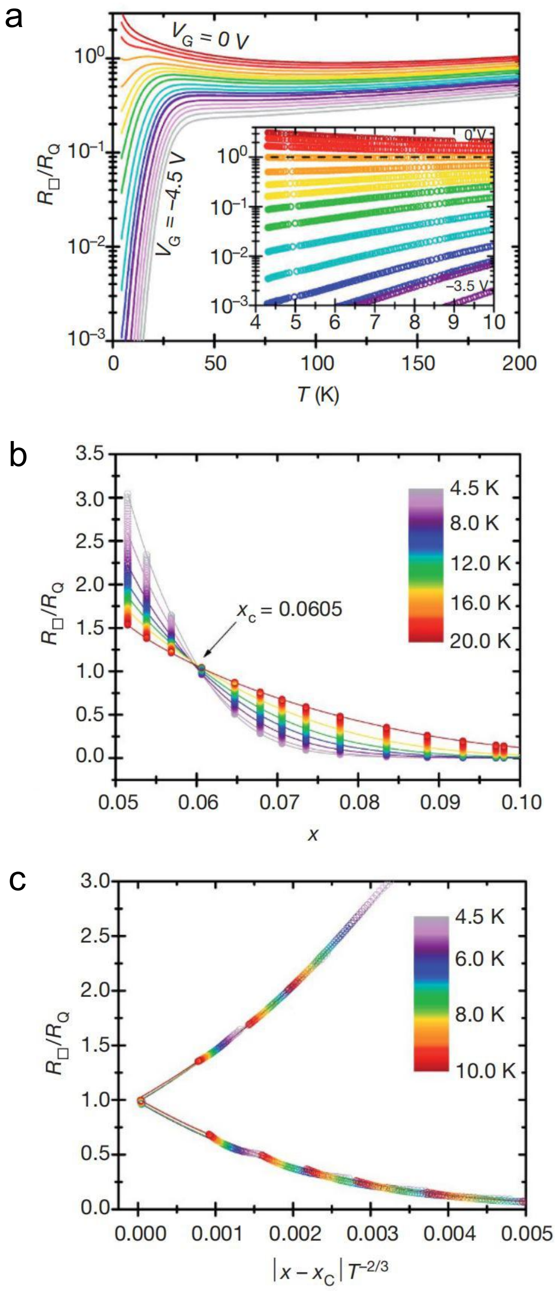

Figure 1.13: Finite-size scaling of QPT in ultra-thin LSCO. **a** Normalized sheet resistance curves $R_\square/R_Q$ as a function of temperature, where $R_Q = h/(2e)^2 = 6.45\ k\Omega$ is the quantum resistance for pairs. A SIT is realized by varying the gate voltage from 0 V to 4.5 V with steps of 0.25 V. The inset emphasizes separatrix below 10 K. The black dashed line corresponds to the critical point where $R_\square = R_Q$. **b** Doping dependence of isothermal sheet resistance from 4.5 K to 20 K with the same data as figure **a**. Here the doping level x is determined by $x = 0.33\ k\Omega/R_\square(T = 180\ K)$. The crossing point indicates the critical doping level $x_c = 0.06\pm0.01$, and the corresponding critical sheet resistance $R_c = 6.45\pm0.10\ k\Omega$. **c** Universal finite-size scaling as a function of $\mu = |x - x_c|T^{1/\nu z}$ with the same data as before between 4.5 K and 10 K. With the critical exponent $\nu z = 1.5$, the discrete groups of data from figure **b** collapse onto the single finite-size scaling function. [80]

because the transition occurs at zero temperature. The superconductor-insulator transition (SIT), especially in 2D, is a prototype continuous quantum phase transition that can be driven by external parameters such as disorder, magnetic field or carrier concentration [53, 81, 80, 82].

For QPTs, a significant marker is that their behaviour follows finite-size scaling analysis [80, 82, 8]. Sheet resistance near a quantum critical point should collapse onto a single finite-size scaling function $R_S = R_c f(|x - x_c|T^{1/\nu z})$, where R_c is the critical resistance at the limit $x \to x_c$ and $T \to 0$; f is the universal scaling function and x is the tuning parameter, like disorder, magnetic field or carrier concentration. The correlation length exponent ν and the dynamic critical exponent z, together with the critical resistance R_c encode the nature of this transition [80, 82]. Fig. 1.13 shows the procedure of the finite-size scaling in the case of LSCO [80].

Such transitions have been induced in a variety of 2D superconductors. There is however not much uniformity in the findings since both the superconducting systems and the tuning parameters are quite diverse. Magnetic field driven SIT studies have reported a large variety of critical exponents and resistance at criticality: from $\nu z \sim 0.7$ and $R_c = 1.3\ k\Omega$ in NbSi thin films [83] to $\nu z \sim 2.3$ and $R_c = 6\ k\Omega$ in Indium oxide thin films [84]. Furthermore, in quenched condensed bismuth thin films the magnetic field driven SIT was shown to have $\nu z \sim 0.7$ and $R_c = 8\ k\Omega$, while the thickness driven SIT displayed $\nu z \sim 0.71.2$ around the same critical resistance, indicating a fundamental difference in their nature [81]. The high critical magnetic field of most high critical temperature superconductors renders the study of the magnetic field driven SIT difficult with the exception of the electron doped cuprate NdCeCuO [85]. However, improvements in extreme electrostatic doping techniques have provided access to the carrier density driven SIT in LSCO (with $\nu z \sim 1.5$ and $R_c = 6.4\ k\Omega$) [80] and YBCO (with $\nu z \sim 2.2$ and $R_c = 6\ k\Omega$). In a recent paper about the result in half unit cell BSCCO samples is remarkable but uses chemical doping with ozone. Their product of critical exponents νz of BSCCO is between 1.5 and 2.4, and the critical sheet resistance also varies from 2.8 to 10.2 kΩ [53]. In our case, we accomplish electrostatic doping with our space charge doping technique on a one unit cell (1 u.c.) BSCCO device and indeed observe a QPT, which will be introduced in detail in a later chapter.

1.3 Transport properties of 2D high T$_c$ cuprates

1.3.1 In-plane resistivity

For hole-doped high-T$_c$ cuprates, the temperature dependence of in-plane resistivity $\rho_{ab}(T)$ changes systematically with doping. The hole-doped cuprate phase diagram as a function of temperature and doping level from reference [86] in Fig. 1.14 is established from the evolution of the in-plane resistivity $\rho_{ab}(T)$ with doping. For the optimally doped cuprates, $\rho_{ab}(T)$ is perfectly linear with temperature, the most unusual transport characteristic for cuprates [87, 88]. This is a ubiquitous feature for all the cuprate families, indicating that it is intrinsic to the copper oxygen layers [86]. Yet the region where the resistivity is strictly linear until low temperatures is only found very close to the optimal doping level [89]. Ando *et al.* [89] came to the conclusion that the quantum critical regime [59] with doping, if it exists, must be in a much narrower region in the cuprates than in other systems [90].

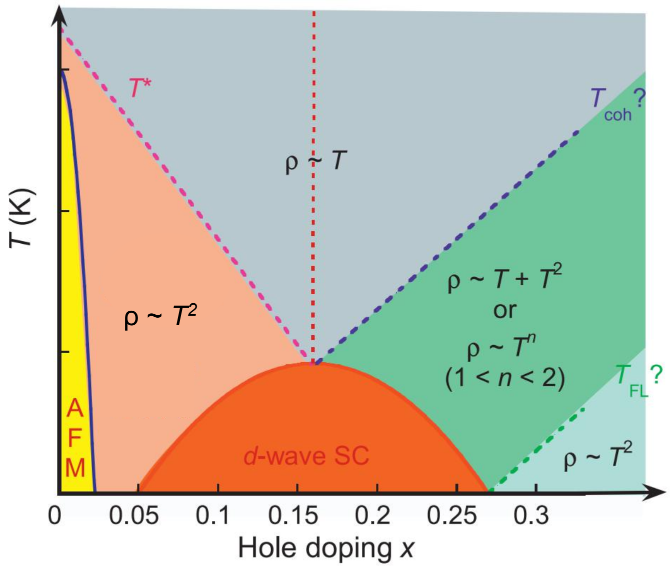

Figure 1.14: Hole-doped cuprate phase diagram on the basis of temperature as well as doping evolution of the in-plane resistivity $\rho_{ab}(T)$. The thick solid lines represents the boundaries between the normal state and the superconducting phase (orange) or antiferromagnetic ground state (violet). The thick dashed lines (green, blue, purple) illustrate the crossover between different in-plane resistivity $\rho_{ab}(T)$ behaviour. The vertical dotted line (red) indicates the optimal doping level, which separate the UD region (left) and OD region (right) on the phase diagram. [86]

In the UD region, at high temperature $\rho_{ab}(T)$ changes linearly with temperature in the strange metal phase (Fig. 1.5). However, this T-linear behaviour deviates downwardly below a characteristic temperature T^* (Fig. 1.14), the value of which increases continuously while decreasing doping level p, thus leading to the crossover between the pseudogap phase and the strange metal phase [89]. During this change of $d\rho_{ab}(T)/dT$, no clear evidence is found that it refers to a phase transition under T^* [86].

In the OD region on the phase diagram, the behaviour of $\rho_{ab}(T)$ can be modeled either by a single power law $\rho_{ab}(T) = \rho_0 + \alpha T^n$, where n varies from the value 1 at the OP to the value 2 for $T_c = 0$, or by fitting with a three-component polynomial $\rho_{ab}(T) = \rho_0 + \alpha T + AT^2$ [91]. The T-linear behaviour is again observed at high temperature in the strange metal phase above a coherent temperature T_{coh}. This crossover line T_{coh}, found from the loss of coherence in the energy dispersion curve measured in thin film BSCCO-2212 with ARPES, separates the OD region into two parts, which are the coherent metal phase at lower temperature and higher doping and the incoherent metal phase at higher temperature and lower doping [92]. In highly OD non-superconducting single crystal LSCO samples, the strictly quadratic T^2 behaviour is observed below 50 K, indicating the possible existence of a highly correlated Fermi-liquid ground state beyond the superconducting dome [93].

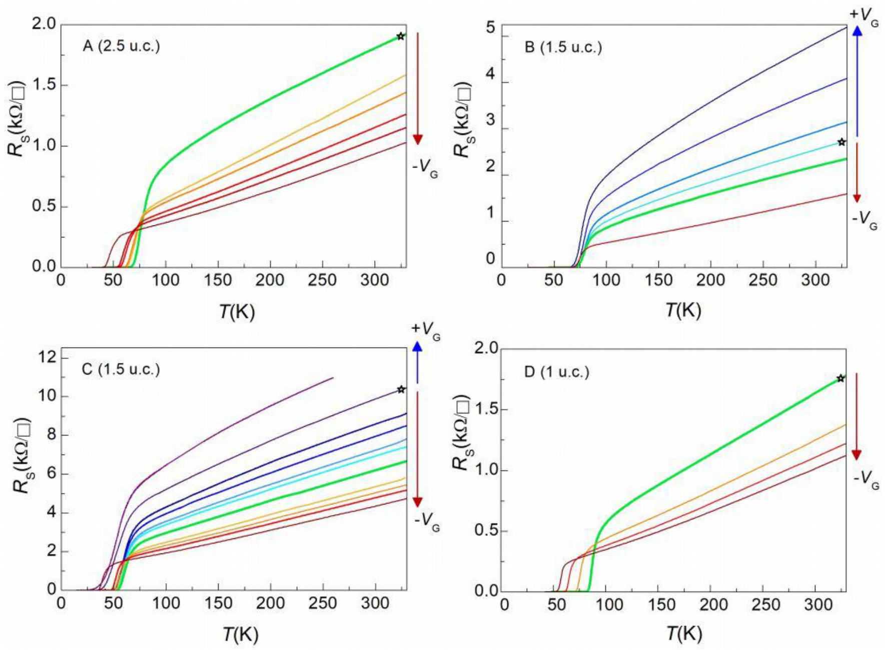

Figure 1.15: Sheet resistance curves $R_S(T)$ for the four ultra thin BSCCO-2212 samples at varying doping levels. Curves corresponding to the initial doping are indicated with stars; the underdoped region corresponds to cyan-blue curves whereas the overdoped region corresponds to yellow-brown curves; R_S curves corresponding to the optimal doping level are plotted in thick green lines. [94].

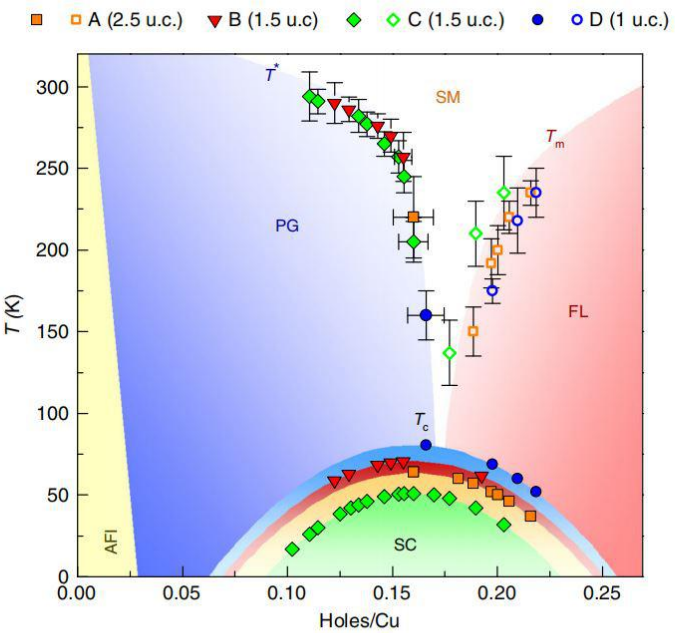

Figure 1.16: Phase diagram of 2D space charge doped BSCCO-2212. The characteristic temperatures T^* (filled symbols), T_m (open symbols), and T_c (filled symbols on the domes), extracted from 26 sheet resistance curves $R_S(T)$ measured on four thin BSCCO-2212 devices (labelled A, B, C, D), are plotted as a function of doping (holes/Cu). They demarcate the boundaries of the pseudo-gap region (PG), the strange metal region (SM), the Fermi liquid region (FM), and the superconducting dome (SC). The different colors of the domes reflect the shrinking of the dome with disorder. [94]

Here in Fig. 1.15 and 1.16, I also present the previous work from our group, which provides an overview of the $R_S(T)$ characteristics as a function of space charge doping for four ultra-thin BSCCO-2212 samples (1-2.5 unit cell) [94]. The doping method will be explained in detail in chapter 2. About 30 temperature dependence of sheet resistance curves $R_S(T)$ are recorded with these four BSCCO-2212 devices. T^* and T_m are extracted from the temperatures corresponding to the deviations in linearity of the sheet resistance curves to determine the domain of existence of the different phases in the underdoped and overdoped regimes respectively. T_c are taken as the temperatures where R_S goes to zero. This phase diagram establishes remarkably coherent and well-demarcated domains corresponding to the well-known cuprate phase diagram.

1.3.2 In-plane Hall coefficient

The Hall coefficient R_H along the in-plane direction is an important parameter to obtain information on the carrier densities. However there are problems for correlating R_H with the carrier density in high T_c and in many other materials, due to their complex physics

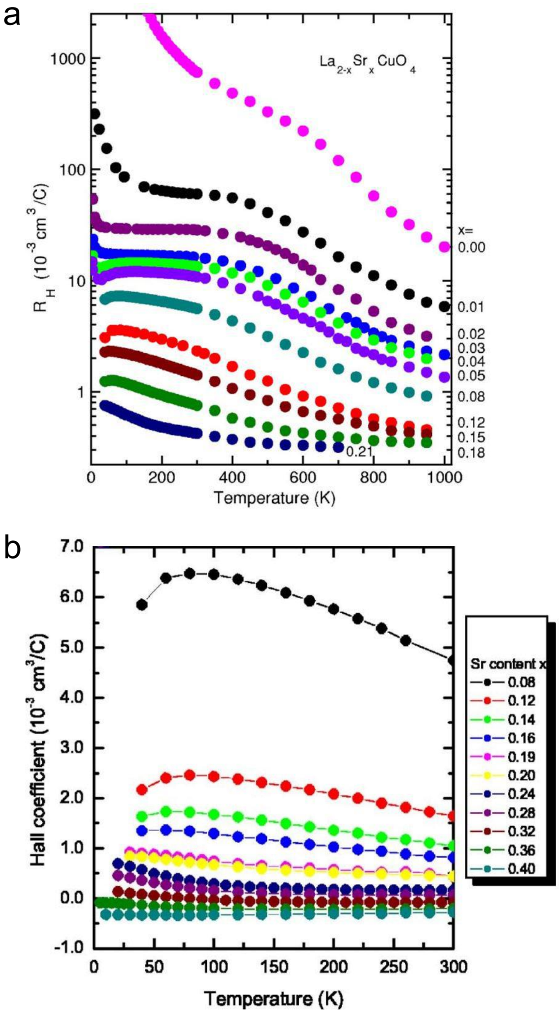

Figure 1.17: Temperature dependence of Hall coefficient R_H. **a** Hall coefficient R_H as a function of temperature up to 1000 K for doping level between 0 - 0.21 on a series of high-quality single crystal LSCO samples grown by the traveling-solvent floating-zone method; the data are obtained by sweeping the magnetic field between ± 6 T at each fixed temperature [95]. **b** Temperature dependence of R_H measured on thin film LSCO grown by the pulsed laser deposition technique with low-pressure pure ozone as an oxidant. The data are gotten by sweeping the magnetic field between ± 1 T for $0.08 \leq x \leq 0.22$, and ± 6 T for $0.24 \leq x \leq 0.40$ [96].

structure. More details about the relation between the hall coefficient and carrier density are given in chapter 2, section **2.3.2**. Fig. 1.17 presents the temperature dependence of the Hall coefficient R_H for a wide range of doping levels, varying from 0 to 0.40 on hole-doped thin film LSCO single crystals [95, 96]. As shown in these figures, R_H varies clearly with both T and doping level p (or x).

Can this temperature and doping dependence behaviour be a clue to understanding the underlying physics in cuprates? By analysing the data in Fig. 1.17**a**, Ono and coworkers [95] found that at x=0, the behaviour of R_H is quite easy to understand by considering the strongest electron correlation effects in the parent insulator LSCO, which leads to the Mott gap. Then at low doping level (0 ≤ x ≤ 0.05), $R_H(T)$ shows a remarkable decrease at high temperature. They proposed that this decrease may be due to the thermally activated charge carriers over a gap, indicating that strong charge fluctuations exist in slightly doped cuprates at high temperature. At higher doping level (0.08 ≤ x ≤ 0.21), the data present qualitatively the same behaviour but not as clearly. Another publication discussed the behaviour of temperature dependence of the in-plane hall coefficient $R_H(T)$ at higher doping level, from 0.08 to 0.40, as seen in Fig. 1.17**b** [96]. Tsukada *et al.* discovered that $R_H(T)$ is nearly temperature independent around 300 K at $x \geq 0.24$. Besides, $R_H(T)$ changes gradually from positive to negative at x = 0.28-0.32, which means that cuprates can be continuously n-doped to the electron-dominant regime. Moreover, the superconducting behaviour vanishes for $x \geq 0.32$.

1.4 The work presented in this thesis

In this thesis I have worked on devices of one unit-cell BSCCO and measured transport properties of these devices as a function of temperature and space charge doping. The bulk crystal material was provided by Prof. Dr. Andreas Erb at the Walther Meissner Institut für Tieftemperaturforschung of the Bayerische Akademie der Wissenschaften in Garching. All devices and measurements were made by me and simulations of Chapter 4 were performed by Johan Biscaras. Below I give a short description of the following chapters.

In Chapter 2, the methods and techniques used for ultra-thin BSCCO-2212 layers fabrication, sample characterization, and device fabrication are presented. The electronic transport measurements, including van der Pauw measurements, Hall measurements etc, are explained. The principle of the electrostatic doping method, which is called space charge doping, is as well described in chapter 2. A brief introduction to the experimental apparatus is also included.

In Chapter 3, we established Superconductor-Insulator Transition (SIT) as a function of doping in two dimensional BSCCO-2212 by space charge doping. The related critical parameters are determined, and a reliable way to estimate doping in the non-superconducting region is also discussed in chapter 3.

In Chapter 4, first a brief introduction on the superconducting transition and the underlying information extracted from its sheet resistance curves is given. Then I will discuss the effects of inhomogeneity and fluctuations on the superconducting transition in 1 unit-cell BSCCO-2212 both with simulations and with analysis of experimental results on the optimally doped 1 unit-cell BSCCO-2212 samples.

In Chapter 5, I will concentrate on the superconducting transition both on the overdoped region and the underdoped region of 1 unit-cell BSCCO-2212 samples. Especially, I will discuss how superconducting fluctuations are affected by doping.

Chapter 2

Experimental part

In this chapter, the methods and techniques used for ultra-thin BSCCO-2212 layers fabrication and electronic transport measurements are presented. A brief introduction to the experimental apparatus is also included. The first section is about the fabrication and characterization of thin layer BSCCO-2212. Then the second section how introduces how the samples are build into a device. The techniques and instruments about transport measurements and space charge doping technique are discussed in the third and fourth section respectively.

2.1 Sample fabrication and characterization techniques

2.1.1 Anodic bonding technique

Anodic bonding is the technique used in our laboratory for the fabrication of thin layer samples. This technique has been successfully applied to fabricate ultra-thin graphene, GaSe, GaS, InSe, MoS_2, BSCCO on glass substrates[97, 98, 99, 100]. This is an effective method for fabricating large area 2D samples with a lateral size up to hundreds of microns. Before the explanation of the principle of anodic bonding, I will first give a brief introduction on the glass substrates that we use.

Glass substrate

The substrates used in this thesis are all made of soda-lime glass. The main structure of soda-lime glass is an amorphous network of about 70 % silicon dioxide (SiO_2). Sodium and calcium atoms are generally introduced during fabrication in the form of sodium oxide (Na_2O) and calcium oxide (CaO), which can result in the breaking of some Si-O-Si bridges [101]. The cations Na^+ and Ca^{2+}, which serve as network modifiers, are compensating the charge of the non-bridging oxygen atoms. The divalent alkaline-earth ions is more strongly bound to the network than the monovalent alkali ions. Thus in the case of soda-lime glass, the mobility of Na^+ is considerably higher than that of Ca^{2+} [101]. Fig. 2.1 shows a schematized structure of soda-lime glass as discussed above.

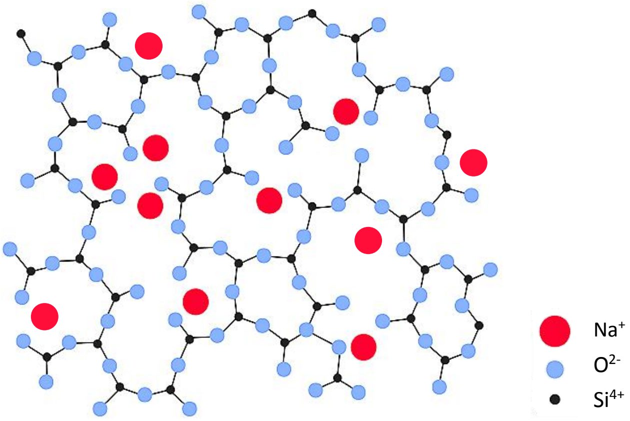

Figure 2.1: The main atomic structure of soda-lime glass.

Anodic bonding

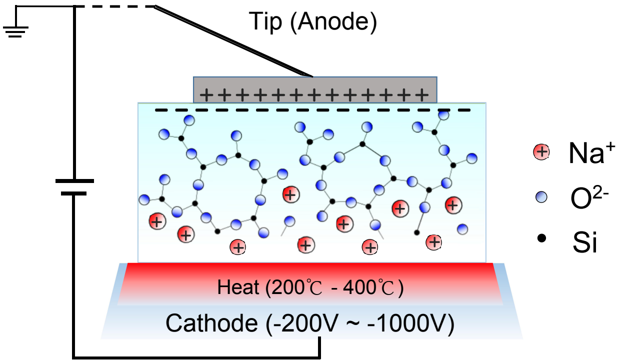

Figure 2.2: Schematics of anodic bonding principle.

The anodic bonding was first used to bond silicon wafer to a Pyrex substrate without any intermediate glue [102]. Fig. 2.2 shows the principle of anodic bonding technique. At high temperature (200 °C - 400 °C), the mobility of Na^+ ions is activated by thermal energy. By applying a negative voltage (-200 V $\sim$ -1000 V) at the back side of the substrate, mobile Na^+ ions will migrate across the substrate and accumulate at the cathode side of the system. The static oxygen ions left behind forms a negative space charge at the surface of the glass and a corresponding positive charge in the wafer. Thus a high electrostatic field is created at the interface of the glass/wafer, which can “stick” the thin layer material on the glass. In the case of glass/Si, chemical bonds Si-O-Si are formed at the interface [103].

Inspired by this technique and with a similar principle, our lab has successfully fabricated large size single and few layer graphene from bulk graphite precursor [103]. Then other thin and large-area samples, such as GaSe, GaS, InSe, MoS_2, BSCCO, are obtained in our lab [98]. The quality of the different fabricated samples have been studied by optical microscopy, atomic force microscopy and Raman spectroscopy, showing that the samples are free from chemical changes and all with good optical contrast [98, 99, 100, 103, 94]. For this thesis, I will focus on the fabrication of 2D BSCCO-2212 samples with anodic bonding technique.

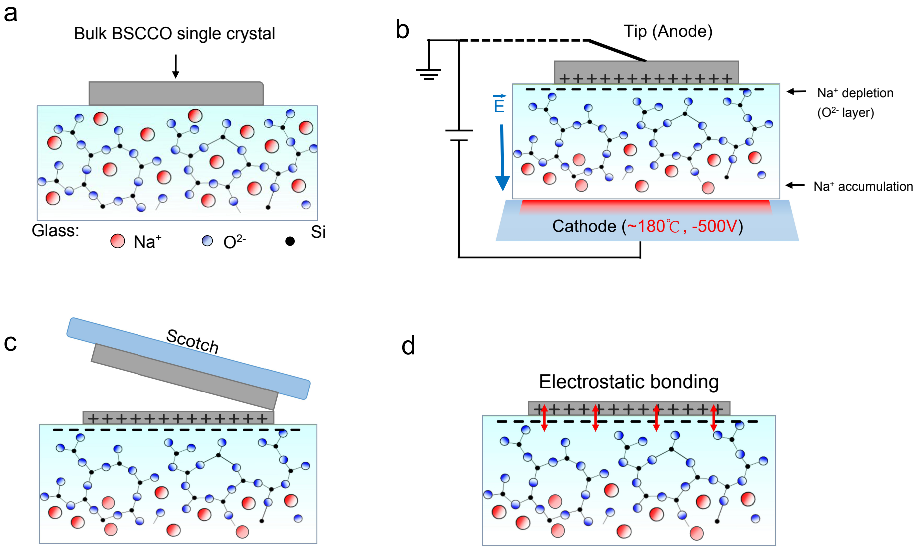

Figure 2.3: Schematic view of sample fabrication procedure. **a** BSCCO-2212 bulk single crystal precursor is deposited on the soda-lime glass substrate. **b** The glass/sample is placed on the anodic bonding machine heated to about 200 °C, and a negative voltage about -500 V is added at the cathode for a few minutes. **c** After anodic bonding process, the bulk precursor is exfoliated with a soft adhesive tape. **d** The ultra-thin BSCCO-2212 layer is left on the glass substrate due to the electrostatic field induced by anodic bonding.

Fig. 2.3 shows briefly the procedure of the fabrication of 2D BSCCO samples. The substrate used here is soda-lime glass, as mentioned above. All the substrates are cut into small square pieces with the size of about 8 mm x 8 mm, and then cleaned in an ultrasound bath with acetone and ethanol for 5 minutes respectively at around 45 °C. After drying with nitrogen flow, the substrate glass is put on a hot plate ($\sim$ 100 °C), and a thin precursor, exfoliated from bulk BSCCO-2212 with a soft adhesive tape, is deposited on the top of the glass. The glass is then put on the anodic bonding device, between two electrodes with an anvil below and a tip above, which has been heated to 180 °C to make Na^+ ions mobile. After that, a negative voltage, (-450 V $\sim$ -500 V) is applied at the cathode, so that the mobile Na^+ ions can drift towards the back side of substrate, creating a negative space charge at the glass/material surface. This negative space charge induces a positive charge in the sample, thus leading to an electrostatic field, which can bind the thin BSCCO-2212 samples on the glass substrate. The whole bonding process takes 10 minutes. Then the voltage is removed and the glass/material is cooled down to room temperature. After the bonding, the upper layers of the precursor material are exfoliated with a soft adhesive tape, leaving few-layer samples of the material on the glass surface.

2.1.2 Optical microscopy

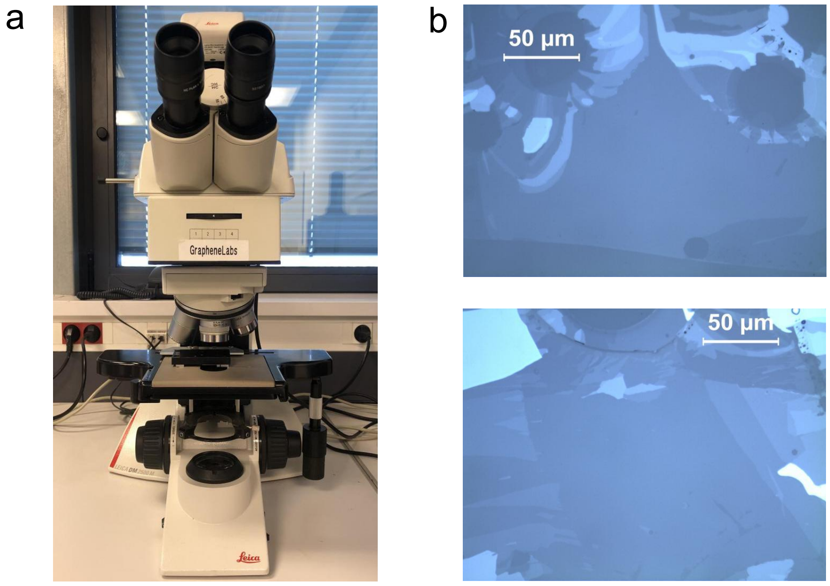

Figure 2.4: Optical microscope **a** Optical microscope set-up. **b** 1 unit cell BSCCO sample photos taken by optical microscope **a** with objective 50x.

Optical microscope provides us a direct view of the samples fabricated with anodic bonding technique. Fig. 2.4 **a** shows the equipment we used in our lab, which is with a Leica DM2500 with objectives of 5x, 10x, 20x, 50x, 100x and a CCD camera. BSCCO-2212 fabricated by anodic bonding has always shown a good optical contrast, which makes their identification and location very easy. Fig. 2.4 **b** shows the figures taken by optical microscope of some ultrathin layers of BSCCO-2212 obtained in our lab. They are of good quality, which means that the samples are homogeneous and with large area. For BSCCO, the samples are usually multiple of half unit-cell, because they cleave between the weakly bound BiO layers. The thickness can be measured more precisely by atomic force microscope. After several years' of fabrication of ultra-thin BSCCO, the number of layers of a BSCCO sample can be figured out directly by observing with optical microscope.

2.1.3 Atomic Force Microscopy (AFM)

Atomic force microscopy, as a kind of scanning probe microscopy, was first invented in 1986 by Binnig, Quate and Gerber [104]. It is an instrument which allows to visualize the topography of the surface down to atomic resolution, which is more than 1000 times better than the optical diffraction limit. As shown in Fig. 2.5, an AFM consists in a micro-fabricated tip placed at the end of a cantilever and an optical system with a laser for the detection of the cantilever's deflections, which are caused by the forces between the tip and the sample surface according to Hooke's law [105]. The tip and the forces are controlled by the feedback system. The sample is positioned on a piezoelectric scanner, which can moves in the z direction to control the sample's distance from the probe and in the x and y direction for scanning. When the tip gets close to the sample and moves along the sample surface, the laser deviation on the photo-diode detector is used in the feedback loop to track the surface for imaging and measuring the sample's height profile.

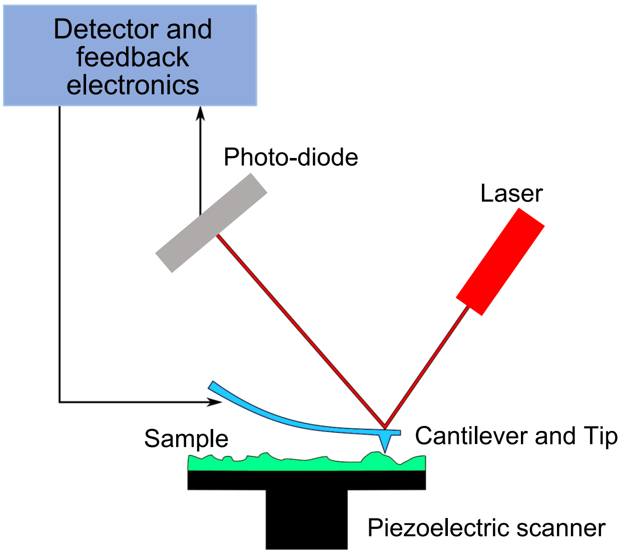

Figure 2.5: Schematic view of AFM.

According to the nature of the tip motion, there are usually three described imaging modes with an atomic force microscope: contact mode, non-contact mode and tapping mode (or AC mode). In contact mode, the forces between the tip and the sample surface are repulsive. A constant cantilever deflection is maintained by the feedback system. Considering that the tip is in hard contact with the sample surface, the stiffness of the

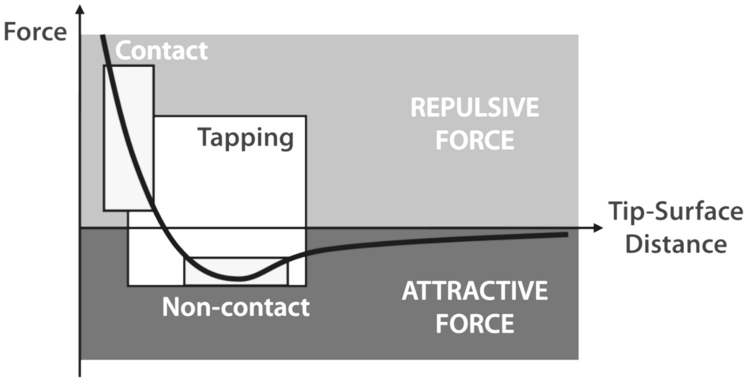

Figure 2.6: Operation regimes for contact mode, non-contact mode and tapping mode.

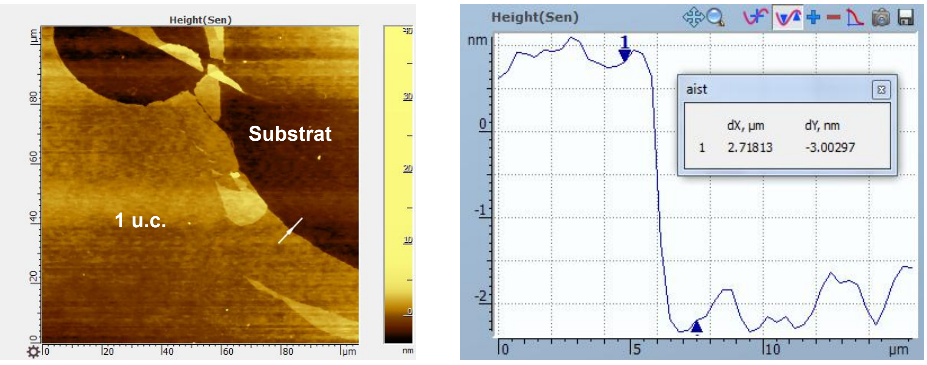

	dX, µm	dY, nm
1	2.71813	-3.00297

Figure 2.7: **Left:** image of 1 u.c. BSCCO-2212 sample taken by atomic force microscope. **Right:** Height profile along the white arrow on the left photo, pointing from the BSCCO layer to the glass substrate. The thickness appears to be ~ 3 nm, which corresponds to that of 1 u.c. BSCCO-2212.

cantilever has to be soft enough (usually less than 1 N/m) to avoid damaging the probe tip and sample surface. In non-contact mode, the probe tip doesn't touch the sample surface. The cantilever is oscillated at or near its resonance frequency with a small amplitude of few nanometres (< 10 nm). The tip is kept typically several nanometres away from the sample surface so that the forces between the probe and the surface are attractive. The feedback loop system maintain a constant cantilever oscillation frequency or amplitude. This non-contact mode is preferable for the measurement of soft materials, because there is very low possible interaction between the surface and the tip. However it takes challenge to keep the probe tip in the attractive force region and requires high performance feedback control. The stiffness of the cantilever needed is with force constant higher than 25 N/m. In tapping mode, the cantilever is also driven to oscillate at or near its resonance frequency with a piezoelectric actuator. The difference from the non-contact mode is that in tapping mode, the cantilever has a larger amplitude, and the probe tip slightly touches the sample surface at the lower end of the cantilever oscillation. A constant cantilever oscillation amplitude is kept by the driven signal with constant frequency and amplitude. The dominant forces between the probe tip and the sample surface are repulsive (Fig. 2.6). Stiff cantilever with force constant of 10-100 N/m is needed for tapping mode. The damage to the surface and the tip is lessened compared to contact mode in ambient air. Fig. 2.7 shows the identification of ultra-thin BSCCO-2212 samples with tapping mode of AFM. In this thesis, all the identification work is accomplished with tapping mode.

2.2 Device fabrication

2.2.1 Gold contact deposition

After the fabrication of the ultra-thin layer BSCCO-2212 on the glass substrate, gold contacts are deposited on the sample with the aim of carrying out electronic transport measurements. To avoid un-necessary processing and contamination of the sample's surface we rejected any form of resin-based lithography to deposit the contacts. Hence, the contacts are deposited by using a 0.15 mm thick steel stencil mask with 4 laser-cut holes forming a van der Pauw geometry (Fig. 2.8). Each contact of the mask is made of a strip about 10 μm wide near the sample, which gets wider away from the center to allow wire-bonding (see below). In the center of the mask the end of the four contacts form a square with a diagonal length of about 50 μm. The mask is stuck on the sample with 0.1 mm thick double sided adhesive tape at the four corner (Fig 2.8). The deposition procedure is performed with an Edward thermal evaporator (Fig 2.8) in the clean room of École Normale Supérieure de Paris. This evaporator can provide a vacuum of 10^{-6} mbar. The chamber of the evaporator is a cylinder with a height of about 40 cm and a diameter of about 30 cm. The gold is placed in a tungsten crucible at the bottom of the chamber and heated with an electrical current to the evaporation temperature of gold. The samples with masks on them are fixed right above the crucible. Gold is chosen for the contact deposition due to its very low resistivity to reduce its influence on the low temperature transport measurement. The thickness of the gold deposition is about 70 nm.

After the gold deposition, the sample is further shaped with a tungsten needle controlled by a micro-manipulator under an optical microscope. The radius of the needle tip is $\sim$10 μm. This step is to conform the shape of the sample to the cloverleaf van der Pauw geometry and to destroy unwanted connection from other flakes left on the glass during the anodic bonding. This basic technique of shaping was chosen as to avoid further un-necessary processing such as plasma etching that could compromise the sample quality. Fig. 2.9 shows some shaped BSCCO-2212 samples with gold contacts on them.

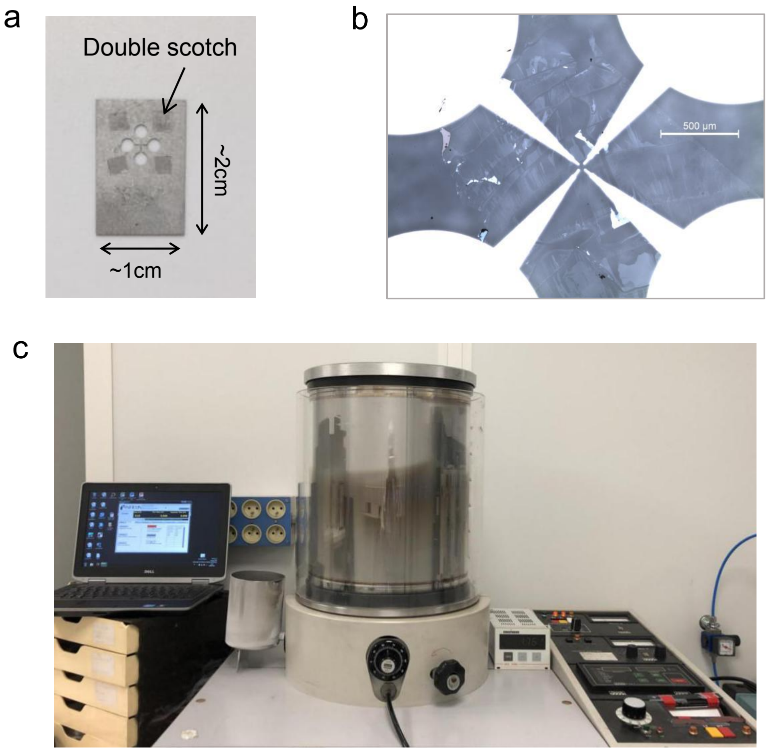

Figure 2.8: **a** Steel stencil mask in van der Pauw geometry. **b** 1 u.c. BSCCO-2212 sample with ∼70 nm thick gold contacts on it. The image is taken by the optical microscope introduced in this chapter with objective of 5x. **c** Photo of the Edward thermal evaporator.

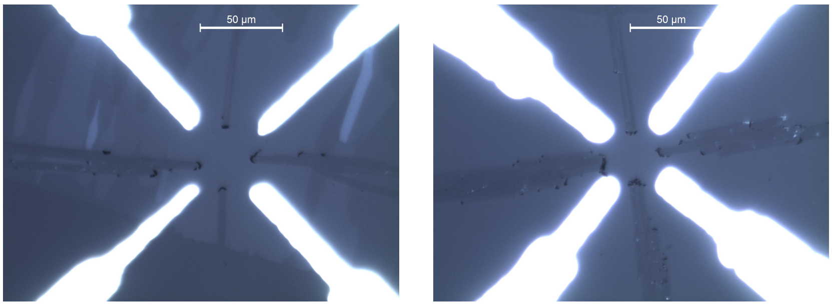

Figure 2.9: Optical images of scratched 1 u.c. BSCCO-2212 samples with objective 50x. Scratches by tungsten needle can been clearly observed on the photos.

2.2.2 Sample Mounting and Wire bonding

To perform transport measurements and apply a back gate for space charge doping (see next section) the samples are glued with conducting silver paste to an insulating MgO substrate covered with an evaporated gold film. The gold film act as a back-gate, while the MgO is a spacer to isolate the back-gate from the sample holder. The MgO with the sample on top is then glued with silver paste to the sample holder.

Wire bonding is used for making interconnections between the gold contacts on the sample and the electrical pads on the sample holder. It is the very last step for device fabrication before the transport measurements.

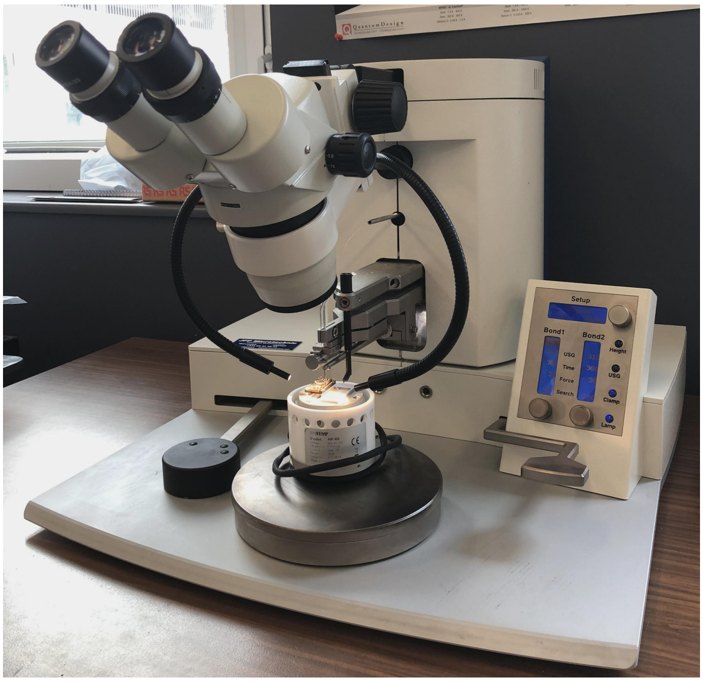

Figure 2.10: Photo of the wire bonding machine used in this thesis.

Fig. 2.10 shows the wire bonding machine WB-100 wire bonder. This WB-100 wire bonder employs the basic ultrasonic bonding method. The wire chosen here is aluminium wire. Bonding two metals using the ultrasonic method results from three variables: force, ultrasonic energy and time. Force is introduced to promote plastic flow (deformation) and intimate coupling between the bonding tool, the wire and the substrate. Ultrasonic (62 kHz) scrubbing displaces surface contamination and insures metal to metal coupling. Time is set long enough to cause solid state diffusion.

2.3 Transport measurement

2.3.1 Sheet resistance and van der Pauw measurement

Sheet resistance, also known as surface resistance, is an electrical property usually used to measure the resistance of thin samples with uniform thickness and is suitable for 2D system such as our one unit-cell BSCCO-2212 samples. Sheet resistance is commonly defined as the ratio between the resistivity (ρ) of a material and its thickness (t):

$$R_S = \frac{\rho}{t} \tag{2.1}$$

The common units used is $\Omega/\Box$ (ohms per square) as R_S has the dimension of a resistance. Sheet resistance is usually measured with four-point measurements techniques to avoid measuring the contact resistance. For BSCCO-2212 few layers samples, we have adopted the van der Pauw geometry.

The van der Pauw method, which is a kind of four-point measurement, is first introduced by Leo J. van der Pauw in 1958 [106]. It's a widely used technique for the measurements of the resistivity and the Hall coefficient of samples in two dimensions. The samples can adopt an arbitrary shape in the condition that they are homogeneous, isotropic, uniform in thickness and without any isolated holes. In the original van der Pauw design, the four contacts need to be located around the perimeter of the sample, and each of them should be sufficiently small compared to the whole area of the sample. However, in our experiments we use a cloverleaf geometry that allows for larger contacts that are not strictly on the edge of the flake.

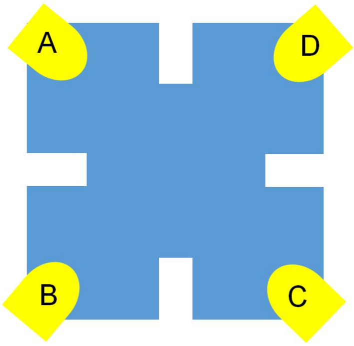

Figure 2.11: Schematic of the van der Pauw geometry used in this thesis. A, B, C, and D represent four gold contacts.

Fig. 2.11 shows the configuration of the van der Pauw geometry used in this thesis.

To determine the sheet resistance R_S of the sample, firstly a current is injected to flow from contact A to contact B I_{AB}, and the voltage $V_{CD} = V_D - V_C$ is measured. Then the current is injected from contact B to contact C I_{BC}, and the voltage $V_{DA} = V_A - V_B$ is measured. Thus the resistances R_1 and R_2 are defined using Ohm's law:

$$\begin{aligned} R_1 = R_{AB,CD} = \frac{V_{CD}}{I_{AB}} \\ R_2 = R_{BC,DA} = \frac{V_{DA}}{I_{BC}} \end{aligned} \tag{2.2}$$

The sheet resistance R_S of the 2D material is related to the two resistances R_1 and R_2 by the relation:

$$e^{-\frac{\pi R_1}{R_S}} + e^{-\frac{\pi R_2}{R_S}} = 1 \tag{2.3}$$

This solution of equation (1.2) can be written in the form:

$$R_S = \frac{\pi}{ln(2)} \frac{R_1 + R_2}{2} f(R_1/R_2) \tag{2.4}$$

where $f(R_1/R_2)$ is a geometric factor depending on the measured electrical anisotropy of the sample which cannot be derived analytically, but can be calculated numerically [107]. This factor can be determined for $1 \leq R_1/R_2 \leq 10^4$ with high precision by the following equation [108]:

$$cosh(\frac{R_1 - R_2}{R_1 + R_2} \frac{ln(2)}{f}) = \frac{1}{2} exp(\frac{ln(2)}{f}) \tag{2.5}$$

However, for our measurements with $1 \leq R_1/R_2 \leq 10^2$ a polynomial approximation can be used.

2.3.2 Hall measurement

As mentioned above, the van der Pauw geometry can also provide possibility for Hall measurement, so that the Hall carrier density and Hall charge mobility can also be extracted from this method. When a magnetic field **B** is applied perpendicularly to a 2D conducting material, where there is an electric current flowing through, the charges of the electric current will experience a Lorentz force F_m. For the electrons, the value of the Lorentz force is:

$$F_m = evB \tag{2.6}$$

where v is the drift velocity of the electrons. This Lorentz force, induced by the magnetic field, will push the electrons to one side of the conductor, as shown in Fig. 2.12. Then to balance this magnetic effect, the buildup of charges at the two sides of the conductor will produce a voltage, which is called Hall voltage U_{Hall}, between the two sides of the material, thus inducing another electric force F_e which is written as:

$$F_e = e\frac{U_{Hall}}{l} \tag{2.7}$$

where l is the width of the 2D material (Fig. 2.12). When the magnetic force and the electric force are balanced, the Hall voltage can be deduced:

$$U_{Hall} = vBl \tag{2.8}$$

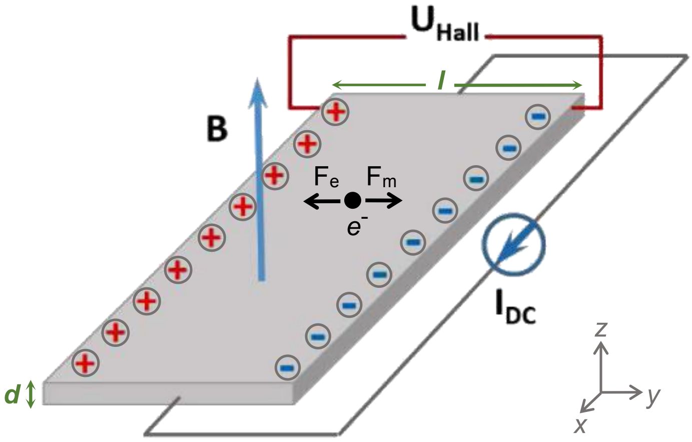

Figure 2.12: Schematic view of the Hall effect in a 2D conducting layer.

Considering the current I expressed in terms of the drift velocity $I = env(ld)$ (n the density of mobile charges per volume of the space, d the thickness of the conductor, and ld the cross-section area), we extract the Hall voltage to be:

$$U_{Hall} = \frac{BI}{ned} \tag{2.9}$$

In 2D samples, it is preferable to use the sheet charge density $n_S = nd$. Therefore the Hall resistance

$$R_H = \frac{U_{Hall}}{I} = \frac{B}{en_S} \tag{2.10}$$

Here n_S can also be called the Hall sheet carrier density, or n_H. The Hall voltage sign is determined by the charge polarity, because the voltage, the current and the magnetic field form a direct trihedron.

However in cuprates, the relation between R_H and n_S is not as simple as in equation 2.10 because of the complex electronic band structure of these materials. Thus the Hall sheet carrier density n_H is different from the real sheet carrier density n_S, which should be equivalent to the number of holes in the CuO_2 planes (a.k.a. the hole doping level p). As reported in the literature, we have found that the Hall resistance in thin BSCCO-2212 is temperature and doping dependent [109]. The maximum of R_H at optimal doping is found around 120 K [110], so we consider the values of R_H at this temperature to estimate semi-quantitatively the variation in carrier density after each doping performed.

In practice, Hall measurements for BSCCO-2212 are carried out at 120 K with a magnetic field sweeping between ± 2 T. In the van der Pauw geometry the Hall voltage is measured by injecting the current between two opposite corners of the square and measuring the voltage between two others. We measure the two possible configurations and take their average to eliminate sheet resistance contributions to the measured voltage. The Hall carrier density n_H is deduced from the slope of R_H as a function of B.

Combining sheet resistance and Hall measurements allows to calculate the mobility of charge carriers. We first write the drift velocity of electrons $v = \mu E$, where E is electric field along the direction of the current I. Then following the expression of $I = env(ld) = en_S vl$ we can write:

$$I = en_S \mu \frac{l}{L} U = \frac{l}{L} \frac{U}{R_S} \tag{2.11}$$

with L being the length of the material along the direction of the current and U the voltage drop in that direction. Combined with the equation (2.10), the Hall mobility μ_H is calculated as:

$$\mu_H = \frac{1}{en_H R_S} \tag{2.12}$$

2.3.3 Transport measurements apparatus

All the transport measurements are carried out in the apparatus shown in Fig. 2.13. The sample is fixed at the bottom of the blue cryostat, which is inserted in the middle of a 2 T electromagnet. The vacuum of the chamber can be pumped to less than 10^{-6} mbar. Liquid He flow is used to cool down the temperature, and a resistive heater is used to increase or stabilize the temperature. The temperature of the system can be controlled in the range from 3 K to 420 K. Excitation current injected into the sample and the gate voltage applied at the back side of the sample/glass are provided by two Keithley 2400 source-meters (Fig. 2.13). The 4-Wire voltages are measured with a Keithley 2700 data acquisition multimeter equipped with a Keithley 7709 matrix relay card to switch between the different van der Pauw/Hall configurations.

For transport measurements, sheet resistance curves are recorded usually from 330K to the temperature below T_c of the material in case of a superconductor, or to the minimum temperature limit of the system ~ 3 K. All the data, including the four-wire resistance, two-wire resistance, gate voltage, gate current, correction factor, and sheet resistance are recorded. Then, Hall measurements are taken at 120 K by sweeping the magnetic field between ± 2 T. The space charge doping is performed at a fixed temperature between 350 K - 400 K with the gate voltage in the range between ± 285 V.

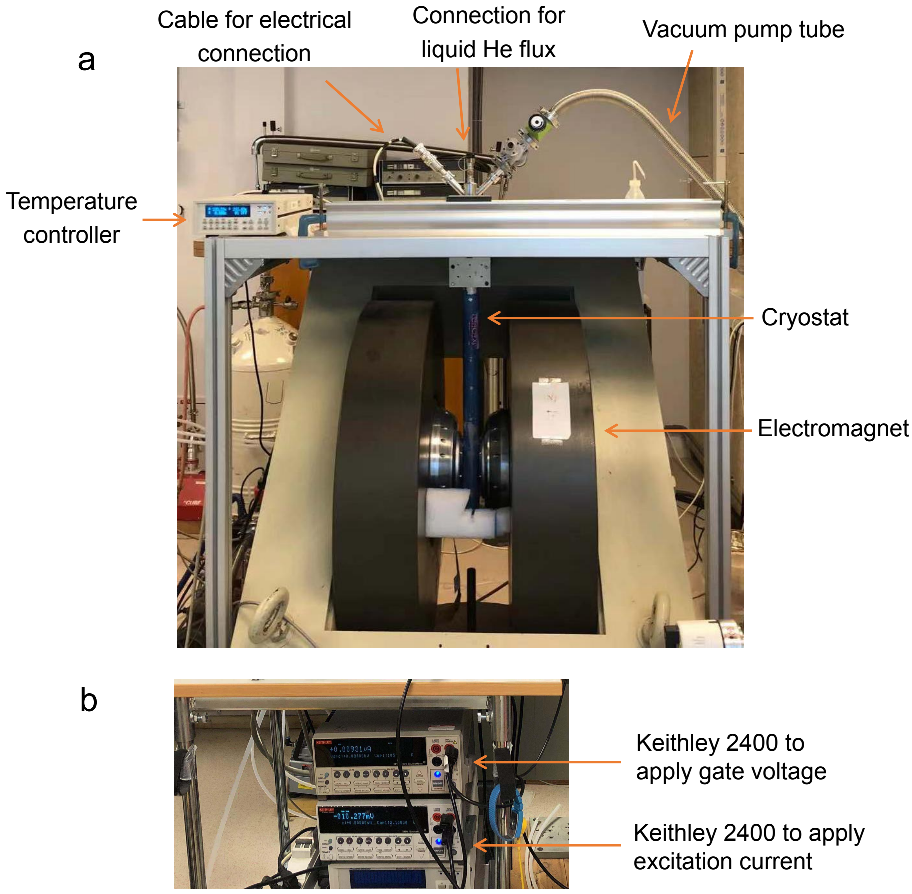

Figure 2.13: Set-up photos. **a** Photo of the apparatus used for the transport measurements. **b** Keithley used in this thesis: the top one is used to apply gate voltage on the back side substrate and measure the gate current; the lower one is to inject excitation current into the sample from each gold contact and measure the voltage between gold contacts of the sample.

2.4 Space charge doping

Space charge doping is a kind of high density electrostatic doping technique which is first introduced by our group in 2015 [100, 111]. Its main idea is to dope two-dimensional materials by exploiting the movement of the mobile ionic species (Na^+ in our case) in the substrate. It is a much simpler, "cleaner" and more efficient way to dope two-dimensional samples, compared to the chemical doping method, as it will neither introduce new species into the material, nor will it change the sample's structure. Using an ionic liquid as a dielectric is another electrostatic way to dope two-dimensional materials, which has been applied to other cuprates such as YBCO [82] and LSCO [80]. However, recent studies have then discovered that the ionic liquid Field-Effect Gating can cause oxygen displacements in cuprates [112]. The space charge doping method avoids problems which may arise in liquid dielectrics, ensures all measurements on a single, low disorder, good quality sample, and removes the sample dependent uncertainty that comes from chemical doping. Furthermore, the space charge doping technique can dope the sample in a reversible way without destroying the sample. Doping densities $> 10^{-14}$ cm^{-2} have been reached in two-dimensional graphene [111], MoS_2 [100] and BSCCO-2212 [94].

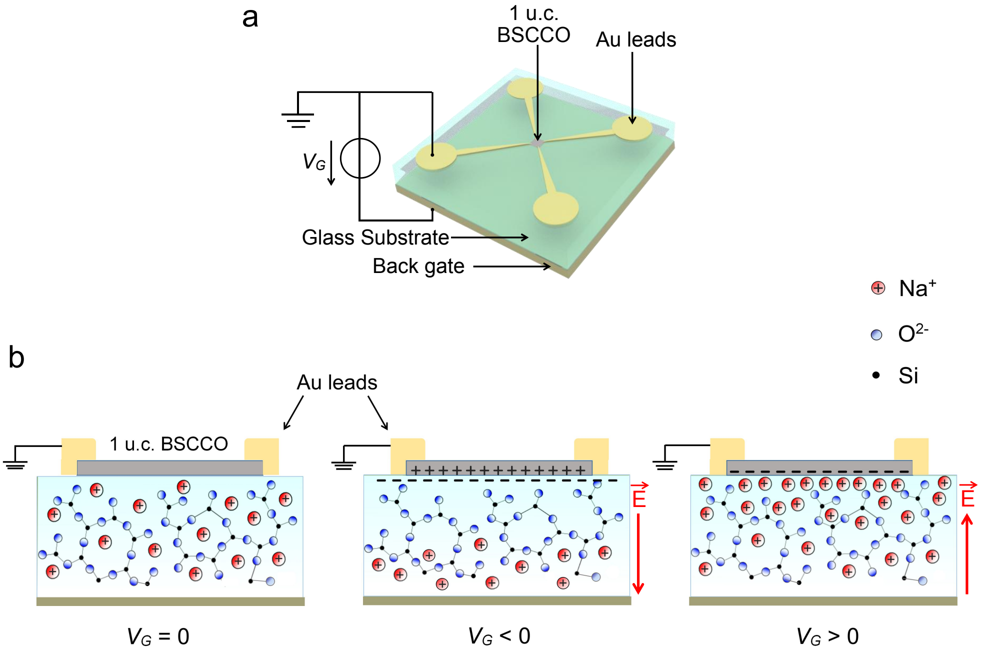

Figure 2.14: Space charge doping technique. **a** Schematic view of the device. **b** Illustration of the principle of space charge doping technique. Details are explained in the main text.

The space charge doping method is actually an extension of the anodic bonding technique, which has been introduced in the former section. Fig. 2.14 explains schematically the principle of the space charge doping. The substrate is again soda-lime glass, where there are plenty of mobile Na^+ ions. At room temperature, all the sodium ions are uniformly distributed inside the glass, bounded with the non-bridging oxygen atoms (Fig. 2.14 **b**). By increasing the temperature to 350 K - 400 K, the mobility of the Na^+ is activated by thermal energy. Thus the soda-lime glass can be considered as a negatively charged matrix of SiO_2 with massive positively charged Na^+ ions. Then if a negative gate voltage is applied at the back side of the glass substrate, all the mobile Na^+ ions will drift towards the bottom of the substrate under the influence of the electric potential difference. This movement of Na^+ ions creates a negatively charged space layer below the interface as shown in Fig. 2.14 **b**. This negative space charge induces a mirror positive charge inside the sample, so that the sample is p-doped (or hole-doped). Similarly, to n-dope (or electron-dope) the sample, a positive gate voltage is added at the back side of the substrate. The electric potential difference pushes the mobile Na^+ ions towards the sample/glass interface, and creates an accumulation layer of Na^+ ions below the interface. This positively charged accumulation Na^+ ions layer induces a negative charge in the sample, which is n-doping (or electron-doping). The doping can be controlled by changing the temperature (from 305 K to 400 K), gate voltage (between ± 285 V) and the time (from several minutes to hours). This also indicates that the mobility of Na^+ ions remains relatively small in our experimental case. By cooling down to room temperature or below, the mobility of the Na^+ ions and the drift current will exponentially decrease, thus "freezing" the Na^+ ions (and the doping) inside the glass matrix.

This space charge doping technique has been successfully applied on graphene [111], on MoS_2 for Metal-Insulator transition [100], and on two-dimensional BSCCO-2212 for the construction of the phase diagram around the optimal doping level [94].

Chapter 3

Superconductor-Insulator Transition in space charge doped one unit cell $Bi_{2.1}Sr_{1.9}CaCu_2O_{8+x}$

In this chapter we will establish and investigate the nature of the superconductor-insulator transition as a function of doping in two dimensional $Bi_{2.1}Sr_{1.9}CaCu_2O_{8+x}$ (BSCCO) and deduce the scaling parameters associated with this quantum phase transition. This work has been published in [113].

3.1 Introduction

A superconductor-insulator transition (SIT) in two dimensions is a continuous quantum phase transition (QPT) at absolute zero temperature [114, 115] driven by external parameters like disorder, magnetic field or carrier concentration [81, 6, 116, 117, 80, 82, 94, 110, 53].

Such transitions have been induced in a variety of 2D superconductors by tuning different external parameters and studied with a finite-size scaling analysis. There is however not much uniformity in the findings as both the superconducting systems and the tuning parameters are diverse. Magnetic field is a common, easily tunable and accessible external parameter. Magnetic field driven SIT studies have reported a large variety of critical exponents and resistance at criticality: from $\nu z \sim$0.67 and R_c =1.3 kΩ in NbSi thin films [83] to $\nu z \sim$2.3 and R_c = 6 kΩ in Indium oxide thin films [84]. Furthermore, in quenched condensed bismuth thin films the magnetic field driven SIT was shown to have $\nu z \sim 0.7$ and $R_c = 8$ kΩ, while the thickness driven SIT displayed $\nu z \sim$1.2 around the same critical resistance, indicating a fundamental difference in their nature [81]. It is therefore difficult to come to a general conclusion about the SIT in different systems and induced by different tuning parameters. The high critical magnetic fields of most high critical temperature superconductors renders the study of the magnetic field driven SIT difficult (with the exception of the electron doped cuprate NdCeCuO [85]). However, improvements in extreme electrostatic doping techniques have provided access to the carrier density driven SIT in $La_{2-x}Sr_xCuO_4$ (LSCO) and $YBa_2Cu_3O_{7-x}$ (YBCO).

Tuning carrier density is an effective way to realize this transition by chemical or electrostatic doping methods. Chemical doping, the usual and only possible method in bulk samples, has been widely used in high critical temperature superconductors, both in bulk and thin films [118, 53]. However it is sample dependent and can lead to disorder and structure change. Electrostatic doping is the method of choice to obtain a continuous and defect free change in doping in the same ultra-thin sample in a field effect transistor device [119, 80, 82]. Both the correlation length ϵ and correlation time τ corresponding to a phase transition are dependent on the variation of an external parameter x with respect to a critical value x_c. In our case this is the variation of the carrier concentration p with respect to the critical doping at the phase transition p_c with, $\epsilon \propto |p - p_c|^{-\nu}$ and $\tau \propto \epsilon^z$ where ν is the correlation length exponent and z is the dynamical-scaling exponent. The variation of physical quantities like sheet resistance across the phase transition in a transport measurement can be expressed in terms of these asymptotic forms and a single 'scaling' formula dependent on $|p - p_c|^{-\nu z}$. If the effects of the QPT persist at experimentally accessible, small, but non-zero temperatures, it can be characterized by its universality class given by the numerical value of νz, the product of the finite-scaling exponents. This value, along with the critical values of the driving parameter (doping) and the measured physical quantity (sheet resistance), consitutes the fundamental information that can be gleaned from a quantum phase transition in reduced dimensions and has been used in the past for studying high T_c superconductors [80, 82, 53].

In this chapter we establish and investigate the nature of the SIT as a function of doping in two dimensional $Bi_{2.1}Sr_{1.9}CaCu_2O_{8+x}$ (BSCCO) and deduce the scaling parameters associated with this QPT. This measurement has been rarely accomplished, always with considerable experimental process. The QPT has been shown to exist in two of the principal families of high T_c compounds, LSCO [80] and YBCO [82] using ultra-thin samples and electrostatic doping. In BSCCO a recent result in single layer (i.e. half unit cell) samples [53] is remarkable but uses chemical doping with ozone. Here we accomplish electrostatic doping with our novel space charge doping technique on a one unit cell (1 u.c.) BSCCO device and indeed observe a QPT. Earlier theoretical work [7] predicted the existence of a material-independent quantum critical resistance $R_Q = h/(2e)^2 = 6.45$ k$\Omega.\square^{-1}$ for the insulator-superconductor transition. Experimental results from the above works show some scatter, with near universal critical resistance values in LSCO (6.4 kΩ) [80] and YBCO (6 kΩ) [82] but a variation of 2.8 to 10.2 kΩ in BSCCO [53]. The critical doping associated with this crossover varies significantly, from p_c = 0.05 - 0.06 holes/Cu [80, 82], the value expected from the generic phase diagram, to nearly 0.02 holes/Cu [53]. Finally the product of critical exponents νz also varies, with 1.5 in LSCO [80], 2.2 in YBCO [120] and between 1.5 and 2.4 in BSCCO [53]. Universality of the QPT should imply $R_c \sim 6.45$ kΩ, $p_c \sim 0.05$ - 0.06 and a similar value for νz in different materials. Thus establishing this benchmark in BSCCO is necessary and the measurement should avoid pitfalls from sample dependent imperfections which tend to overshadow material parameters.

A crucial aspect of this program is determining the doping since absolute determination of doping in high T_c compounds, whether bulk or few layer samples, remains elusive. The Hall coefficient is notoriously variable with temperature. In LSCO and YBCO [80, 82] the inverse sheet resistance at a fixed temperature well above the T_c is proposed as a measure of the doping p, presupposing simple Drude-like behavior with constant carrier mobility. An empirical relation, linking the dome shaped dependence of the critical temperature on doping [45, 121, 94], has also been used. Can this be extended to the strongly undoped non-superconducting region? We show here that it can and indeed gives a reliable, though not absolute, determination of doping which could profitably be used in future work.

3.2 Sample preparation and transport measurements

3.2.1 Sample preparation

$Bi_{2.1}Sr_{1.9}CaCu_2O_{8+x}$ precursors were exfoliated from bulk crystals (T_c = 89 K), and deposited on soda-lime glass with a thickness of 0.5 mm and with an area of ∼ 8 mm x 8 mm. Then anodic bonding technique, which is explained in chapter 2, was used to fabricate 1 u.c. BSCCO samples of ∼ μm lateral size. The precursor on the glass substrate is placed between two electrodes and heated to ∼ 180 °C to activate the Na^+ mobility (Fig. 2.2). On the application of a negative gate voltage (∼ 500 V) at the back side of the glass substrate, the Na^+ ions in the glass move away from the glass/sample interface, forming an O^{2-} space charge at the sample-glass interface. This space charge sticks the first few nm of the precursor electrostatically on the glass substrate. Adhesive tape is used to exfoliate the precursor. A large area ultra thin BSCCO sample, the thickness of which is evaluated by Atomic Force Microscopy and optical contrast, is left on the glass surface. The sample is then annealed in air to reduce its doping level by oxygen loss.

70 nm thick gold contacts were evaporated onto the sample through a steel stencil mask to achieve a van der Pauw geometry device after the annealing process. We have found that both lithography and Cr buffer layers degrade sample quality. Sample quality and the absence of contamination are checked through the R_S measurement. The glass substrate and device was then glued on to the backgate by silver paste (Fig. 2.16 **a**).

To determine the annealing parameters to reach an initial value for doping close to the superconductor-insulator transition, about 100 1 u.c. BSCCO samples were fabricated, and about half of them were chosen, due to their bigger size and better homogeneity, to put into the oven for trials of different annealing parameters. Bulk BSCCO samples need several hours of annealing in a predetermined atmosphere of partial pressure of oxygen well above 400 °C. A 1 u.c. sample should need a much shorter time and at a lesser annealing temperature because of the very small diffusion length corresponding to the sample thickness. Some of the annealing parameters, as well as the corresponding four-wire sheet resistance, are shown in Fig. 3.1. Here I also present the transport measurements of two 1 u.c. BSCCO samples. The first 1 u.c. BSCCO sample was annealed at 400 °C for 5 minutes in air (black curves in Fig. 3.2). This sample revealed an insulating behaviour. Strong hole doping with space charge failed to push it into the superconducting region. To obtain samples with higher doping 1 u.c. BSCCO samples were annealed in the oven at 350 °C for 1 minute (red curves in Fig. 3.2). However the sample chosen for transport measurements was still an insulator but came closer to the underdoped part of the phase diagram after strong hole doping. As shown in Fig. 3.2, the two lower red curves became much less insulating at low temperature. With these parameters however reaching the required doping value still needed trial and error. I finally found that 350 °C and 1 minute are most likely to reduce the sample doping to the superconductor-insulator transition point. I also came to the conclusion that whether the sample actually reaches this point depends not only on the parameters of the anneal, but also on the quality of the sample surface which is not very well controlled.

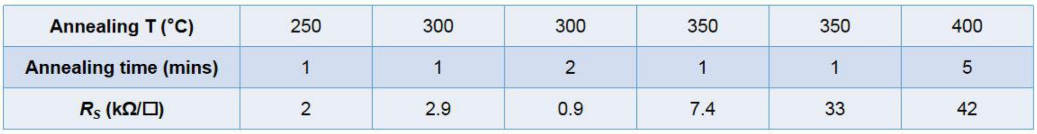

Annealing T (°C)	250	300	300	350	350	400
Annealing time (mins)	1	1	2	1	1	5
R_S (kΩ/□)	2	2.9	0.9	7.4	33	42

Figure 3.1: Table of some examples of the annealing parameters tried on 1 u.c. BSCCO samples and their corresponding sheet resistance.

3.2.2 Space charge doped one unit cell $\mathbf{Bi_{2.1}Sr_{1.9}CaCu_2O_{8+x}}$

Fig. 3.3 shows the sheet resistance curves R_S of another 1 u.c. BSCCO sample annealed at 350 °C for one minute in air. The four-point sheet resistance measured at room temperature increased to $\sim$ 7 kΩ.$\square^{-1}$ compared to $\sim$ 2 kΩ.$\square^{-1}$ measured in similar devices prepared without annealing.

The thick olive green curve indicates that the starting doping level p after annealing is indeed near the beginning of the superconducting dome. The corresponding critical temperature T_c (defined in this work as the temperature below which R_S vanishes) is near 10 K. The doping level was then tuned inside a high-vacuum cryostat by space charge doping as explained in Chapter 2. Above room temperature (350 K - 380 K), $\mathrm{Na^+}$ ion mobility inside the glass is activated. By applying a positive (or negative) gate voltage at the back of the glass substrate, the mobile $\mathrm{Na^+}$ ions drift towards (or away from) the sample/substrate interface, creating a positive (or negative) space charge and

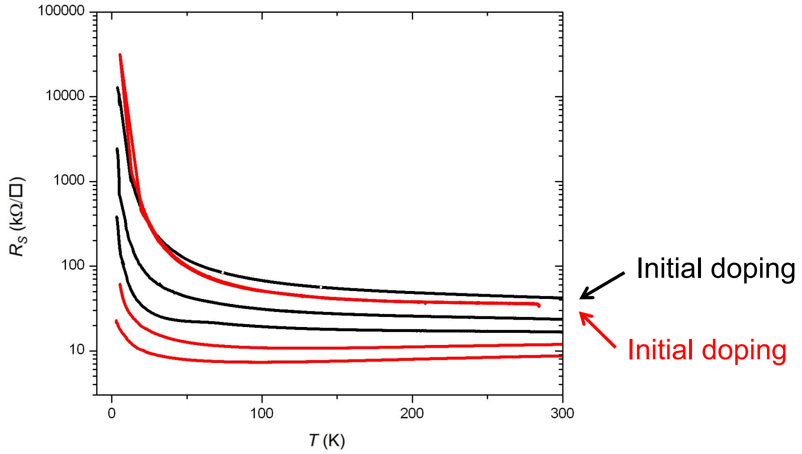

Figure 3.2: Sheet resistance curves of different doping level as a function of temperature. y-axis is en log scale. The black curves correspond to the sample annealed in the oven at 400 °C for 5 minutes after being fabricated with anodic bonding technique; the red curves refers to the sample annealed at 350 °C for just 1 minute.

corresponding electron (or hole) doping within the sample (Fig. 2.16). The doping time at the doping temperature for moving between two neighbouring doping levels is typically about 10-110 minutes. This space charge is frozen on cooling down to room temperature or below by loss of Na^+ ion mobility. Fig. 3.4 illustrates the behaviours of gate current I_G and sheet resistance R_S during one n-doping (electron-doping) process. As represented in Fig. 3.3, the SIT is attained by measuring the $R_S(T)$ curve at each fixed doping level.

Reversibility of space charge doping

The doping is tuned step by step as shown in Fig. 3.5. The temperature for doping varies from 350 K to 380 K. A positive (or negative) voltage, applied to the back gate of the device (Fig. 2.16), decreases (or increases) the doping level. The value of the voltage varies from 100 V to 280 V. The time varies from 10 minutes to 110 minutes. These doping procedures also present the reversibility of this electrostatic doping method.

Can the doping be due to oxygen diffusion rather than electrostatic charge?

In some electrostatic doping experiments with ionic liquids in oxide samples it has been shown that diffusion of oxygen at sample interfaces can contribute greatly to the dop-

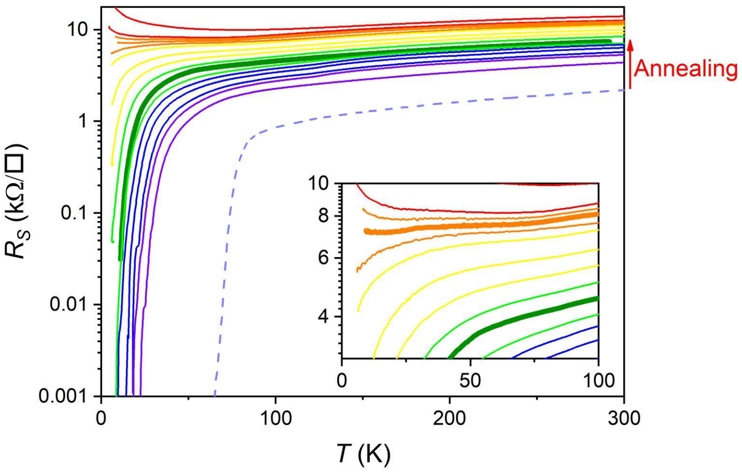

Figure 3.3: Temperature dependence of R_S curves induced by space charge doping with y-axis en log scale. The thick olive green $R_S(T)$ curve is the initial sheet resistance of the sample after annealing to reduce doping whereas the dashed violet curve is representative of the optimal doping level of 1 u.c. BSCCO after fabrication by anodic bonding. The inset shows a blow-up and the thick orange 'horizontal' curve approximately corresponding to the critical doping.

ing since in oxides doping depends on the oxygen content. High-Tc superconductors are oxides and in YBCO a material where such behaviour [122] is suspected, it is well known that two structural entities exist, planes and chains. The oxygen in the chains is weakly bound and this is the oxygen which is accumulated or depleted while doping with stoichiometric change of oxygen. It is explicitly stated in [122] that the observed oxygen diffusion related to strong electric fields is exclusively that of weakly bound chain oxygen atoms and not that of strongly bound oxygen atoms in the CuO2 planes. In BSCCO no chains exist. Eventual weakly bound oxygen can be accumulated in interstitial oxygen in BiO planes, causing distortions and superstructure in the unit cell. There is quantitative information about this. Diffusion constants for oxygen have been measured in BSCCO [123]. In the a-b plane (movement of interstitial oxygen) they are five orders of magnitude higher than in the c direction, the direction of the space charge doping electric field. Moreover, our sample has been pre-annealed so that oxygen content is extremely low and corresponds to an initial chemical doping around p=0.06 leaving no possibility of weakly bound oxygen which may be moved by an electric field.

In a liquid ion gated sample, the 2D sample is sandwiched between a substrate and the liquid ion layer. In our experiment, the sample is on the glass substrate which also serves as the gating material. Let us imagine that we induce oxygen diffusion in the sample. Even if weakly bound oxygen is available, it cannot diffuse in and out of a 1

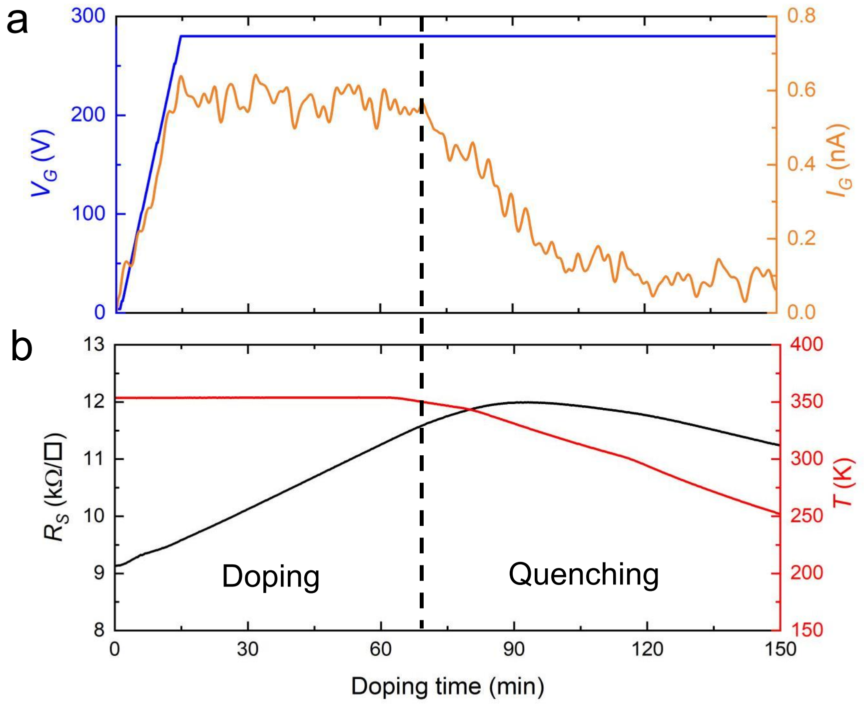

Figure 3.4: Dynamics of space charge doping. **a** A positive gate voltage is added to the back of the device from 0 to 280 V with steps of 4 V (blue curve, left axis). The behaviour of the gate current I_G (orange curve, right axis) during the n-doping process at 350 K (red curve in **b**) is plotted as a function of time. **b** Sheet resistivity (black line, left axis) vs doping time during space charge doping with positive gate voltage at $T = 350$ K and the following quenching in temperature. The temperature is presented with the red curve (right axis), the vertical black dash line marks the limit between the doping itself and the subsequent temperature quenching.

unit cell sample into the vacuum or the glass, reversibly. In a 3 unit cell sample sandwiched sample [122] oxygen diffusion can be imagined between different layers of the thicker sample or eventually at or with the sample/liquid ion interface. In our case this is not possible.

A further guaranty comes from the fact that we have successfully doped, with precisely the same space charge doping method and similar doping changes, samples such as graphene [111] and MoS_2 [100] which do not contain oxygen.

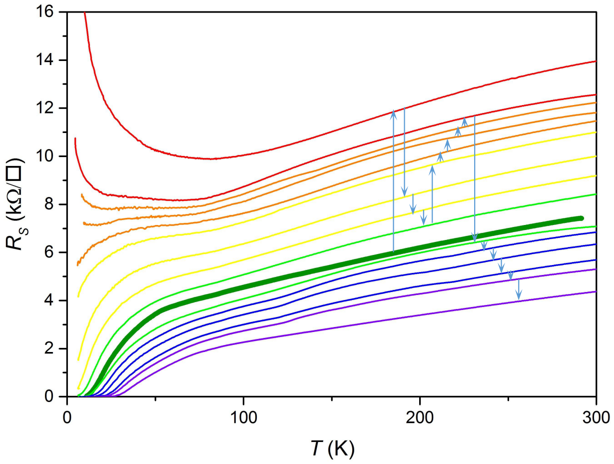

Figure 3.5: Temperature dependence of sheet resistance driven by space charge doping method on a linear scale. The thick olive $R_S(T)$ curve indicates the starting doping level after annealing in the oven. The left-to-right direction of the arrows shows the order of doping step by step, which shows the reversibility of this electrostatic doping method.

3.2.3 Hall measurement

The principle of Hall measurement has been explained in section **2.3.2**. The measurements were performed with a DC current of 1 to 10 μA. An external magnetic field of up to 2 T perpendicular to the sample plane was supplied by a resistive electromagnet at ~120 K. As described in section **2.3.2**, the Hall coefficient (or Hall resistance) $R_H = B/(en_S)$, where $e = 1.6{\times}10^{-19}\ C$ stands for the charge value of an electron, and n_S indicates the sheet charge carrier density. With the value of the slope of the fitted red curves in Fig. 3.6, the sheet carrier density of the sample can be calculated. Therefore for the initial doping level after annealing, which corresponds to the thick olive green $R_S(T)$ curve in Fig. 3.3, the carrier density of the sample $n_{S0} \simeq 8.9139{\times}10^{14}$ cm^{-2}. While the sheet carrier density of the highest n-doping level, represented by the highest red $R_S(T)$ curve in Fig. 3.3, $n_S(max) \simeq 0.7237{\times}10^{14}$ cm^{-2}. Therefore space charge doping provides an effective electrostatic doping method for a wide range of carrier density in 2D materials.

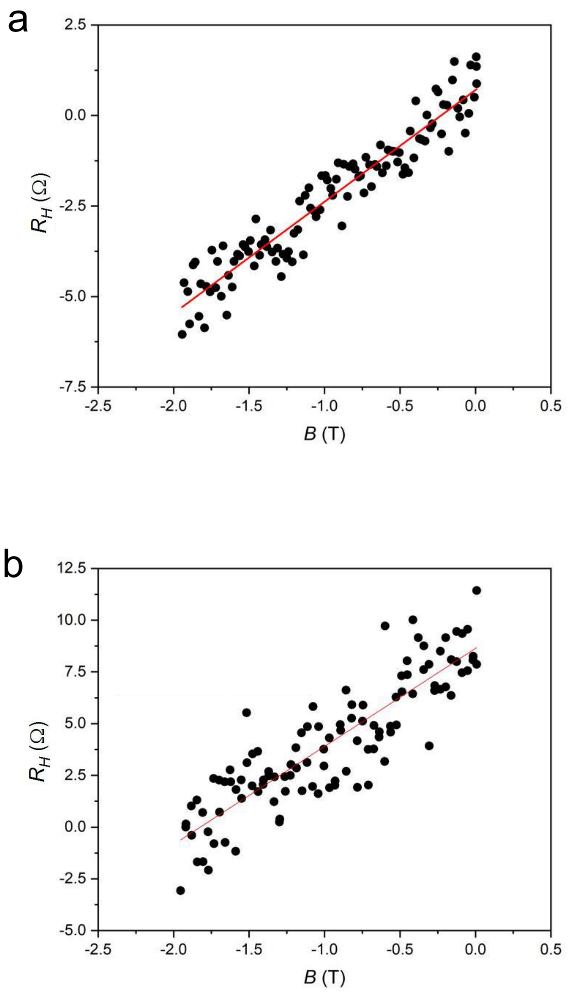

Figure 3.6: Hall coefficient as a function of magnetic field $R_H(B)$ for the initial doping **a**, which corresponds to the thick olive green $R_S(T)$ curve in Fig. 3.3, and for the highest n-doping **b**, which corresponds to the highest red $R_S(T)$ curve in Fig. 3.3. The thick red lines in both the two figures shows the linear fit with the program Origin.

3.3 Analysis and discussion

3.3.1 Determination of doping level

SIT is realized by tuning the sample's doping level with space charge doping technique. The immediate challenge, elusive even in bulk high T_c superconductors, is to determine the doping level. In a simple single band model the Hall coefficient R_H and the elementary charge q directly give the charge carrier concentration (or doping level) $p = 1/qR_H$. High T_c superconductors can certainly not be classified as such and indeed R_H is anomalously temperature dependent.

Drude model

One possible estimation is through the classical Drude model where conductivity σ is given by the product of the elementary charge q, the mobility μ and the carrier density n, that is $\sigma = q\mu n$. Based on this, attempts have been made to determine the carrier concentration using $p = S/R_S(T_f)$, where S is an empirically determined constant and $R_S(T_f)$ the sheet resistance at a fixed temperature well above T_c (we choose $R_S(200\text{K})$ in this thesis) [80, 82]. The constant S is determined by the maximum of the superconducting dome which is nominally set at 0.16 holes/Cu. In the inset of Fig. 3.7 **a** we show the relation between the Hall ($1/qR_H$) and Drude ($1/R_S(T_f)$) estimates of doping for device F (the sample studied in this thesis) and devices C, D and E used in the earlier studies in our lab [94]. Two deductions can be made. The relation is linear, implying simple proportionality. Device C, known to have high disorder and low mobility has a markedly different slope, showing the importance of mobility. If the empirical constant S is adjusted for each sample as in Fig. 3.7 **a**, we can hope to determine $p = S/R_S(T_f)$ as shown on the x-axis while maintaining the near linear relation with inverse Hall coefficient. The following procedure is taken to check the feasibility of this estimation. In Fig. 3.7 **b** the critical temperatures of these devices are shown as a function of the above estimation of doped charge. The generic dome shape is flattened and skewed, with superconductivity starting at a low doping of 0.028, and stretching above $p = 0.3$, well beyond the limits of the generic phase diagram. Though this result is coherent with a similar recent determination [53] we conclude that this estimate of doped charge is unsatisfactory.

Empirical formula

Another often used approach seeks to estimate doped holes (p) per Cu atom with an empirical $T_c(p)$ relation [45] for the region of the superconducting dome.

$$T_c(p)/T_c(p_{opt}) = 1 - Z(p - p_{opt})^2 \tag{3.1}$$

where $T_c(p_{opt})$ is the maximum critical temperature measured corresponding to the optimal doping level and Z is a scale factor empirically determined to be 82.6

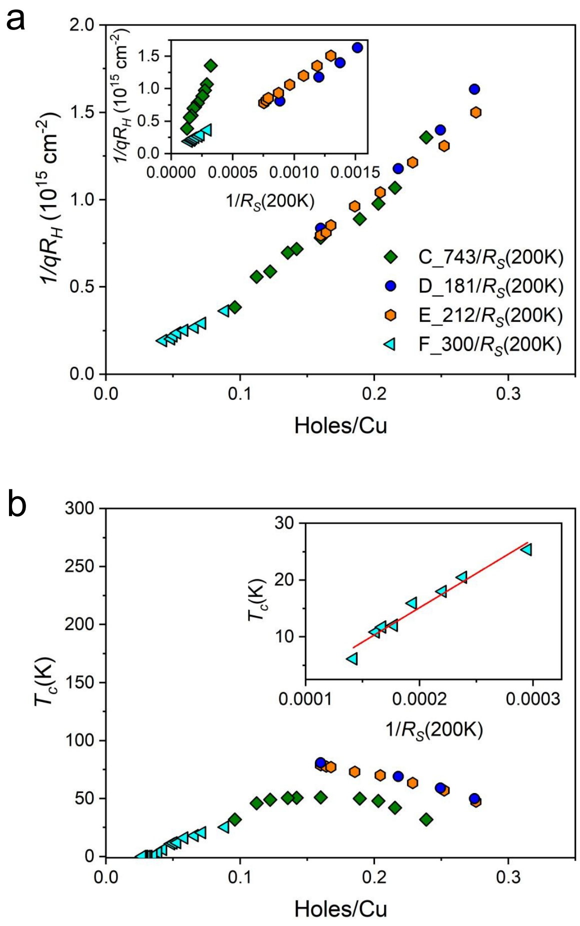

Figure 3.7: Hall coefficient and inverse sheet resistance for estimating doping. **a** Dependence of $1/qR_H$ on $p = S/R_S(T_f)$ for device F of this work and devices C,D and E of our earlier works. Inset: Dependence of $1/qR_H$ on $1/R_S(200\ K)$ showing linear behavior. **b** Superconducting dome as a function of T_c and of doping p as calculated above for devices C, D, E and F. Inset: Critical temperature T_c as a function of $1/R_S(200\ K)$ showing a linear dependence in the neighborhood of zero T_c.

[124, 121, 125]. In this approach, in accord with the generic phase diagram, superconductivity exists in the region $p \sim 0.05$ to $p \sim 0.27$ holes/Cu. The dome shape implied by this relation is experimentally verified (notwithstanding local deviations for example in YBCO around p = 0.12 doping), in particular for 1 u.c. BSCCO [94]. The problem in our case is that doping has to be determined for non-superconducting as well as superconducting regions. To overcome this hurdle we seek inspiration from the simpler approaches discussed above. Firstly we remark (inset Fig. 3.7**b**) that when the T_c in the superconducting region is plotted against the inverse sheet resistance at 200 K, a simple linear relationship is found. Extrapolating this relation to the nearby non superconducting region, we replace T_c by $S/R_S(200\ K)$ in equation 3.1 where S is the value of the slope of this linear dependence. We thus have a coherent and continuous estimation of p across the SIT which is compatible with the generic high T_c phase diagram. This method should be applicable to other high T_c materials. In Fig. 3.8 we show the part of the phase diagram around the beginning of the superconducting dome, relevant to device F. Superconductivity develops according to this estimation at a critical doping of $p \sim 0.057$. In the inset of Fig. 3.8 we show the superconducting phase diagrams for devices C,D,E and F, which are compatible with the generic phase diagram by construction and exhibit a smooth variation with an optimum doping of 0.16 holes [94, 110]. Remarkably, in a recent study [126] an estimation of doped holes in bulk BSCCO using Fermi surface volume measured by photoemission measurements finds that the dome in BSCCO is smooth, with a range corresponding to our observations and in agreement with the generic high T_c shape.

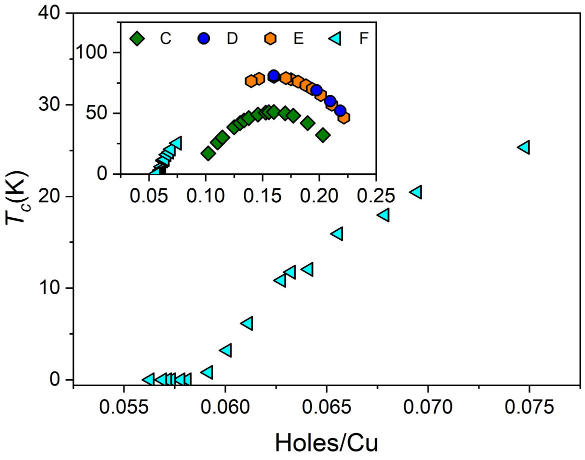

Figure 3.8: Superconducting dome (phase diagram) as a function of critical temperature and doping. Inset: Superconducting phase diagram for four devices C,D,E and F.

3.3.2 Finite-size scaling of QPT

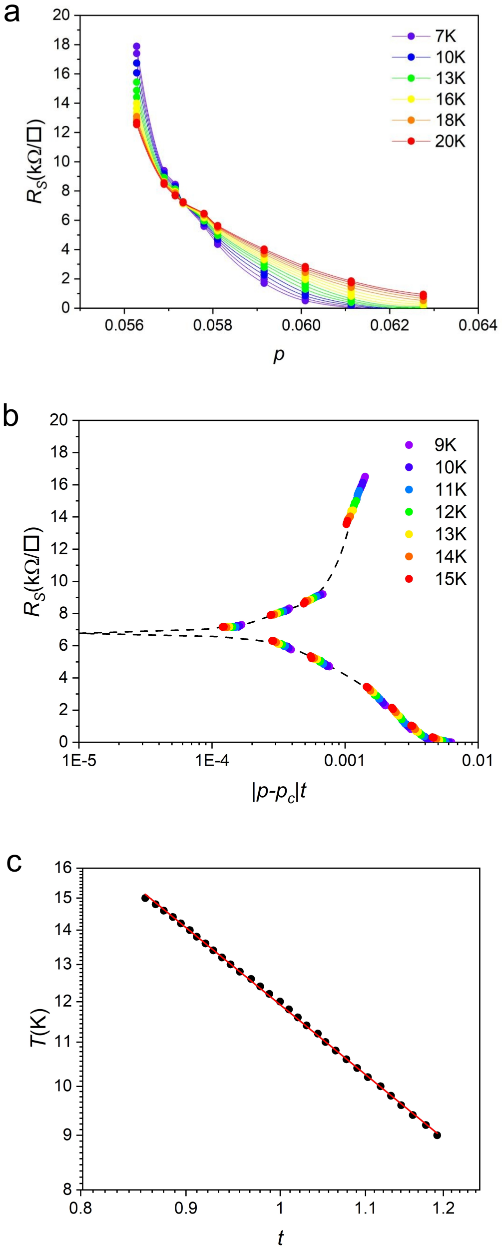

Figure 3.9: Finite-size scaling of QPT. **a** Doping dependence of isothermal sheet resistance from 7 K to 20 K. The dots are extracted from $R_S(T)$ data and the lines are splined guides for the eye. **b** Universal finite-size scaling function at the SIT with $t = T^{-1/\nu z}$. **c** The linear relation between T and t and between 9 K and 15 K plotted on a log-log scale. From the slope we obtain the critical exponent product $\nu z = 1.57 \pm 0.10$.

A superconductor-insulator transition (SIT) in two dimensions is a continuous quantum phase transition (QPT) at absolute zero temperature driven by external parameters like disorder, magnetic field or carrier concentration. In this thesis, the carrier concentration is tuned by space charge doping technique to realize this QPT. Based on the estimation method discussed in last section **1.3.1**, we can set about investigating the existence of possible scaling relations corresponding to a quantum phase transition in our 1 u.c. BSCCO device at the SIT. This implies that all sheet resistance curves of Fig. 3.3 should collapse onto a single finite-size scaling function

$$R_S = R_c f(|x - x_c| T^{-\frac{1}{\nu z}}) \tag{3.2}$$

where R_c is the critical resistance at the limit $x \rightarrow x_c$ and $T \rightarrow 0$. f is the universal scaling function and x is the tuning parameter, in our case the doping level p. The correlation length exponent ν and the dynamic critical exponent z, together with the critical resistance R_c encode the nature of this transition [80, 82].

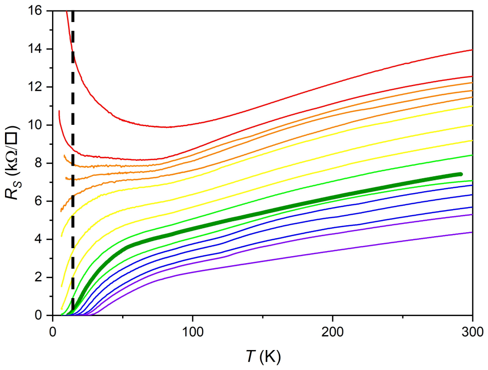

Figure 3.10: Illustration of extraction of isothermal sheet resistance. The intersection points between the thick black dotted line and all the sheet resistance curves represent all the sheet resistance values at the same temperature.

Fig. 3.9 shows the results of finite-size scaling analysis of the SIT in device F. The first indication of critical behaviour can be found by plotting the isothermal sheet resistance of the data in Fig. 3.3, not as a function of temperature, but as a function of the doping p. This is done in Fig. 3.9**a**. Each temperature dependence of the sheet resistance curve in Fig. 3.3 is recorded at a fixed doping level, because the doping level, tuned by space charge doping at high temperature, can be fixed by removing the mobility of the Na^+ ions when cooling to room temperature or below. So we can extract the value of the sheet resistance at a fixed temperature from each R_S curve (or each doping level), and this procedure can be explained in Fig. 3.10. Then these isothermal sheet resistance values can be plotted as a function of doping level, which constitutes one $R_S(p)$ curve in Fig. 3.9**a**. Fig. 3.9**a** shows the isothermal $R_S(p)$ curves between 9 K and 20 K (a total of 30 different temperatures were used), all curves intersect at a single point which corresponds to the critical doping $p_c \sim 0.057$ where superconductivity sets in. The corresponding critical sheet resistance is ~ 6.85 k$\Omega.\Box^{-1}$.

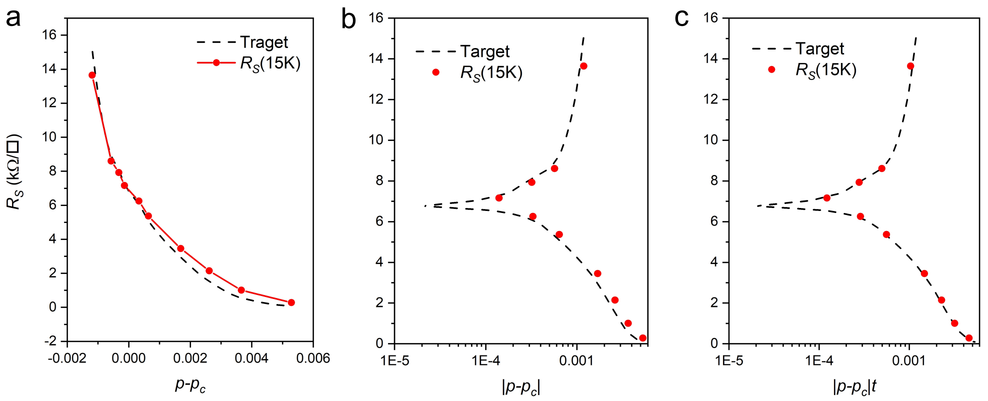

Figure 3.11: Illustration of renormalization process for the extraction of the critical exponents. **a** Isothermal sheet resistance as a function of $p - p_c$, $R_S(p - p_c)$. The thick dotted curve is the target curve f, on which all the isothermal sheet resistance should collapse. Here, $R_S(12K)$ is chosen as the target. Red curve is the isothermal sheet resistance curve at 12 K. **b** The same data as **a**, but as a function of $|p - p_c|$ with x-axis en log scale. **c** The same data as **b** with the abscissa contracted by the coefficient t depending on the temperature. By definition, t(12K)=1, and t(15K) is optimized to maximum the overlap of the two curves.

In Fig. 3.9**b** we investigate the existence of a single finite-size scaling function f for data between 9 K and 15 K by using as the abscissa $|p - p_c|t$. For each isothermal curve in Fig. 3.9**a** (a total of 30 different temperatures), a scaling factor t is optimized such that it collapses onto f, chosen as the 12 K sheet resistance variation, as discussed below and shown by the dashed line. This renormalization process is explained in Fig. 3.11 with R_S(15K) as an example. If the scaling is valid, the corresponding experimental points of Fig. 3.9**a** should collapse onto the scaling function, as indeed observed in Fig. 3.9**b**.

The power law relation between T and t between 9 K to 15 K is shown in Fig. 3.9**c**. A perfect linear relationship is seen in a double logarithmic plot since all scaling factors t should be of the form $t = T^{-1/\nu z}$ based on the equation 3.2. From the slope we obtain the critical exponent product $\nu z = 1.57 \pm 0.10$ similar to the $\nu z = 1.5$ found in LSCO [80]. However in YBCO ($\nu z = 2.2$ [82]) and BSCCO ($\nu z = 1.53$, 2.45 and 2.35 for three different devices [53]) contrasting results have been found.

Finite-size scaling from 7 K to 20 K

In Fig. 3.12 we show the same scaling analysis between 7 K and 20 K. All sheet resistance collapse again onto a single function, which shows that critical sheet resistance R_c = 6.85 ± 0.1 kΩ.$\square^{-1}$. Then we also plot the relation between T and t between 7 K and 20 K on a double logarithmic scale, as shown in Fig. 3.12**b**. We remark that deviations from linearity are found at the two extremes. The possible reason can be that for higher temperatures ($>$ 15 K) thermal fluctuations may overshadow the QPT while at lower temperatures ($<$ 9 K) defect related weak localisation phenomena may alter it, justifying our choice of the 12 K curve for the scaling function f.

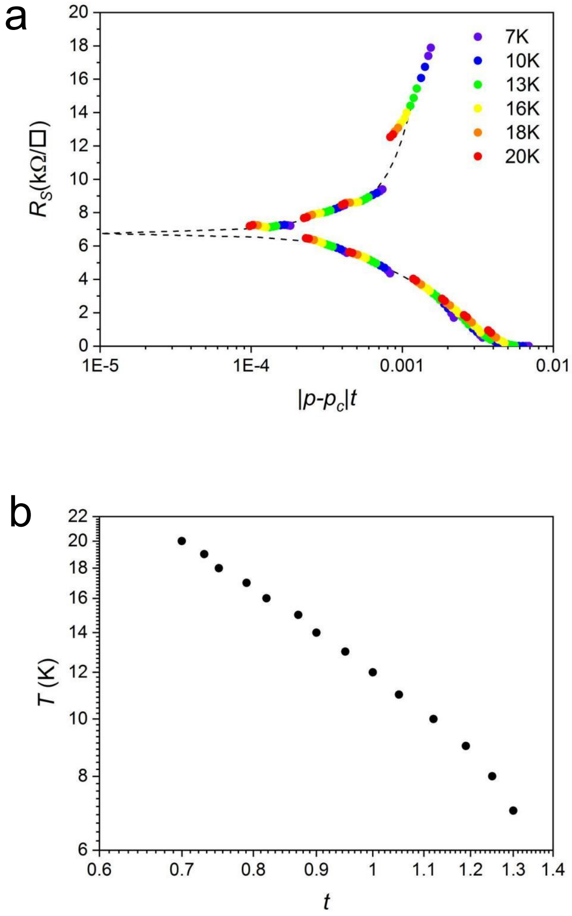

Figure 3.12: Scaling analysis between 7 K and 20 K. **a** Scaling of the same sheet resistance data as in Fig. 3.9**a** as a function of $|p - p_c|t$ with $t = T^{-1/vz}$. **b** The linear relation between T and t from 7 K to 20 K on a double logarithmic scale. Deviations from linearity are found at extremes. The possible reason can be thermal fluctuations at high temperature and defect related to weak localization at low temperature.

Validity of scaling at two extreme temperatures

The zero temperature quantum critical point should imply that data at the lowest temperatures is the most indicative of the physics in question. However just as quantum critical aspects may be blurred on the high temperature side by thermal fluctuations, the ground state may also be overshadowed on the low temperature side by effects such as weak localisation which can become dominant before this ground state can be reached through the critical point and across the quantum phase transition. This or other analogous effects will always be present in a real sample. So we argue for a domain of temperatures not too low and not too high where the effects of the quantum phase transition are the most evident. Moreover, it is the scaling process which allows us to determine this domain as shown by the two ranges we have used (7K-20K and 9K-15K). In particular for the data in the range 7K to 9K, it can be clearly seen (Fig. 3.12**b**), that νz, which is given by the local slope, is much higher than 1.5. This directly results from the R_S of the insulating phases rising higher than the 'expected value' for temperatures below 9K and indicating that it is indeed a localisation like phenomenon which causes this discrepancy. In high Tc samples such behaviour is clearly visible in earlier work [82].

We cannot exclude the possibility of a flattening of the superconducting dip at lower temperatures and a quantum superconductor-metal transition invoked by Kapitulnik et al. [127]. But even this transition and interpretation is only valid untill a certain low temperature limit. There is no guaranty that R_S stays finite at still lower and unattained temperatures and in fact for 2D samples it should become infinite as temperature is continuously lowered. However, as successfully argued in reference [117] this could mean double critical points with no hierarchy of one critical point over the other but a change in criticality according to the coherence length picked out by the temperature and the control parameter in an inhomogeneous sample.

In high Tc samples with pairing in the underdoped region expected to persist to high temperatures and a high Tc at optimal doping, we can expect quantum critical effects to persist at temperatures higher than in metals where a superconducting transition is achieved at a few Kelvin or a few tenths of a Kelvin. Indeed in YBCO [82] the low temperature data is not used for scaling either.

3.4 Conclusion

The superconductor-insulator transition has been uniquely characterized as having a non-zero and finite resistance phase corresponding to a 'horizontal', temperature independent resistance [76] which is also the critical resistance. What is the nature of the superconductor-insulator transition found here?

The superconducting state is characterized by a complex order parameter. A continuous quantum phase transition is characterized by the continuous change of this order parameter across the transition (giving rise to power laws and scaling) and critical fluctuations of the amplitude or the phase of the order parameter at the transition. Amplitude fluctuations imply the breaking down of pairing above the critical temperature and the transformation of Cooper pair bosons to fermions as in superconductors described by the Bardeen-Cooper-Schieffer (BCS) scenario. The fermion state may be a metal or even an insulator if in the latter eventuality the fermions are localized by disorder or interactions. Phase fluctuations in superconductors are typically described in the Berezinskii-Kosterlitz-Thouless scenario by the duality between Cooper pairs and vortices which are both bosons. In the superconducting state, vortices (associated with phase 'slips' and dissipation), are bound in pairs and localized while Cooper pairs are mobile. The opposite situation prevails above the critical temperature and the system is insulating. If this duality is perfect, a simple argument [7] establishes the critical resistance threshold between the superconducting and insulating states at the quantum resistance with pair charge: $R_Q = h/(2e)^2 = 6.45$ k$\Omega.\square^{-1}$. However deviations from perfect duality generated by the nature of the interaction or factors like disorder are to be expected [76]. Thus the measurement of the critical resistance and the finite scaling exponents of the continuous QPT can inform us about the all-important nature of the superconducting state. Simple models exist for some cases and are used for defining the universality class, for example $\nu z = 4/3$ in the classical percolation model, 7/3 in the quantum percolation model [128, 84] and 2/3 in the 3D XY model [129].

Our result of $R_c = 6.85$ kΩ ($\pm$ 0.10 kΩ) which is reasonably close to R_Q found in LSCO [80] favors the picture of a phase fluctuation driven transition and a strong coupling pairing interaction for high T_c superconductivity at the underdoped limit as opposed to the weak coupling scenario in BCS superconductors. We find $\nu z = 1.57 \pm 0.10$ for the finite scaling exponent product describing the measured transition. This again compares favorably with the value of 1.5 [80] in LSCO and 1.53 in one BSCCO device [53], implying the same universality class for these compounds. A quantum critical point should imply that data at the lowest temperatures is the most indicative of the physics in question, so scaling of data at higher temperatures should be treated with caution. Just as quantum critical aspects may be washed out by thermal fluctuations, the ground state may also be overshadowed at lower temperatures by effects such as weak localisation. Other effects such as a low temperature non-zero resistance metallic state instead of a superconducting one [127] or a double critical point [117] may also appear. However the clear separation in our data between the insulating and the superconducting regimes at the critical conductivity corresponding to $R_Q = h/(2e)^2$ provides support for the existence of the quantum phase transition and critical point [130].

We retain several other positives from this work. The use of a 1 u.c. sample ensures strict two dimensionality and makes a direct link with our earlier work on similar samples [94, 110], notably with respect to the phase diagram and rigorous estimation of doping. The space charge doping method avoids problems which may arise in liquid dielectrics [119, 112, 23], ensures all measurements on a single, low disorder, good quality sample and removes the sample dependent uncertainty that comes from chemical doping.

Chapter 4

2D superconductivity: Effects of Inhomogeneity and Fluctuations with Simulations and Experiments

In this chapter, I will first give a brief introduction on the superconducting transition and the underlying information extracted from its sheet resistance curves as well as the corresponding derivative curves. Then Berezinskii-Kosterlitz-Thouless (BKT) transition and the phenomena as well as the analytical method related will be described in section **4.1**. In section **4.2**, simulation process is explained. And finally, the analysis of transport measurements data will be given in section **4.3**. (*Johan BISCARAS did the simulations for the contents of this chapter.*)

4.1 Introduction

Transport measurements are macroscopic but the superconducting transition is inevitably dependent on mesoscopic and nanoscopic detail. Can simulations of the superconducting transition, coupled with transport measurements, bring understanding about phenomena happening at these scales? To answer this question, we base ourselves on measurements of the superconducting transition as a function of electrostatic doping in 1 unit cell thick samples and analysis of the width and shape of this transition. The 3 nm thickness allows for uniform electrostatic doping which is a convenient and defect-free means of bringing about continuous change in doping in the same sample. The use of an ultra-thin sample also facilitates analysis on two fronts. Firstly, in two dimensions fluctuation phenomena related to the superconducting transition are exacerbated, making the analysis of changes in widths easier. Secondly aspects related to percolation and clustering can be easily simulated and compared with analytical models.

4.1.1 The superconducting transition

A superconducting transition in ideal bulk material is an abrupt transition with a vanishing width. As shown in Fig. 4.1, the typical measured superconducting transition in our samples as seen in the temperature dependence of sheet resistance $R_(T)$, has a width clearly seen from the dR_S/dT derivative curve. The main mesoscopic or local contributions to this width are fluctuations and inhomogeneity. Sample inhomogeneity can originate in defects or heterogeneous doping resulting in a macroscopic doping distribution and local variation of critical temperature. In the extreme case, the sample may also include non-superconducting regions. To discuss the effects of fluctuations and inhomogeneity, we identify two regions from the dR_S/dT curve, the high temperature (HT) and low temperature (LT) sides. These two sides are separated by the maximum of the derivative curve as presented in Fig. 4.1. It is our working hypothesis that the LT side is influenced principally by inhomogeneity and the HT side principally by fluctuations. This chapter will examine this hypothesis by comparing extensive 2D simulations of the superconducting transition in the presence of these local perturbations which will be analysed in the background of measured transition.

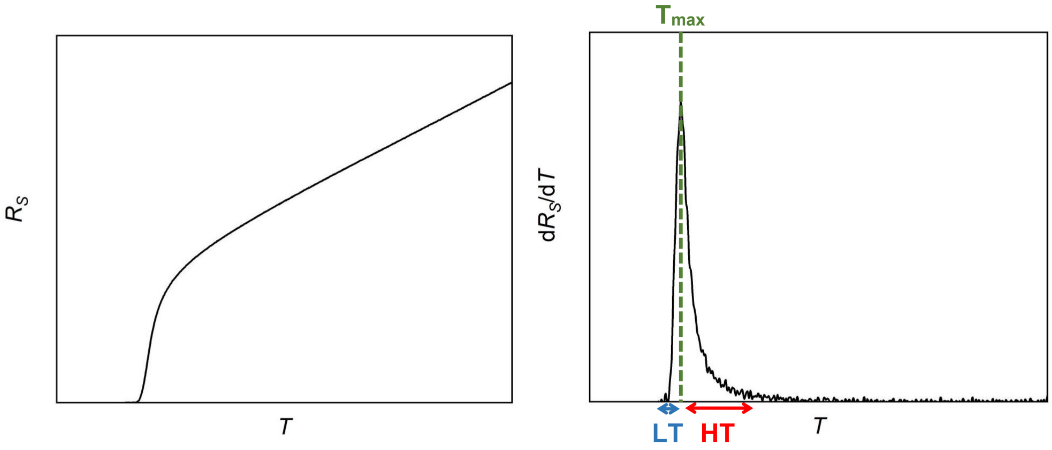

Figure 4.1: Schematic view of temperature dependence of sheet resistance curve $R_S(T)$ (left) and its related derivative curve dR_S/dT (right). The identified higher temperature (HT, red) and lower temperature (LT, blue) are indicated on the right figure, separated by the green dotted line indicating the maximum of the derivative curve.

The effect of fluctuations is always present in experiments. However this effect can be included or excluded from the simulation based on established models. Thus by comparing the two the the effect of fluctuations can be quantified.

Inhomogeneity englobes different aspects. Defect induced inhomogeneity can deteriorate critical temperature and mobility. Heterogeneous doping which could be an intrinsic feature in these materials implies a probability distribution of critical temperatures which we have examined in detail in simulations later in this chapter. In experiment an example of inhomogeneity from the reference [131] is shown in Fig. 4.2. We can observe that in slightly underdoped BSCCO-2212, superconductivity is clearly granular in nature, with homogeneous superconducting domains of ∼3 nm. The influence of such non-superconducting domains on the superconducting transition can of course be examined in simulations and can be also studied experimentally using an external magnetic field which generates vortices. These can then be switched on or off with the magnetic field. We show later the influence of all these parameters.

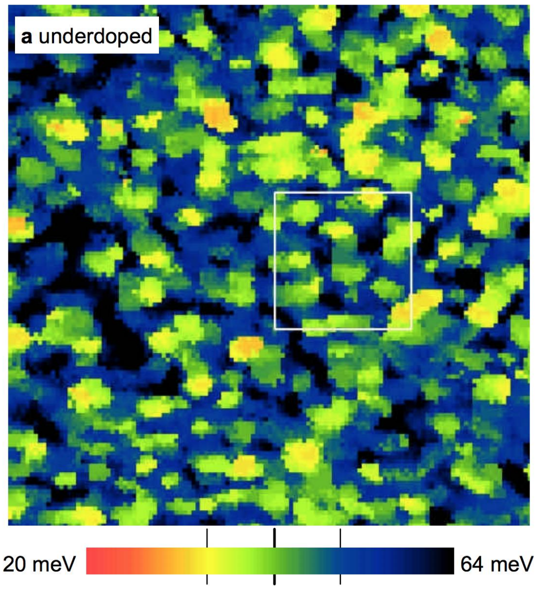

Figure 4.2: STM gapmap of a slightly underdoped BSCCO-2212 sample (T_c = 79 K), showing an area of 56 × 56 nm and colour scale spanning the range 20 ± 64 meV. [131]

4.1.2 Berezinskii-Kosterlitz-Thouless transition

The superconducting transition in two dimensions is expected to be a Berezinskii-Kosterlitz-Thouless (BKT) transition [132, 133, 134], which is related to the non-trivial topological defects (vortices) rather than continuous symmetry breaking. Such a transition has been experimentally observed in superfluid Helium films [135], layered magnets [136], two dimensional conventional superconductors [137, 138, 139], as well as high-T_c superconductors [140, 141]. The BKT transition is universally described by the 2D XY-model as discussed in these references where the system is considered to be a simple square lattice with spacing **a**. The Hamiltonian of the system is given as:

$$H_{XY} = -J\sum_{i,j} cos(\theta_i - \theta_j) \tag{4.1}$$

where θ_i is the angle relative to some fixed axis, $i(j)$ represent the sites of the square lattice in two dimensions, and J is the spin-spin coupling constant [133, 142]. The U(1) symmetry of the phase field $\theta(\mathbf{r})$ is admitted in this XY-model, and it cannot be broken at finite temperature [140]. However, at low temperature, the system can be described as "stiff" with respect to the fluctuations of the variable θ [142]. The relevant transition is driven by vortex-like topological excitations [141, 143]. If we consider a single vortex, the Helmholtz free energy is given by

$$E = F - TS = (\pi J - 2T) ln \frac{L}{a} \tag{4.2}$$

where E is the energy and S is the entropy of a single vortex excitation [133, 142]. In 2D, both of them are logarithmically dependent on the size L of the system. A critical temperature, which is called the BKT temperature, is extracted from this formula:

$$T_{BKT} \simeq \frac{\pi J}{2} \tag{4.3}$$

This is the temperature below which the vortices are bound together in vortex-antivortex pairs. When $T > T_{BKT}$, free vortices proliferate and destroy the quasi-long-range order [142, 144].

For a 2D superconductor, the energy scale corresponding to the coupling J in the XY-model is defined as the superfluid stiffness, which is associated with the areal density ${n_s}^{2d}$ of the the superfluid electrons [141, 142, 145]:

$$J_s = \frac{\hbar^2 {n_s}^{2d}}{4m} = \frac{\hbar^2 c^2 d}{16\pi e^2 \lambda^2} \tag{4.4}$$

where d is the thickness of the 2D superconductor, m is the effective mass of the carriers, and λ is the magnetic penetration depth. In the case of conventional 3D superconductors, $J_s(T)$ vanishes continuously to zero at the superconducting transition temperature [145]. In 2D the BKT superconducting transition is governed by vortex-antivortex proliferation, so that one would expect that the superfluid density discontinuously jumps to zero at T_{BKT} [142, 145, 146].

4.1.3 Fluctuation phenomena and 2D HTS

Fluctuations are more easily observed in high-T_c superconductors than in conventional superconductors due to the small coherence length of a few nm, or three lattice constants in the plane, and even less in the perpendicular direction [147]. These fluctuations, which have been proved to have a strong 2D character in several cuprates [141, 148, 149, 150], are thought to be of Gaussian (amplitude and phase) nature [141, 147].

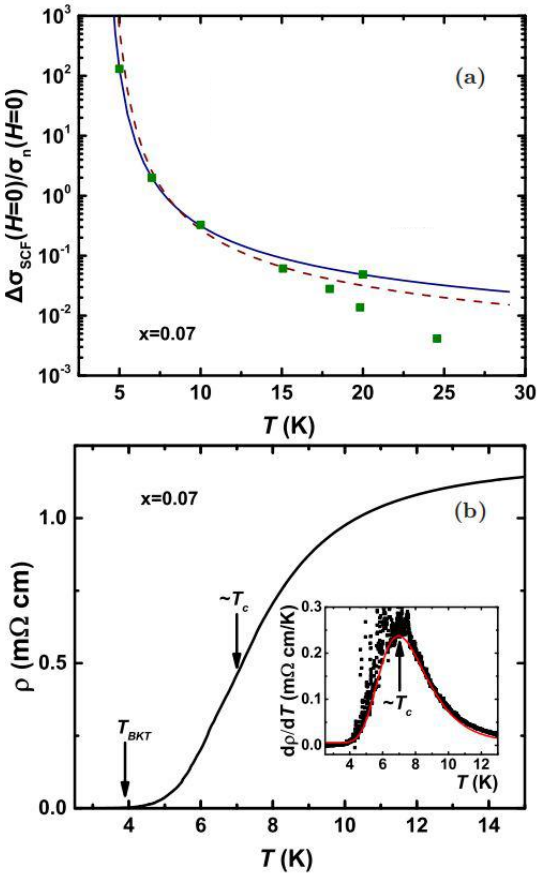

Figure 4.3: Paraconductivity of LSCO film with doping level $x = 0.07$. **a** The green square symbols are temperature dependence of $\frac{\Delta\sigma}{\sigma_n}$ without magnetic field ($H = 0$), which are extracted from experimental data (details are explained in [141]). The solid curve, as well as the dotted curve, is a fit to formula 4.5 with reasonable parameters T_{BKT}, A and b. **b** $\rho(t)$ at $H = 0$. T_{BKT}=3.9±0.1 K, is taken as the temperature of zero resistance on the curve. GL temperature T_C is determined to be the temperature where $d\rho/dT$ is maximum (inset).

In 2D, the theory to describe the correspondence between the paraconductivity (or resistivity) in 2D superconductors and the fluctuation correlation length has been established [140, 141]. When approaching the superconducting transition from $T > T_{BKT}$, the formula which is usually used to describe the paraconductivity due to vortices [141] is given by

$$\frac{\Delta\sigma}{\sigma_n} = \left(\frac{\xi(T)}{\xi_0}\right)^2 \tag{4.5}$$

where $\Delta\sigma = \frac{1}{\rho(T)} - \frac{1}{\rho_n(T)}$ is the temperature dependence of the contribution of superconducting fluctuations to paraconductivity (ρ and ρ_n are respectively the measured and normal-state resistivity), and $\xi(T)$ is the temperature dependence of superconducting correlation length. Then if we follow the Aslamazov-Larkin [**?** **?**] (AL) contribution to GL fluctuations, which is widely adopted for describing fluctuating Cooper pairs above the mean-field temperature T_C (also known as the Ginzburg Landau Temperature T_{GL}), the coherence length will diverge following a power-law $\xi^2 \sim (T - T_C)^{-1}$ [140, 141]. In addition, in the scenario of the BKT transition, the correlation length can be defined in terms of the inverse of the vortex density (n_F), thus we can have the relation $\xi^2 \equiv \frac{1}{2\pi n_F}$. According to Halperin and Nelson's observation, the BKT transition is supposed to occur only in a range of temperature $t \ll t_C$ [151], where t and t_C are defined as below

$$t = \frac{T - T_{BKT}}{T_{BKT}} \ , \quad t_C = \frac{T_C - T_{BKT}}{T_{BKT}}. \tag{4.6}$$

Halperin and Nelson also propose an interpolating formula to describe the transition between the higher temperature GL and the lower temperature BKT regimes:

$$\frac{\Delta\sigma}{\sigma_n} = \left(\frac{2}{A} sinh \frac{b}{\sqrt{t}}\right)^2 \ , \quad T \gtrsim T_{BKT} \tag{4.7}$$

where A and b are constants of order 1 [140, 141, 151].

Fig. 4.3 from [141] shows the above analysis applied to in-plane transport measurements in thick LSCO films ($d \approx 10^3$ Å), where it is argued that low dimensionality intervenes because of the 2D nature even in bulk. The authors conclude that the BKT regime exists at $T_{BKT} < T < T_C$ and for $T > T_C$, a crossover to the GL regime occurs.

4.1.4 Effects inhomogeneity and 2D HTS

Mesoscopic inhomogeneity has a crucial effect on the BKT transition in two dimensions by considerably broadening the transition width [140, 143]. Spatial variations can occur not only in the local density of states but also in the local superconducting energy gap [152]. Such inhomogeneity on the nanoscopic scale has been revealed both in the conventional superconductors [153] and in cuprates [154] by scanning tunneling spectroscopy (STS). However, in practice, the direct observation of the BKT transition is rather challenging. Thus indirect analysis on the data of transport measurements, such as temperature dependence of sheet resistance curves $R(T)$ and I-V curves, has been intensively studied [140, 153, 154, 155, 156, 143]. Theoretical work [157, 140, 143] has also been used for comparison with experimental results.

To study the effect of inhomogeneity, Benfatto and co-workers [140] proposed an interpolation formula, based on the original interpolation formula introduced by Halperin and Nelson [151] for paraconductivity, to describe the superconducting transition between the Ginzburg and Landau (GL) fluctuations at higher temperature and the BKT fluctuations at lower temperature.

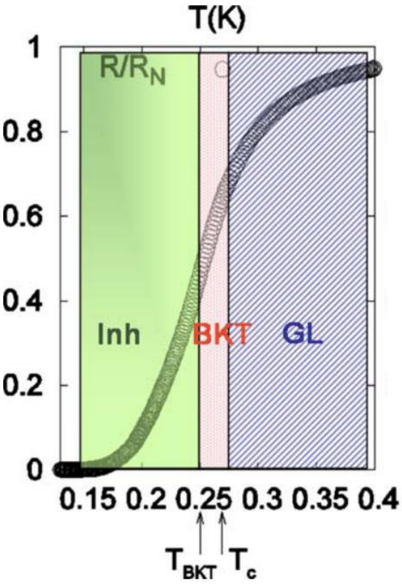

Figure 4.4: Analysing different rgimes in the transition, from [140]. Above T_{BKT}, the regime is governed by GL fluctuations. BKT fluctuations are restricted to a narrow range of temperature. A considerable tail results from inhomogeneity of the system.

$$\frac{R}{R_N} = \frac{1}{1+(\Delta\sigma/\sigma_n)} = \frac{1}{1+(\xi/\xi_0)^2} \tag{4.8}$$

where R_N is the resistance of the normal state, and $\xi(T)$ is the temperature dependence of the superconducting correlation length. Here

$$\frac{\xi}{\xi_0} = e^{\frac{\mu(T)}{2k_BT}} \left(\frac{L}{\xi}\right)^{\frac{\pi J(T)}{2T}} , \quad T \lesssim T_{BKT} \tag{4.9}$$

$$\frac{\xi}{\xi_0} = \frac{2}{A} sinh\left(b\sqrt{\frac{T_{BKT}}{T-T_{BKT}}}\right), \quad T \gtrsim T_{BKT} \tag{4.10}$$

where the parameter A is a constant of order 1, and $b = 2.1\sqrt{(T_{GL}-T_{BKY})/T_{BKT}}$, which is deduced from renormalization-group theory calculation of $\xi(T)$ near T_{BKT} [140]. This interpolation formula gives an idea of the relative values of T_{GL} (or T_C) and T_{BKT}, and can be used to study the impact of inhomogeneity on the tail of the resistance transition [140]. Fig. 4.4 represents this approach introduced by reference [140]. One possible way to describe the spatial inhomogeneity of the system is to use a Gaussian profile for the probablility distribution of critical temperatures[140, 141].

$$P(J) = \frac{1}{\sqrt{2\pi}\delta} e^{-\frac{(J-J_0)^2}{2\delta^2}} \tag{4.11}$$

where J_0 is a constant value determined for the homogeneous case. In the homogeneous condition, the width of this Gaussian contribution is zero, and only the value J_0 is permitted. J_0 refers to the density of superfluid electrons at zero temperature [140, 141] and can be calculated using BCS theory, where the superconducting gap is evaluated to be $\Delta(0) = 1.76 k_B T_c$.

$$J_0 = \frac{\hbar^2 {n_S}^{2D}}{4m} \approx \frac{\hbar}{e^2 R_S} \frac{\pi \Delta(0)}{4} \tag{4.12}$$

where ${n_S}^{2D}$ is the superfluid density in two dimensions, and m is the effective mass of the carriers. In this work we choose a gamma distribution for the probability distribution of local T_c rather than a Gaussian distribution as it is more general, especially in terms of asymmetry. The details are given in the next section.

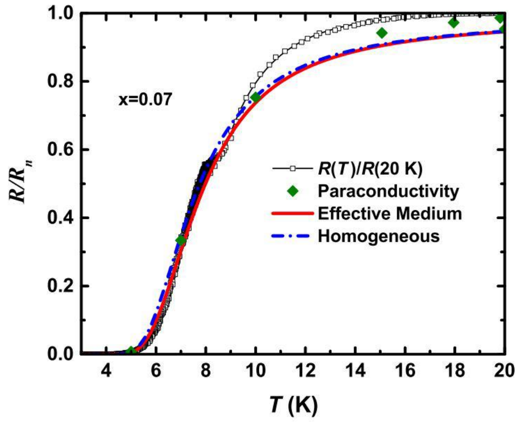

Figure 4.5: Comparison between the resistivity ($R(T)/R_n(T = 20\ K)$ black) measured in LSCO films (x=0.07) and the resistivity theoretically deduced from formula 4.8 both in the inhomogeneous (red) and homogeneous (blue) case. The theoretical data $R(t)$ is determined as the solution of a random-resistor-network problem in a so-called effective-medium approximation. [141]

Fig. 4.5 from [141] shows this approach including both inhomogeneity and fluctuations for analysing in-plane transport measurements in LSCO with $x = 0.07$. Though a quantitative fit over the whole temperature range is not possible, it can be seen that the contributions of inhomogeneity and fluctuations can be approached by such an analysis.

In conclusion, in 2D fluctuation phenomena and the effect of inhomogeneity are exacerbated and significantly modify the shape of the superconducting transition. In the following sections, we use a two dimensional grid of resistors for simulation and one unit cell thick BSCCO devices for the measurement of the width and shape of this transition. Simulations using the explicit calculation of the sheet resistance of a 2D array of resistors with resistance adjusted to different inhomogeneity landscapes is used along with Effective Medium Theory for making deductions below the macroscopic scale. This provides a means for using the superconducting transition as a tool for understanding mechanisms related to fluctuations and inhomogeneity which are fundamental for many superconductors.

4.2 Simulations

In this section I will describe the model and results of simulations of 2D inhomogeneous superconductivity, and then how the shape of the transition (width, tail) is affected by different parameters. (*Simulations done by Johan BISCARAS.*)

4.2.1 Resistor network model

The resistor network

We model a 2D (super)conductor by a square grid of resistors. It is convenient to represent the network by a visual picture as shown in Fig. 4.6. On the picture each coloured pixel represent simultaneously a node of the resistor network and the two resistors on the right and below connected to it. For simplicity the two resistors within each pixels have the same resistance value (i.e. each pixel is isotropic).

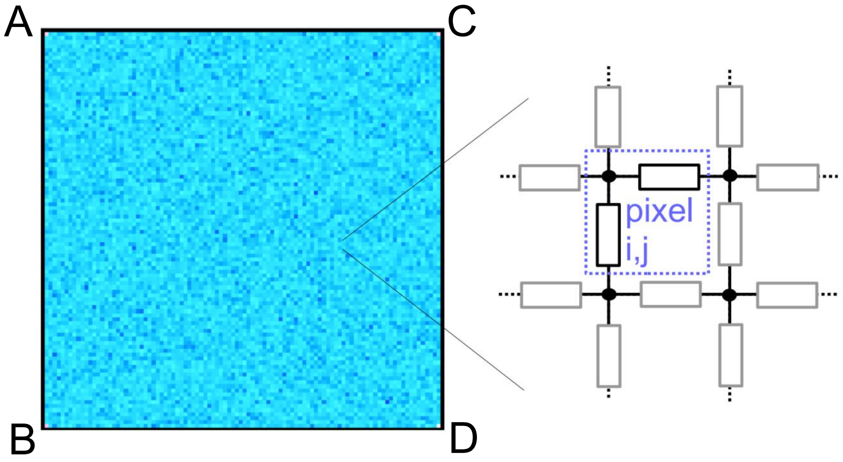

Figure 4.6: A resistance network represented by a bitmap image.

Without magnetic field, we can write Kirchhoff's law of current conservation at each node i, j:

$$\frac{V_{i+1,j} - V_{i,j}}{R_{i,j}} + \frac{V_{i,j+1} - V_{i,j}}{R_{i,j}} + \frac{V_{i+1,j} - V_{i,j}}{R_{i-1,j}} + \frac{V_{i,j-1} - V_{i,j}}{R_{i,j-1}} = I_{i,j} \tag{4.13}$$

where $V_{i,j}$ is the potential voltage at the node i, j and $I_{i,j}$ is the residual current in the node. To calculate the global resistance of the whole network, we have to simulate the injection of one unit of current on one node, and the extraction of the same current on another node. Which means $I_{i,j}$ is zero for all i, j except for the injection and extraction nodes. Having set the $I_{i,j}$ we can calculate the potentials $V_{i,j}$ at each points.

In practice, the above image is 100 x 100 pixels, which means there are 10 000 nodes, and so it forms a system of 10 000 linear equations, i.e. it is a matrix equation of type :

$$G{\cdot}\vec{V} = \vec{I} \tag{4.14}$$

Where G is a 10 000 x 10 000 conductance matrix, and vector V and I represent the vectors of potentials and residual intensities at each node.

To calculate the global resistance of the network we simulate a van der Pauw measurement. The 4 corners of the network (A,B,C and D) are used as current leads and voltage probes. In a first simulation, corners A and B are chosen as current injection and extraction nodes respectively, while we "measure" the voltage drop between corners C and D. Then a second simulation "measures" the resistance in the perpendicular direction (by swapping the roles of corners B and C). The resistance is then calculated with the standard vdP formula (section **2.3.1**).

Superconductivity

To include superconductivity in the simulation, we first attribute to each pixel a value of T_c, which is represented in the Fig. 4.7 in color scale of blue. Hence, considered separately each pixel would have its own Resistance vs. Temperature characteristic, in which we include Halperin-Nelson fluctuations (so T_c is really a T_{BKT}). For simplicity, the normal resistance of each pixel is considered uniformly equal to 1, which gives:

$$R = \frac{1}{1 + [\frac{2}{A} sinh(\frac{b}{\sqrt{T/T_c - 1}})]^2} \tag{4.15}$$

Where A is theoretically "of order 1", and b is related to the vortex core energy. We have chosen A=2 and b=0.1 uniformly across the grid.

We then choose a temperature T, and calculate the associated local conductivity for each pixel since Kirchhoff's law of current conservation concerns the conductance matrix, not the resistance. Superconductivity is thus not invoked by zero resistance pixels, but infinite conductivity. To avoid infinite values, the conductivity of each node is limited to the maximum value of 1001, which is high enough compared to the normal state, but low enough to avoid numerical problems related to very large numbers. Of course, we simulate as many temperatures as needed to obtain the global $R(T)$ curve.

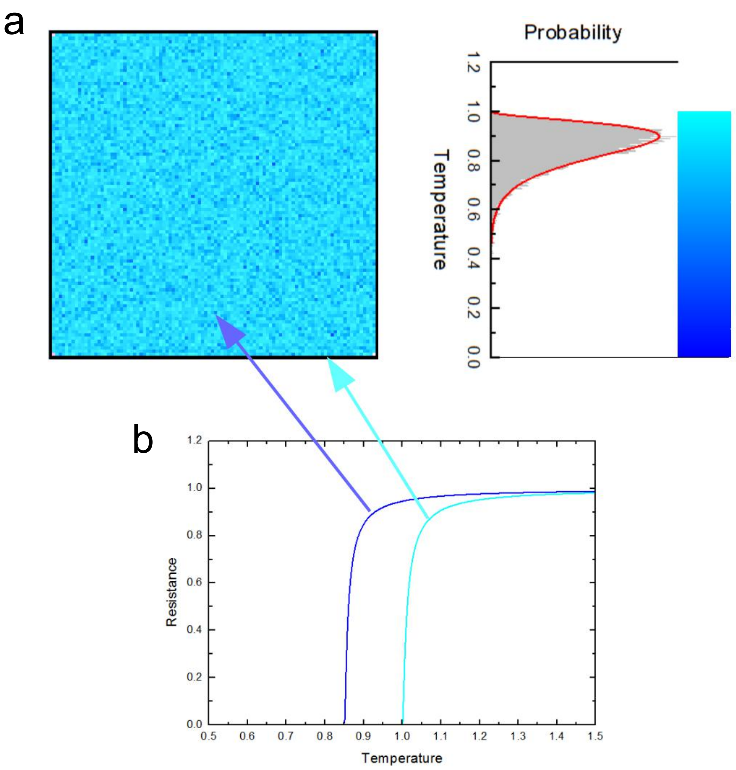

Figure 4.7: Same resistance network. **a** The shade of blue represent the local critical temperature of each pixel from 0 to 1. On the right, the probability function (red line left) used to generate the colors of the resistance network, and the actual histogram of the produced image (gray bars). The color bar indicate the correspondence between color and temperature. **b** Two examples of R(T) for two pixels of local $T_c = 0.85$ (blue) and $T_c = 1.0$ (cyan).

4.2.2 Un-correlated Random Resistor Network

We first check the accuracy of our calculation. We simulate a non-random network, with a known result, by setting all nodes homogeneously to a particular value of T_c. As shown in Fig. 4.8, calculated resistance for a homogeneous T_c of 0.9 or 1.0 accurately represent the continuous line of the Halperin-Nelson formula.

On Fig. 4.8, we have also represented the resistance calculated for the network with each node having a randomly distributed T_c according to the probability distribution shown in red. This distribution has been chosen because contrary to the more common Gaussian distribution which extend to infinity, this distribution has a well-defined maximum critical temperature (here 1.0). It can also include various degrees of asymmetry, a symmetric version would then resemble a Gaussian distribution. It is called a Gamma

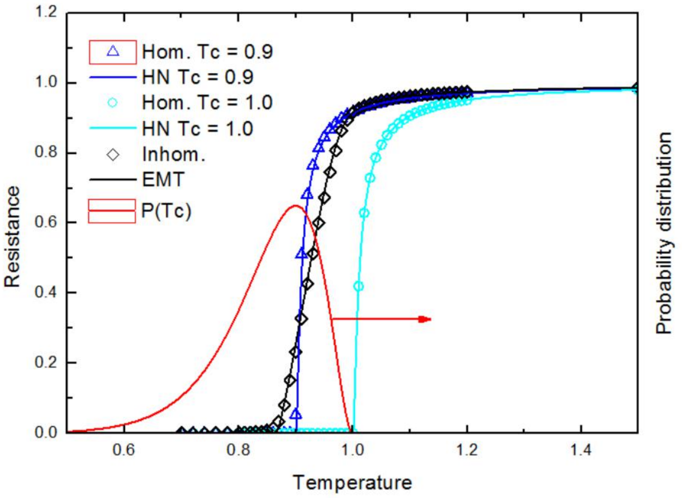

Figure 4.8: Simulation of $R_S(T)$ curve (black) with 2 homogeneous networks with $T_c = 0.9$ (blue) and $T_c = 1.0$ (cyan). The simulated $R_S(T)$ indicates an inhomogeneous network generated by the probability distribution shown in red (right axis). Continuous curves are the direct Halperin Nelson formula for the homogeneous cases, or the Effective Medium Theory calculation for the inhomogeneous case.

distribution whose formula involves Euler's Γ function:

$$P(T_c) = \frac{(T_{c,max} - T_c)^{k-1} e^{\frac{-(T_{c,max}-T_c)}{\theta}}}{\theta^k \Gamma} \tag{4.16}$$

Finally, the black line in Fig. 4.8 has been calculated using the Effective Medium Theory (EMT) [**?**]. EMT gives an implicit relation between the randomly distributed values of each nodes R_i with the global resistance R with the following formula:

$$\sum_i P(R_i) \frac{R - R_i}{R + \alpha R_i} = 0 \tag{4.17}$$

Where $P(R_i)$ is the probability distribution of the value R_i, and $\alpha = D - 1$ with D being the dimensionality. While an analytical formulation can be derived for specific situations, we will compute it numerically. Given any distribution of T_c, we calculate analytically at each temperature the actual resistance of each "node" from the actual $P(R_i)$. Then a simple dichotomy between 0 and 1 allows to converge to the solution R. The resulting black curve closely matches the values obtained from the RN simulation.

Both models agree with conventional predictions of percolation in 2D that superconductivity sets in when half of the total cells are superconducting, i.e. the global transition temperature is that of the median of the probability distribution. Fig. 4.9 presents the results of EMT and RN for two probability distributions with the same transition temperature. The EMT and RN models also allow to disentangle the contributions from fluctuations and spatial inhomogeneities. Indeed, we can see that above the maximum T_c of the probability distribution, where all the paraconductivity comes from fluctuations, the EMT and RN transition curves asymptotically match the transition from an homogeneous sample with the same transition temperature with only fluctuations. This result validates the approach to find the critical temperature of the inhomogeneous network from high temperature paraconductivity alone, thus disregarding an eventual low temperature tail in the transition.

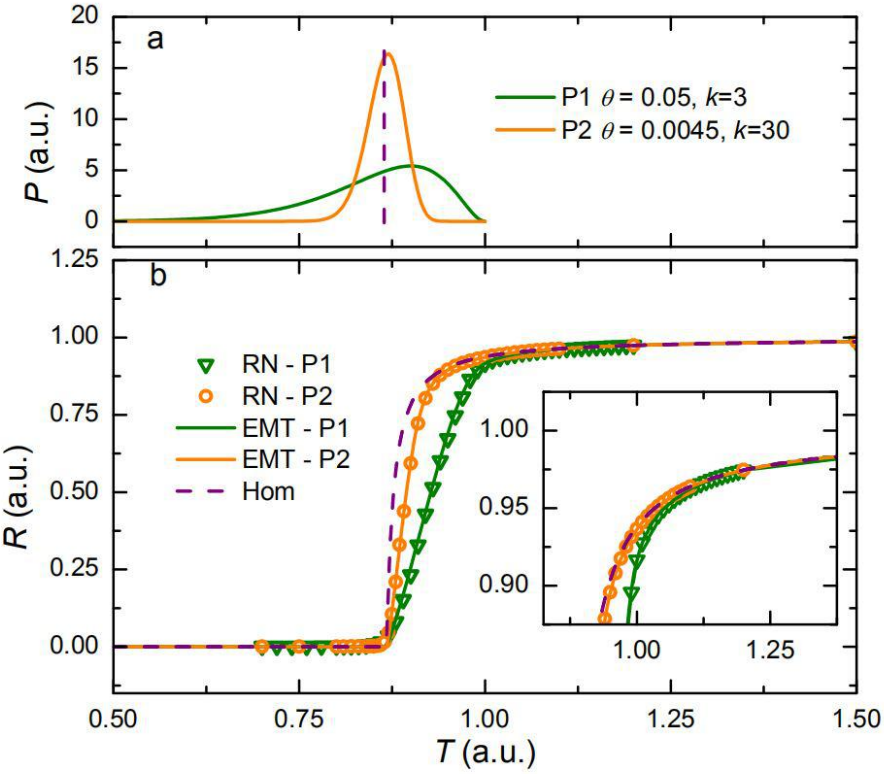

Figure 4.9: **EMT and RN comparison.** **a** Two probability Gamma distributions of transition temperatures generated to have the same median, but with different asymmetry and skewness. The median is designated by the vertical dashed line. **b** Temperature dependence of uncorrelated Resistor Network calculation (RN symbols) or Effective Medium Theory (EMT - lines) for the two probability distributions in **a**. An homogeneous sample of same transition temperature (set at the median of P1 and P2) with only Halperion Nelson fluctuations is also represented (dashed line). **Inset** Zoom of **b** in the fluctuation part.

Conversely, the presence or absence of a low temperature tail is not related to fluctuations. Indeed, if fluctuations are excluded from the EMT calculations (i.e.: the transition of an homogeneous sample would be a sharp step from 0 to 1 as shown in Fig. 4.9) the global transition temperature remains the same as with fluctuations and corresponds to the temperature of the median probability as noted before. The absence of a pronounced tail can thus be understood on the basis of inhomogeneities, which will be discussed further below. In short, and as hypothesized in the introduction, the effect of fluctuations should preponderantly be seen in the high temperature half of the derivative curve of the transition while the effect of inhomogenity should be dominant in the low temperature half of the derivative curve.

4.2.3 Inhomogeneous distribution and Temperature Derivative

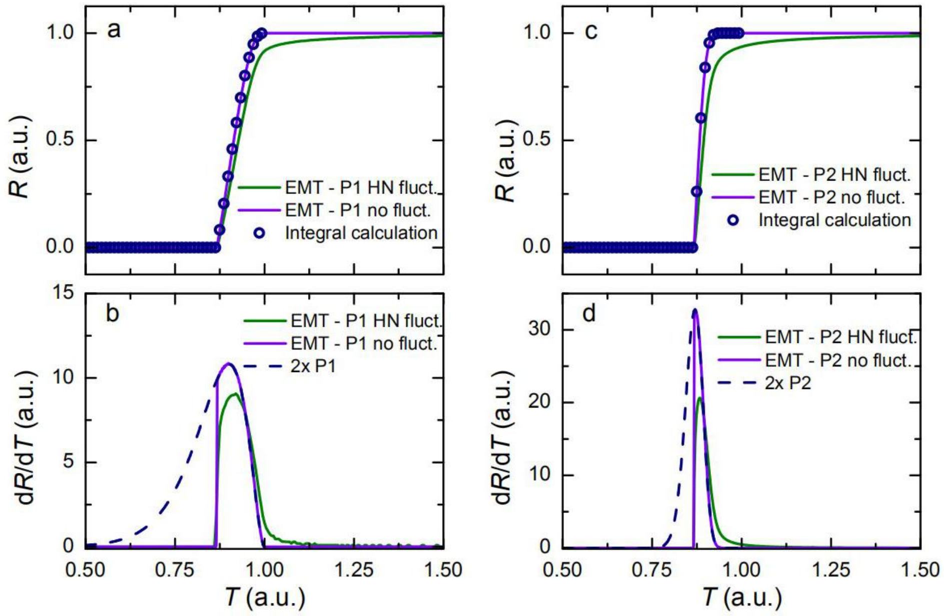

Figure 4.10: **Inhomogeneous distribution and Temperature Derivative.** **a** and **c** Temperature dependence of the resistance calculated from EMT with or without fluctuations for P1 distribution (**a**) and P2 distribution(**c**). Symbols show the calculation directly from the integral of P1 (resp. P2) distribution with respect to temperature. **b** and **d** Temperature derivative of the EMT curves from **a** (resp. **c**). The dashed line represent the P1 (resp. P2) distribution with a factor 2.

Without fluctuations, the $R(T)$ curve can be calculated analytically directly from the cumulative probability of critical temperatures, i.e. the mathematical primitive of $P(T_c)$, but restricted to above the median temperature (with a factor of 2 as we take only half the weight of the distribution). This is summarized in the following equation:

$$\begin{aligned} R(T > T_c) &= 2\left(\int_0^T P(T)dT - \int_0^{T_c} P(T)dT\right) = 2\left(\int_0^T P(T)dT - 0.5\right) \\ R(T < T_c) &= 0 \end{aligned} \tag{4.18}$$

In other words, the derivative of the resistance with respect to temperature is a direct probe of probability distribution, but only above the critical temperature as shown in Fig. 4.10. Note that this only holds without fluctuations, but it still gives an important result on the low temperature tail of the transition: if the median temperature is close to the probability maximum of the distribution (which is the case for Gaussian and Gamma distributions) the slope at the foot of the transition is high and there is no tail. Conversely, a tail is bound to appear if the probability at the median temperature is low/far from the probability distribution. This scenario cannot happen in a probability distribution with only one mode, even with a very asymmetric Gamma distribution, as it would mean that a substantial part of the density weight of the distribution is far from the maximum.

Bi-modal distribution

As noted before, it is not possible to have a pronounced tail if all nodes in the EMT are chosen in a probability distribution with only one mode. A probability distribution with 2 modes (two local maxima) can however produce a tail. We consider here the extreme case where the second maximum in the distribution represent non-superconducting nodes with a critical temperature of zero. In this situation, the aforementioned relation between cumulative probability and resistance (or equivalently probability density and resistance derivative) holds provided we exclude fluctuations. We show in Fig. 4.11 that as the proportion of non-superconducting nodes increases from 0 to o.25 to o.5, the median temperature shifts at lower temperature away from the maximum of the distribution. Hence, a tail forms mechanically as the lower part of the transition now coincides with the smaller probability weight. At 50% non superconducting nodes the tail goes to zero temperature, and the derivative of the $R(T)$ curves describes completely the probability distribution.

The agreement between EMT and RN simulations still holds with the inclusion of fluctuations as shown in Fig. 4.12, in agreement with our previous statement that fluctuations have little impact on the tail part of the transition.

Clearly it is not possible to completely de-correlate fluctuations from inhomogeneities in experiments. However, by analyzing the derivative of EMT and RN simulations, it does appear that the higher temperature part of the derivative peak in the experiments is more related to fluctuations than inhomogeneity in the sample while fluctuations have little effect on the appearance of the low temperature tail.

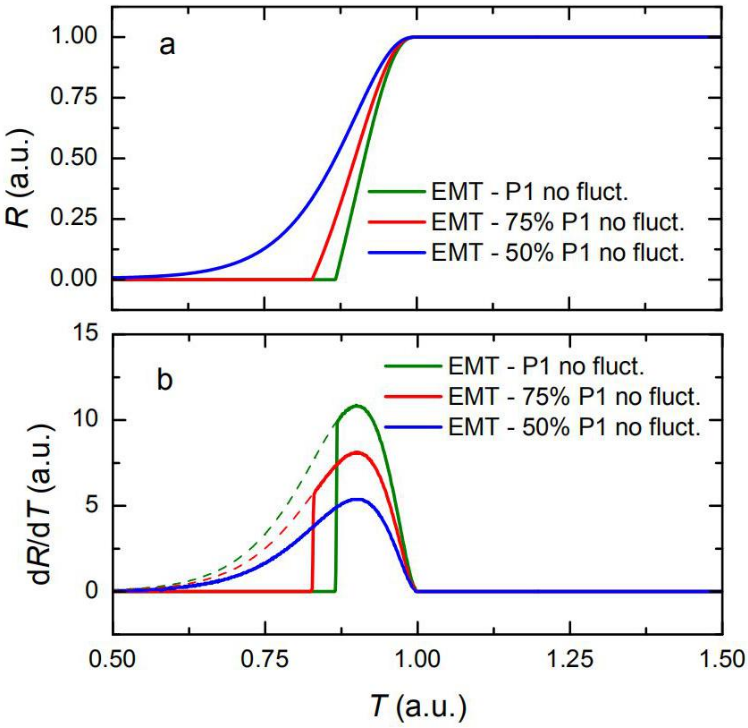

Figure 4.11: **Bi-modal distribution without fluctuation.** **a** Temperature dependence of the resistance calculated from EMT without fluctuations for P1 distribution, 75% of P1 and 50% of Pa (complementary weight is set at zero temperature). **b** Temperature derivative of the EMT curves from **a**. The dashed lines represent the P1 distribution with a factor 2 and 1.5. P1 is numerically identical to the 50% curve.

Spacial correlation effects

A bi-modal distribution of T_c is not the only mechanism for generating a low temperature tail in the $R(T)$ curve. We have performed several RN simulations with the same probability distribution of T_c but with ordered or disordered spatial correlations which of course decrease the randomness. With spatial correlations a pair of nearby nodes will no more necessarily have a completely uncorrelated random T_c with a greater probability of having similar local T_c.

In order to compare similar things, we will stick to the same size of network, and the same probability distribution, but impose spatial correlations. In practice this is achieved by taking a non-random network with a pattern and repeatedly twitching the local T_c values until the probability distribution approximates the targeted distribution. As we only change the local T_c by a small amount each time, the resulting pseudo-random network conserve most of the features of the random network. The three networks shown in Fig. 4.13 thus have almost the same distribution of T_c globally but are very different

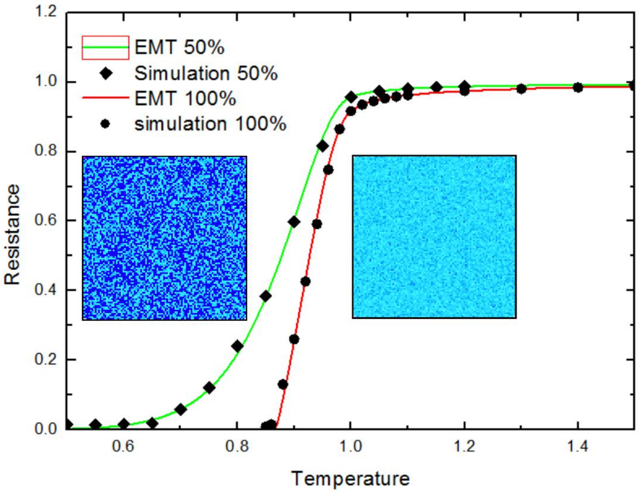

Figure 4.12: Simulation of $R_S(T)$ curve with 2 inhomogeneous networks and their respective EMT calculations. "100%" is the same network as in Fig. 4.8, while "50%" has been generated with the same shape of distribution but with 50% of its weight moved to 0.

when comparing their spatial distributions.

The result of the simulation on these three networks is shown in Fig. 4.14. As shown in Fig. 4.8, the uncorrelated network closely matches the result of the EMT calculation. However, despite having almost the same T_c distribution, the correlated networks deviate significantly from EMT. Note that since the only input of EMT is the distribution of critical temperature, all three should have the same EMT result, which is evidently not the case. This is explained by the fact that EMT ignores spatial correlations. Indeed, the transition in the most "connected" network (blue diamonds) is steeper, while it is broader in the less "connected" network (red circles). Remarkably, despite having a steeper transition, the "connected" network shows a persistent low temperature tail. Another important aspect is that all three coincide in the high temperature part, even at temperatures below the purely fluctuating regime.

Of course correlated patterns can be infinitely varied but there is a common trend: more "connected" networks have sharper transitions, with the exact shape depending on the pattern. One special case is the case of "randomly" correlated network, in which we only have short range correlations (patches) but no long range order. We give below two examples of such randomly patchy networks (Fig. 4.15). The green symbols represent a random network whose patches are allowed to superimpose on one another without any correlation between patches (inset of Fig. 4.18 bottom right panel) while the orange symbols represent quasi-uniformly distributed non-overlapping patches ((inset of

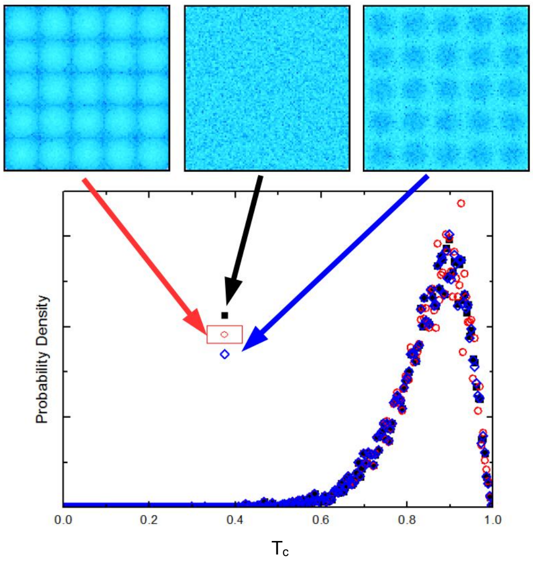

Figure 4.13: Two Examples of correlated-random resistor networks (left and right) having almost the same probability density of T_c as the purely uncorrelated random resistor network (center), as shown by the plot. Note that in some parts of the plots (0.4 to 0.8) all 3 are very closely matched, which is not an accident: the left and right networks were generated using the actual histogram of the network shown in the center.

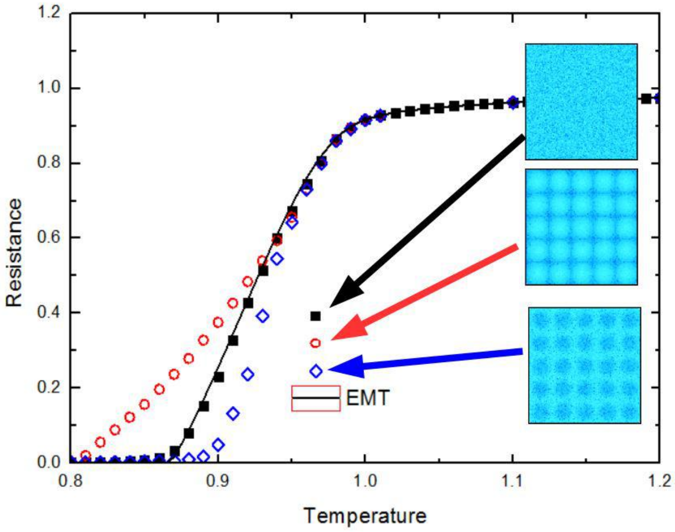

Figure 4.14: Simulations and EMT calculations of the uncorrelated network (black), and two spatially correlated networks (red and blue) as shown in Fig. 4.13.

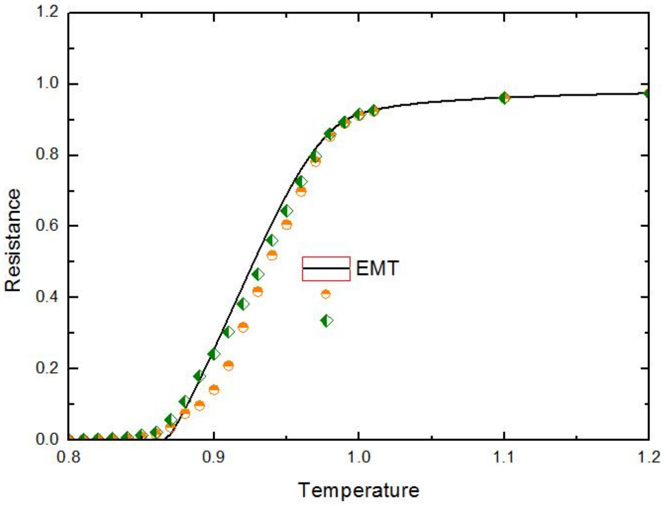

Figure 4.15: Simulations of two networks with short range correlation but no long range order, compared with the EMT. More explanations are given in the main text.

Fig. 4.18 bottom left panel)). It appears unsurprisingly that the random patch network (green symbols) is quite close to the purely random network (represented here by the EMT). However, the quasi-uniformly distributed patch network (orange symbols) has a significantly "connected" characteristic.

In figure 4.16 we show the derivatives of the $R(T)$ curves obtained for 6 simulations of resistor networks, with or without short/long range correlations and more or less connectivity. As we will discuss later, the shape of the derivative in more "unconnected" networks does not seem to be compatible with experimental results. However, the other examples display only subtle differences.

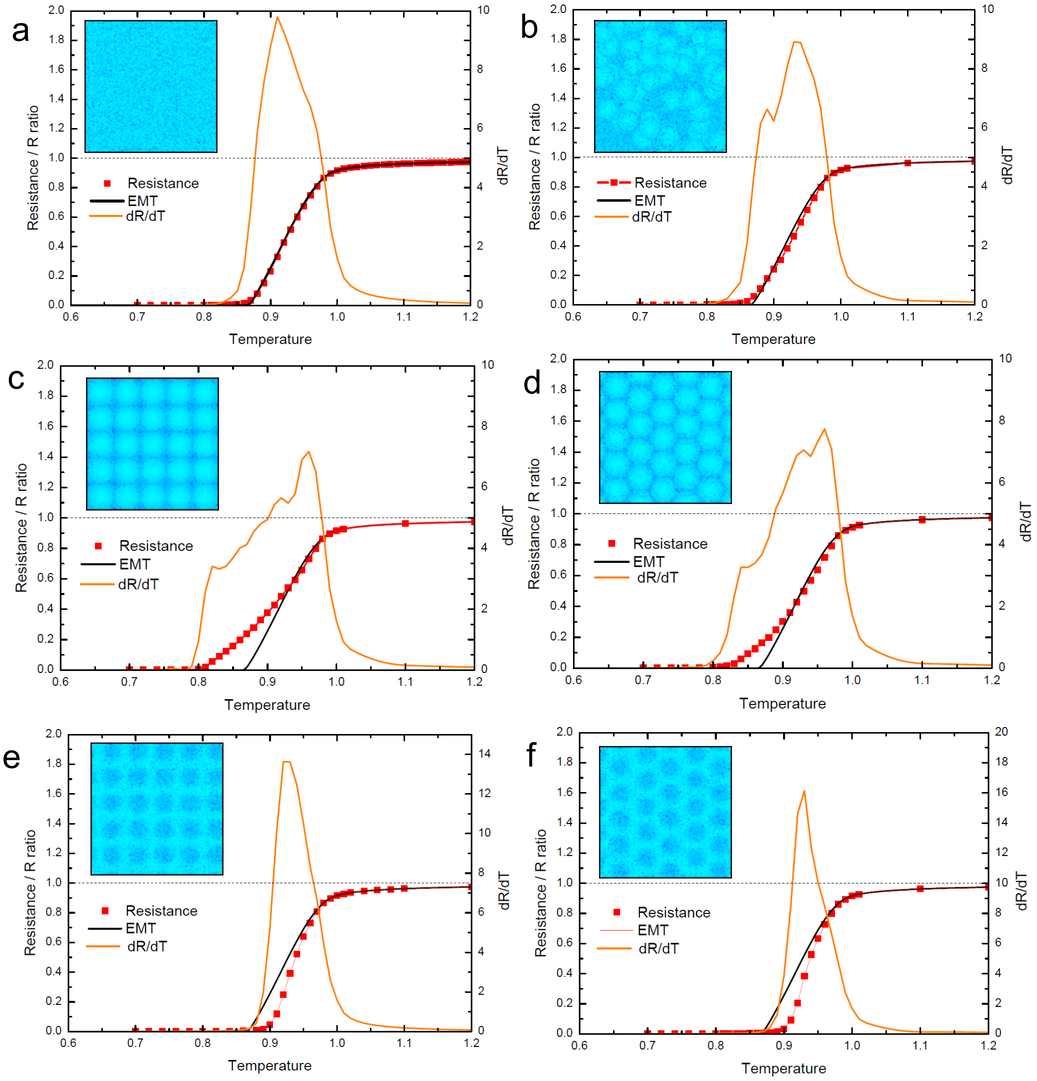

Figure 4.16: Simulations of the $R(T)$ curves of 6 networks compared with the EMT, and their temperature derivatives. **a** non-spatially correlated network. **b** short range correlation. **c** and **d** more “unconnected” networks. **e** and **f** more “connected” networks

4.2.4 Anisotropy

Since we are simulating the experimental van der Pauw measurement, we will also investigate the anisotropy between the horizontal $R_h = V_{AB}/I_{CD}$ and vertical resistances $R_v = V_{BC}/I_{DA}$ (Fig. 2.13).

Firstly, we can safely say that an homogeneous resistor network is perfectly isotropic throughout the transition. It follows that, as real samples do present anisotropy, they are unlikely to be homogeneous.

Secondly, in theory a perfectly homogeneously randomized resistor network should also be isotropic throughout the transition, but in practice, some non-spatially correlated networks do appear to have significant anisotropy in the RN simulation. We show as an example in Fig. 4.17 (top and middle pannels) two non spatially correlated networks with the same probability distribution and displaying various degrees of anisotropy in the middle of the transition. The presence of a bi-modal distribution (bottom panel) gives similar results. This anisotropy may also result from the finite (and quite small) size of the network that may allow substantial anisotropy to develop. However, more simulations on bigger networks would be required to verify that possibility.

Finally, inhomogeneity does appear to enhance anisotropy but not in a systematic way. Indeed, the anisotropy ratio appears quite unpredictable, as shown for several spatially correlated networks in Fig. 4.18. Furthermore, these simulations may suffer from the same size limitation problem as the non-spatially correlated ones. Hence, it is difficult to draw conclusions on origin of the resistance anisotropy in real and simulated samples.

In conclusion, the resistor network model is used to simulate the vdP resistance measurement of inhomogeneous superconductivity in two dimensions. The EMT curve accounts well for random inhomogeneity in 2D. The shape of the resulting superconducting transition is affected by multiple parameters: the probability distribution, the eventual presence of non-superconducting parts, the presence of long-range or short range correlations. A significant tail can result from a fraction of non-superconducting part in the network and/or spatial correlations. The connected nature and eventual long-range order of these correlations also influences the measurement. However, the presence or absence of a tail seems not related to the fluctuations. Fluctuations mainly appears in the higher temperature part of the derivative peak. To conclude this part on simulations, the effect of fluctuations is preponderantly seen in the high temperature half of the derivative curve of the transition. The effect of inhomogenity is dominant in the low temperature half of the derivative curve.

In the next section, I will compare these models with the curves extracted from the experimental data of our one u.c. BSCCO samples.

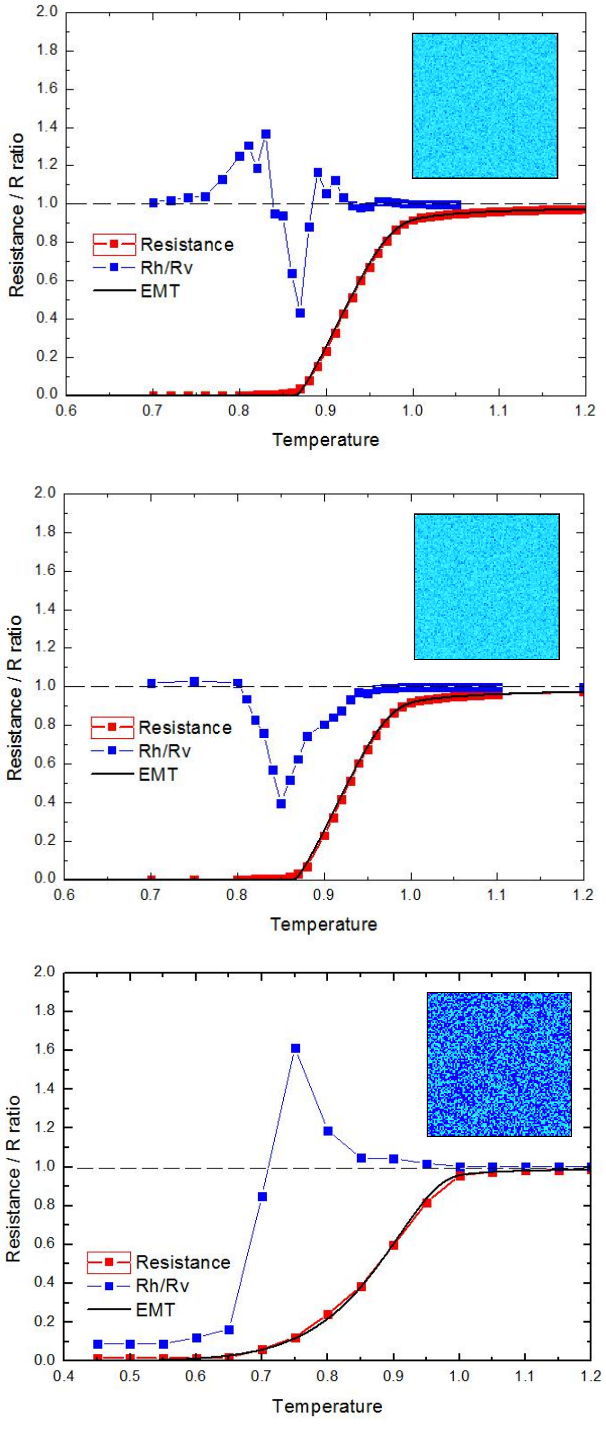

Figure 4.17: Uncorrelated random networks, two different mono-modal networks (top, middle), and a bi-modal half superconducting network(bottom).

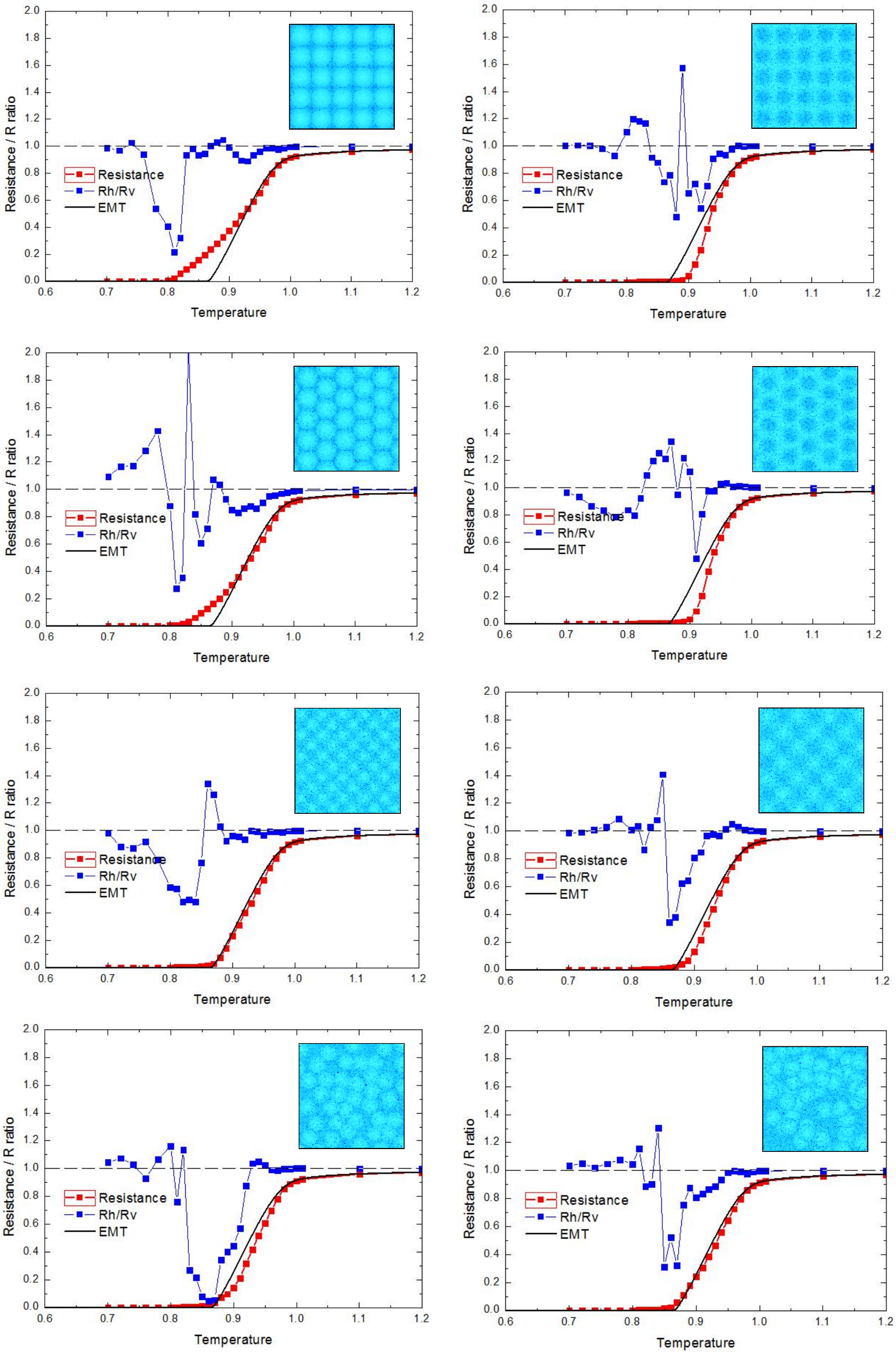

Figure 4.18: Simulation of several different spatially correlated networks. Note that in the following graphs we kept all data for the R_h/R_v ratio, even below T_c (which is not possible in real samples).

4.3 Simulation and experimental analysis comparison

In this section, we will analyse the data of three one u.c. BSCCO samples at their optimal doping (∼0.16). The transport measurement data are studied using the ratio $R_S(T)/R_N(T)$ (R_N normal-state resistivity), the derivative of $R_S(T)/R_N(T)$, as well as the anisotropy of the R_S measurement for understanding mechanisms related to fluctuations and inhomogeneity in the light of the understanding gained form the simuations in the preceding sections. The samples used in this section were fabricated with the same method introduced in the previous chapters, but without annealing in the air.

4.3.1 Temperature derivative

The temperature dependence of sheet resistance curves $R_S(T)$ and normalized resistance curves R_S/R_N of three one unit-cell BSCCO samples (labelled C, D, E) at their optimal doping (∼0.16) are shown in Fig. 4.19. The form of the normal-state resistance $R_N(T)$ is determined as $R_N(0) + BT^m$ (B and m are constants). The critical transition temperatures T_c, defined here as the temperature where the sheet resistance vanishes, are respectively 50.4 K, 80.4 K and 80 K for sample C, D and E.

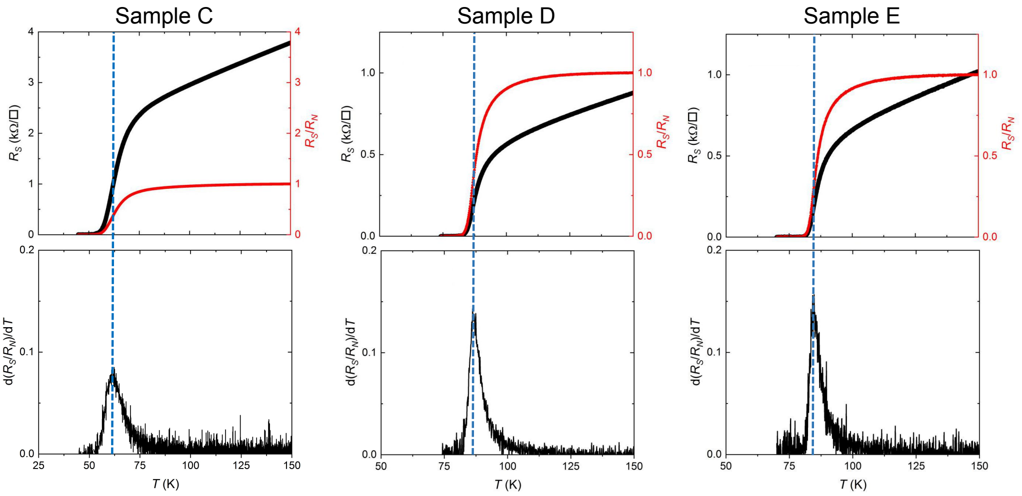

Figure 4.19: **Analysis of experimental data. above** Temperature dependence of sheet resistance $R_S(T)$ (*left, black*) and its normalisation to the normal-state R_N (*right, red*). **below** Temperature derivative of R_S/R_N from the curves above. The dashed lines represent the maximum of the derivative curves.

The corresponding temperature dependence of the derivative curves is calculated for sample C, D and E. The T_{max}, which corresponds to the peak of the temperature derivative curves, is respectively approximately 61 K, 86.2 K and 84.5 K respectively for samples C, D and E. Sample C is a disordered inhomogeneous sample which leads to a low critical temperature at optimal doping while both D and E are high quality samples [94] and can be compared to each other. The resistive transition in sample D is also measured in the presence of a perpendicular magnetic field. When an external magnetic field is applied normal state vortices corresponding to flux lines appear in an ordered lattice penetrating the sample. The temperature dependence of the sheet resistance curves and the normalization to the normal-state R_S/R_N is shown in Fig. 4.20. It can be clearly observed that with higher magnetic field, both the width and the tail of the sheet resistance curve increase. Hence T_c decreases a lot, with the values of 80.4 K (B=0), 64 K (B=1 T), and 58 K (B=2 T). This change is qualitatively similar to that in Fig. 4.11, which shows the effect of non-superconducting regions in the network.

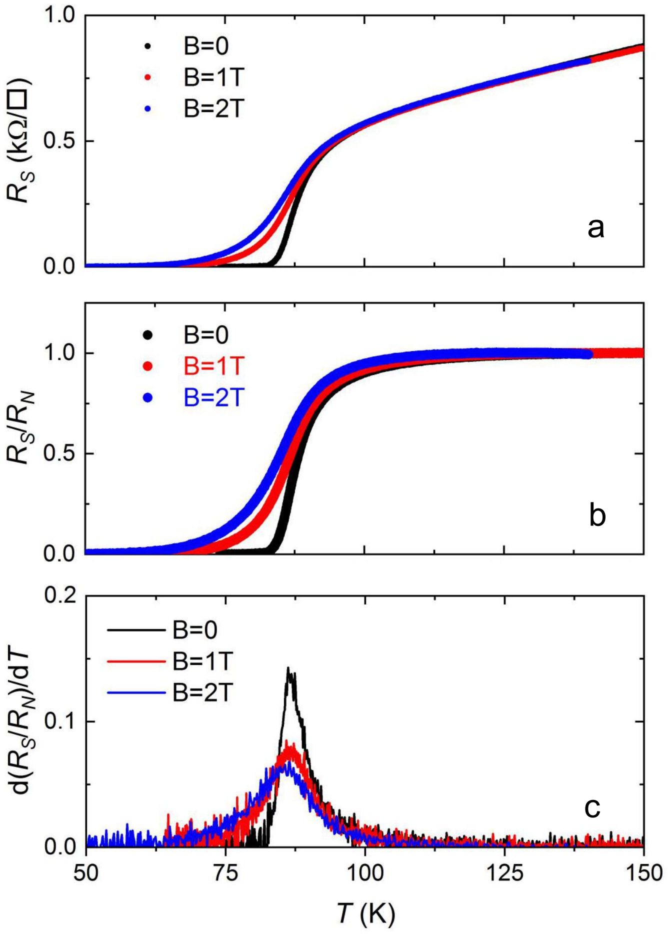

Figure 4.20: **Magnetic field and 2D superconductivity.** **a** and **b** Temperature dependence of sheet resistance R_S and their normalisation to the normal-state R_S/R_N of 1 u.c. BSCCO sample (D) at optimal doping with different magnetic field. **c** Temperature derivative of the curves R_S/R_N in **b**.

Several qualitative conclusions may be reached by studying the transitions and the derivatives, in the light of our earlier findings from simulations:

1) The transitions in the high quality samples D and E are sharp and imply not only relatively homogeneous samples with a narrow probability distribution of critical temperatures, but also eventually a 'connected' nature of the underlying network for any inhomogeneity if present.

2) The transition in sample C with a lower T_C is logically broader. However the derivative curve remains peaked implying underlying connectivity in the inhomogeniety.

3) The extent of the high temperature (HT) half of the peak of the derivative curve is about 20K for the three samples. The extent of the low temperature (LT) half of the peak is about 10K for sample C while it is 3-4K for samples D and E. This tells us that the HT part of the derivative curve is unchanged in the three samples. Our understanding being that this part is dominated by fluctuations, this means that the associated fluctuation regime is identical, which is not a surprise given that the material and the doping level are the same. When inhomogeneity increases it is the extent of LT half of the peak of the derivative curve which increases substantially in going from samples D and E to sample C, signifying that this part is dominated by the effects of inhomogeneity.

4) This conclusion is reinforced by studying the derivative curves in Fig. 4.20. The extent of the HT part of the derivative peak increases marginally by 2-4K from its zero-field value of about 20K. However the extent of the LT part of the derivative peak increases dramatically from about 4K to beyond 12K and 20K at 1T and 2T. Again inhomogeneity (here an ordered network of normal state vortices) acts principally on the LT part of the derivative peak.

These observations confirms our starting hypothesis as well as our intermediate conclusion reached from simulations: The effect of fluctuations is preponderantly seen in the high temperature half of the derivative curve of the transition. The effect of inhomogenity is dominant in the low temperature half of the derivative curve.

4.3.2 Anisotropy

The experimental results of measured anisotropy of sample C, D and E are shown here in Fig. 4.21. A substantial anisotropy is measured on all 3 samples at temperature well above T_c. Such pronounced anistropy is similar to the simulated anisotropy in spatially correlated random networks of Fig 4.18. However in two similar samples, D and E, the anisotropy is noticeably different. As noted previously, it is not possible to draw major conclusions on the presence or shape of such correlations in real samples at this time.

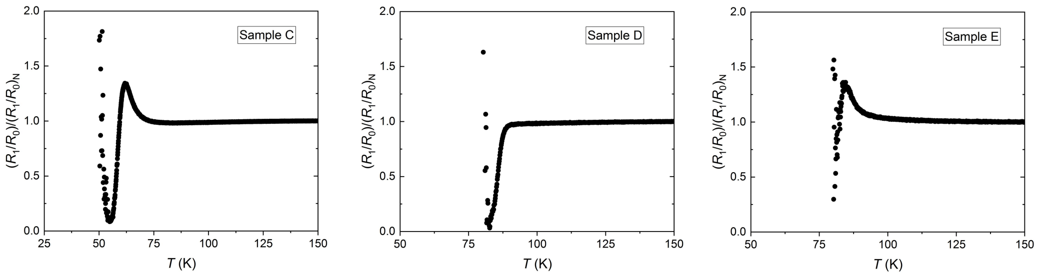

Figure 4.21: Van der Pauw anisotropy for sample C, D and E, with $R_0 = V_{AB}/I_{CD}$ and $R_1 = V_{BC}/I_{DA}$. The ratio R_1/R_0 is fitted by the normal-state $(R_1/R_0)_N$ with the same type of the fitting formula as the normal-state resistivity $R_N(T) = R_N(0) + BT^m$.

4.3.3 Conclusion

In this chapter, we discussed the effects of inhomogeneity and fluctuations on superconducting transition on mesoscopic and nanoscopic scale on the optimally doped one unit-cell BSCCO-2212 samples. We prepared the groundwork and confirmed both with simulations and with analysis of transport measurements. We investigated how the temperature derivative of sheet resistance curve are affected by the effects of inhomogeneity and fluctuations. Then we also did a small analysis of the effect of inhomogeneity by comparing homogeneous and inhomogeneous samples on the one hand and an homogeneous sample in which we introduce inhomogeneity in the form of an ordered network of non-superconducting regions. Finally we came to the conclusion that inhomogeneity mainly influence the superconducting transition on the lower temperature part of the derivative curve, while fluctuations on the higher temperature part of the derivative curve. More details will be explained in chapter 5, where we discuss mainly the effects of fluctuations.

Chapter 5

Fluctuations, doping and high T_c superconductivity

In this chapter, we will focus on the effects of fluctuations on the superconducting transition with 5 one u.c. BSCCO-2212 samples as function of doping. We will compare the fluctuations effects between the overdoped and the underdoped regime.

5.1 What can we learn from experiment

In the last chapter we established on the basis of systematic comparisons between experiment and simulations of 2D superconductivity that sheet resistance measurements of the transition are indelibly marked by inhomogeneity and quantum fluctuations. We found further that the derivative of the normalized sheet resistance as a function of temperature (which we will abbreviate simply by 'derivative') presents an asymmetric peak at the superconducting transition. The LT (low temperature) half of this peak is dominated by effects of inhomogeneity while the HT (high temperature) half of the peak, notably the asymmetric HT tail, is dominated by quantum fluctuations. In the last chapter we studied the effects of inhomogeneity, mainly through simulations. In this chapter we address the effects of fluctuations. In the 2D BSCCO system we have earlier established the comprehensive phase diagram as a function of doping [94]. We have notably pin-pointed the critical doping of p=0.19 which separates two parts of the superconducting dome [110]. Though the nominal optimal doping is p=0.16, the critical value could be associated to an underlying quantum critical point or to a transition between two different regimes identified roughly by the underdoped and overdoped parts of the dome. In chapter 3 [113] we have measured another quantum phase transition, the SIT as a function of doping, where strongly undoped 2D BSCCO transits from an insulator to a superconductor. We concluded that this transition in the strongly underdoped region is compatible with a superconducting state where Cooper pairs (bosons) could exist both above and below the critical temperature, and a superconducting state which corresponds to the development of phase coherence between these existing Cooper pairs at the critical temperature. In this chapter we wish to take this analysis further into the less underdoped and the overdoped regions. Indeed the superconducting wave function is characterized [2] by an amplitude and a phase, both of which have to be well defined for superconductivity to appear.

Isolated Cooper pairs may form at some 'high' temperature as a result of a strong interaction (strong coupling). However these may not be compatible with a condensed quantum ground state if there is no phase coherence which could develop only at a lower temperature. The intermediate temperature range should hence be marked by fluctuations of this phase [158, 159]. On the other hand, in a more 'common' scenario of classical superconductivity (weak coupling), the superconducting condensate appears with the simultaneous establishment of the amplitude and the phase of the superconducting wave function, at a single temperature which is the critical temperature, with amplitude and phase fluctuations in a limited temperature range above it.

Fluctuations of the superconducting state above critical temperature can thus inform us about the nature of the superconducting state below T_C. In the past [160, 161] several works have examined the nature of fluctuations by examining the shape of the superconducting transition in both 2D and bulk samples in classical and high T_C superconductors. Theories, more or less comprehensive, exist for describing the effects of fluctuations both of phase and amplitude and the interplay between them [150, 162]. However we have seen in Chapter 4 that inhomogeneity, about which it is not possible to have even cursory information in a macroscopic transport measurement, profoundly influences the shape of this transition. It is not a surprise then that many of the above works do not provide a conclusive picture.

In this chapter we approach this problem armed with several tools. Firstly we know that quantum fluctuations are enhanced in 2D. Secondly the small coherence length of high T_C superconductivity also enhances fluctuations. This means that the effect of fluctuations will be more marked in a measurement. Thirdly, our earlier work on the 2D BSCCO system helps us to clearly establish the parameters of the study. Finally, space charge doping provides us the means to electrostatically dope a given one u.c. BSCCO sample over large regions of the phase diagram. However we confine our qualitative analysis to the HT half of the derivative and do not parametrically fit our measurements with available theoretical models, for the reasons given above.

5.2 Analysis of experiments

In this section we introduce the analysis of temperature dependence of sheet resistance in both the overdoped and the underdoped side in one unit-cell BSCCO samples. We develop here a simple criterion for measuring the temperature range of fluctuation above T_c and analyse a large gamut of measurements from this and earlier works in our group [94, 110, 113].

Two temperatures can be identified on the HT half of the derivative. The maximum temperature corresponding to the peak of the derivative and the maximum slope which is roughly the midpoint of the transition and which we can identify with T_c in this chapter because it signifies the onset of the superconducting phase. The other temperature corresponds to the start of the high temperature tail of the derivative, which is defined here arbitrarily at a threshold of 5 percent of the peak (Fig. 5.1). Since this is the temperature at which the normalized sheet resistance starts deviating from its normal state value, we identify it by T_f, the temperature at which fluctuations start to be detected. Then, Δ_T is given by $T_f - T_C$ and signifies the temperature range over which fluctuations occur (as measured by our sheet resistance measurements) before superconductivity sets in. We also introduce a normalized quantity $\Delta_n = (T_f - T_C)/T_C$. In this chapter we will determine Δ_T and Δ_n for a variety of measurements across a wide doping range.

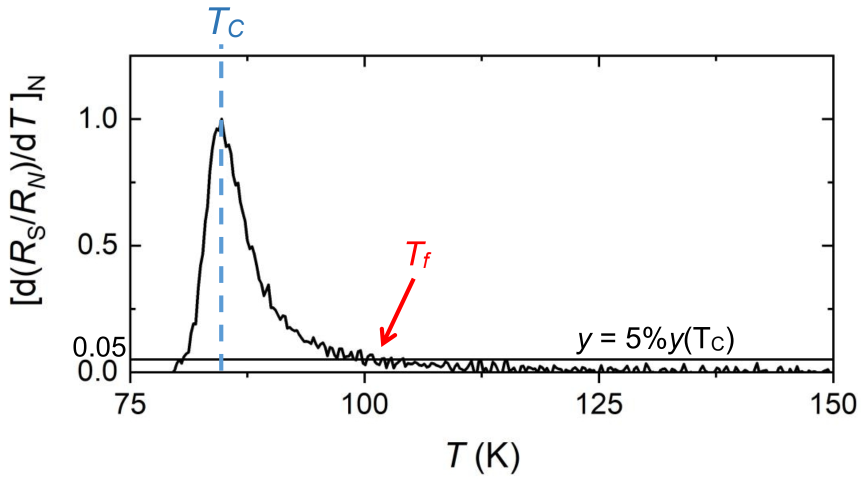

Figure 5.1: Determination of the T_C and T_f temperatures. This normalized derivative curve is taken as an example to show the dtermination of T_C and T_f. It is extracted from Fig. 5.5**d** with $p = 0.16$ (black curve). T_C is the temperature where the curve arrives at the maximum, as shown by the blue dotted line. T_f is taken as the cross point (red arrow) between the derivative curve and the horizontal solid line ($y = 0.05$), that is the 5% of the maximum of the derivative curve. Thus for this curve, $T_C = 84.7$ K and $T_f = 100.6 \pm 1$ K.

5.2.1 Overdoped 2D BSCCO

Here we show the analysis of two one u.c. BSCCO samples, labeled respectively D and G, on the overdoped side of the phase diagram. First for sample D, the initial doping level is optimal (black curve in Fig. 5.2). With space charge doping we p-dope first to the maximum hole-doping level and then n-dope the sample step by step back to the optimal doping. The doping order is indicated in Fig. 5.2**a** with grey arrows from left to right. The critical temperature T_c decreased from 81 K to 52 K The normalized sheet resistance curves $R_S(T)/R_N(T)$ are shown in Fig. 5.2**b**, with the normal-state resistivity $R_N(T) = R_N(0)+BT^m$ (B and m are constants). The corresponding derivative curves are presented in Fig. 5.2**c**. The doping levels are calculated with the empirical formula $T_c(p)/T_c(p_{opt}) = 1 - Z(p-p_{opt})^2$, which has been introduced in chapter 3. In Fig. 5.2**d**, the maximum of each derivative curve is normalized to value 1. This procedure is to simplify the extraction of the start of the high temperature tail of the derivative curve, as explained in Fig. 5.1. Sample G is subjected to a similar procedure as shown in Fig. 5.3. The critical temperature changes between 82.7 K and 58.9 K. From these two examples the following conclusions can be reached by analysing the derivative:

1) In this overdoped region, the shape of the derivatives at different doping show that Δ_T decreases slightly but observably as doping increases, as seen also through the narrowing of the derivative peak (the area of which is normalised by construction since the sheet resistance is normalized before the derivation).

2) Both T_f and T_C shift almost rigidly (if we ignore the small decrease in Δ_T) to lower temperature as doping increases.

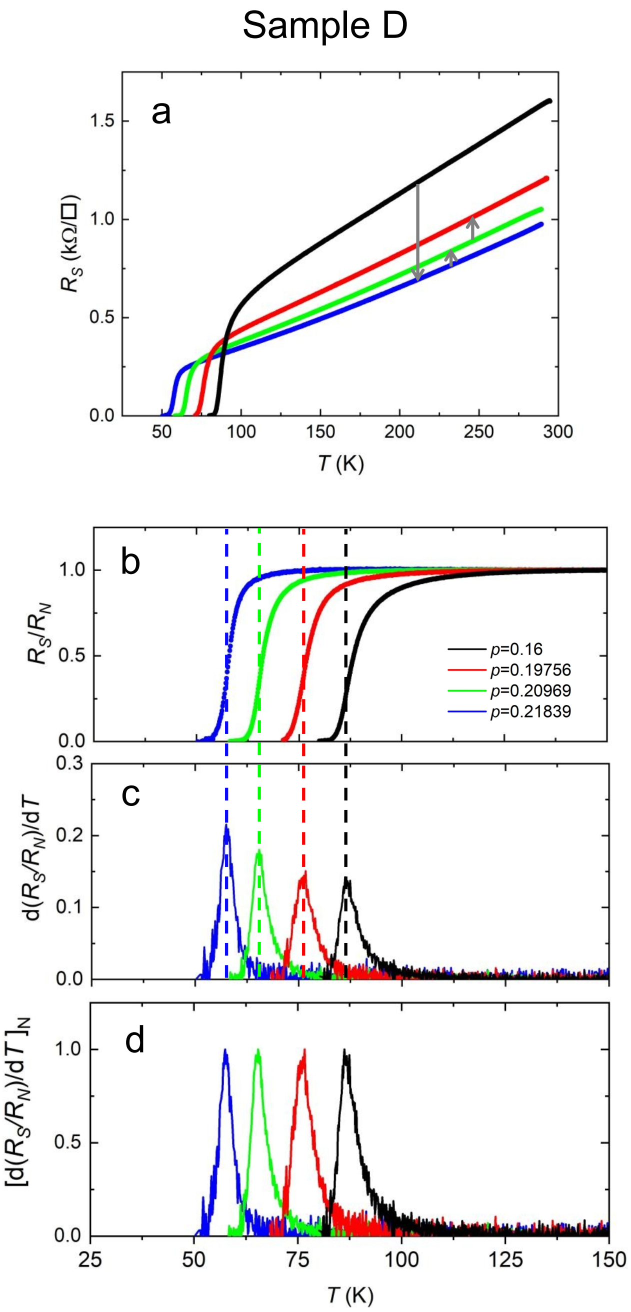

Figure 5.2: **Derivative and 2D superconductivity in overdoped region.** **a** Temperature dependence of sheet resistance curves $R_S(T)$ of 1 u.c. BSCCO sample labelled D from 25 K to 300 K. The black curve shows the optimal doping level, and the grey arrows from left to right indicate the order of doping. **b** Temperature dependence of the normalised sheet resistance R_S/R_N on the same sample as **a** from 25 K to 150 K. $R_N(T) = R_N(0) + BT^m$ (B and m are constants). **c** Temperature derivative of the curves R_S/R_N in **b**. The dotted lines represent the highest points of the derivative curves. **d** The maxima of curves from **c** are normalized to 1 respectively.

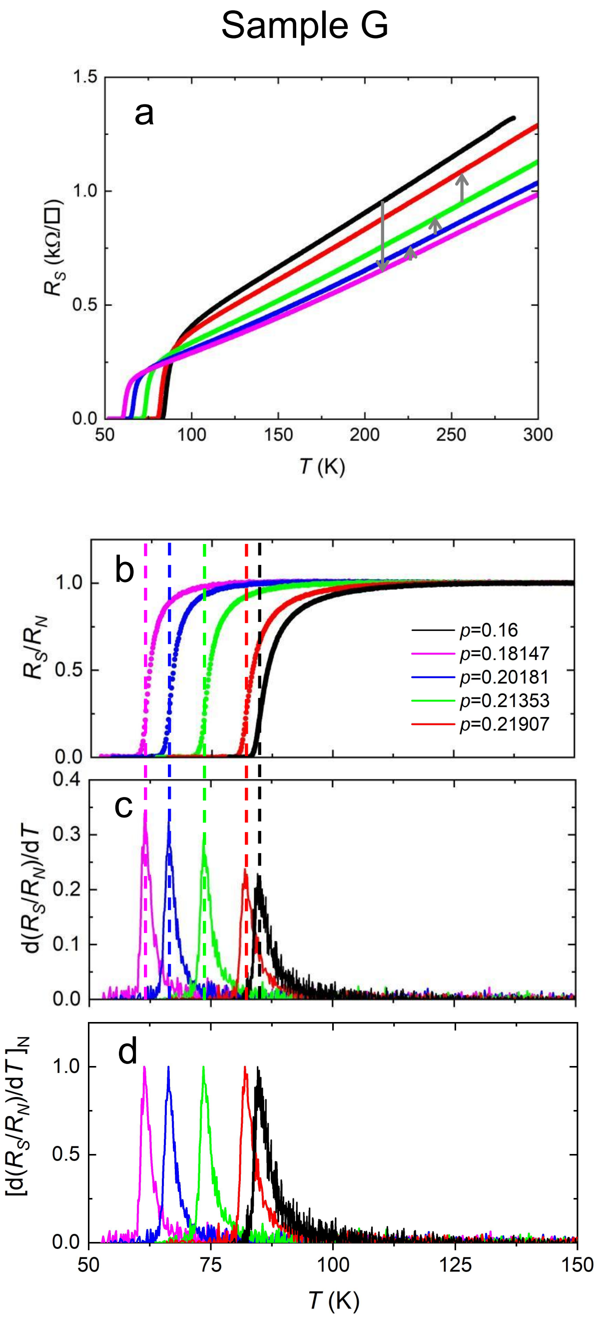

Figure 5.3: **Derivative and 2D superconductivity in overdoped region.** **a** Temperature dependence of sheet resistance curves $R_S(T)$ of 1 u.c. BSCCO sample labelled G from 50 K to 300 K. The black curve shows the optimal doping level, and the grey arrows from left to right indicate the order of doping. **b** Temperature dependence of the normalised sheet resistance R_S/R_N on the same sample as **a** from 50 K to 150 K. $R_N(T) = R_N(0) + BT^m$ (B and m are constants). **c** Temperature derivative of the curves R_S/R_N in **b**. The dotted lines represent the highest points of the derivative curves. **d** The maxima of curves from **c** are normalized to 1 respectively.

5.2.2 Underdoped 2D BSCCO

In this part, three one u.c. BSCCO samples C, E and F are presented respectively in Fig. 5.4, Fig. 5.5 and Fig. 5.6. The sheet resistance curves of sample C on the underdoped side were shown in Fig. 5.4**a**. The sample was electron-doped step by step with space charge doping with the order shown by grey arrows from left to right in Fig. 5.4**a**, leading to a change of T_c between 26 K and 51 K. Then all the sheet resistance curves were normalized by their normal-state resistance $R_N(T) = R_N(0) + aT - bT^2$ (a and b are constants). The resulting curves R_S/R_N are plotted in Fig. 5.4**b**. The corresponding derivative curves are presented in Fig. 5.4**c**. The doping levels are calculated with the empirical formula $T_c(p)/T_c(p_{opt}) = 1 - Z(p - p_{opt})^2$. In Fig. 5.4**d**, the maximum of each derivative curve is normalized to value 1. The same analysis for sample E and F are shown in Fig. 5.5 and Fig. 5.6. The critical temperature changed from 76.5 K to 80 K for sample E, and from 12 K to 25.4 K for sample F. As in the overdoped case the following conclusions can be reached by analysing the derivatives of the underdoped region of the phase diagram:

1) As in the overdoped case, T_f and T_C and Δ_T and Δ_n can be identified for further analysis.

2) In this underdoped region, a visual examination show that Δ_T *increases* substantially as doping increases, as seen also through the substantial broadening of the derivative peak (the area of which is normalised by construction as mentionned for the overdoped curves).

3) While T_f stays nearly the same, as p-doping is decreased T_C shifts to lower values.

4) These observations are qualitatively and quantitatively different from those found in the overdoped region.

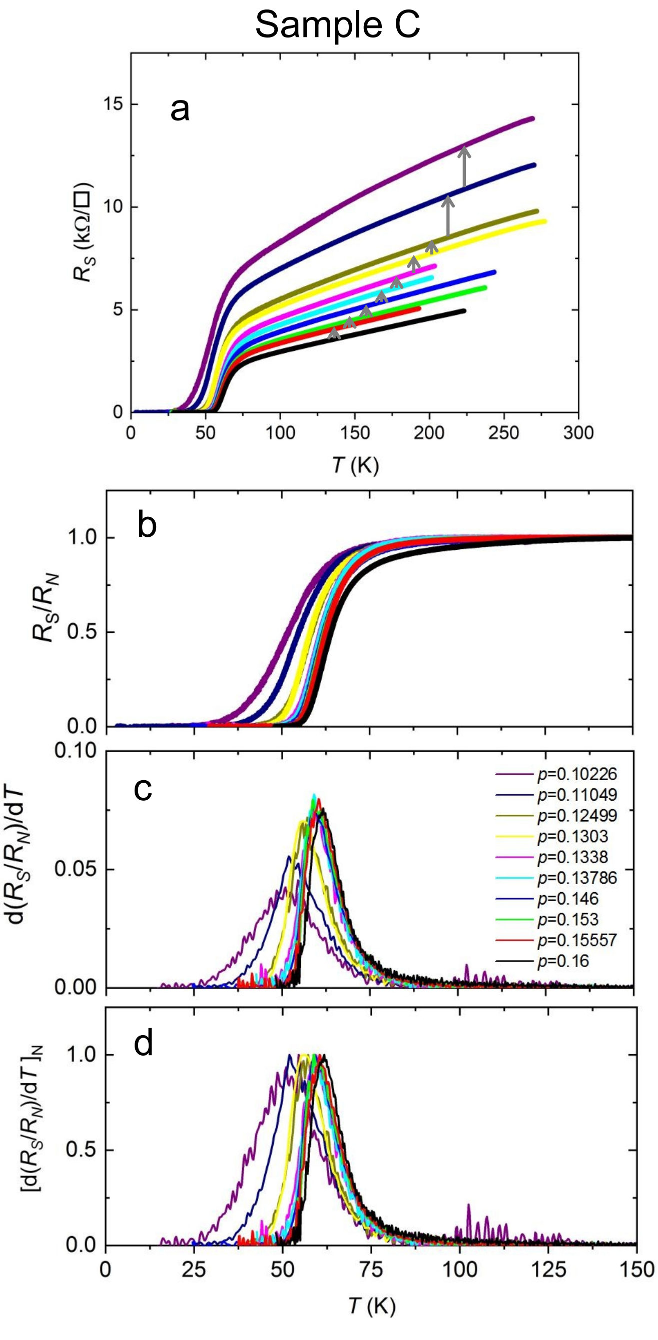

Figure 5.4: **Derivative and 2D superconductivity in underdoped region.** **a** Temperature dependence of sheet resistance curves $R_S(T)$ of 1 u.c. BSCCO sample labelled C from 0 to 300 K. The black curve shows the optimal doping level, and the grey arrows from left to right indicate the order of doping. **b** Temperature dependence of the normalised sheet resistance R_S/R_N on the same sample as **a** from 0 to 150 K. $R_N(T) = R_N(0) + aT - bT^2$ (a and b are constants). **c** Temperature derivative of the curves R_S/R_N in **b**. The derivative curves are smoothed. **d** The maxima of curves from **c** are normalized to 1 respectively.

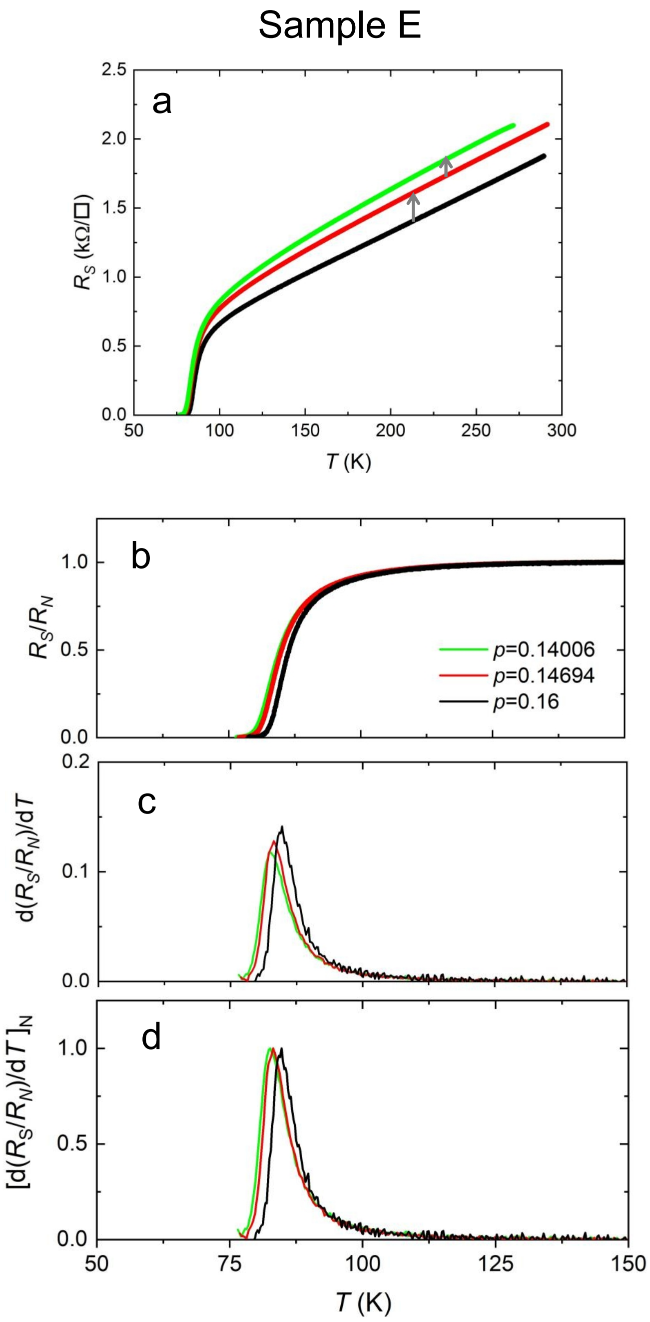

Figure 5.5: **Derivative and 2D superconductivity in underdoped region.** **a** Temperature dependence of sheet resistance curves $R_S(T)$ of 1 u.c. BSCCO sample labelled E from 50 K to 300 K. The black curve shows the optimal doping level, and the grey arrows from left to right indicate the order of doping. **b** Temperature dependence of the normalised sheet resistance R_S/R_N on the same sample as **a** from 50 K to 150 K. $R_N(T) = R_N(0) + aT - bT^2$ (a and b are constants). **c** Temperature derivative of the curves R_S/R_N in **b**. The derivative curves are smoothed. **d** The maxima of curves from **c** are normalized to 1 respectively.

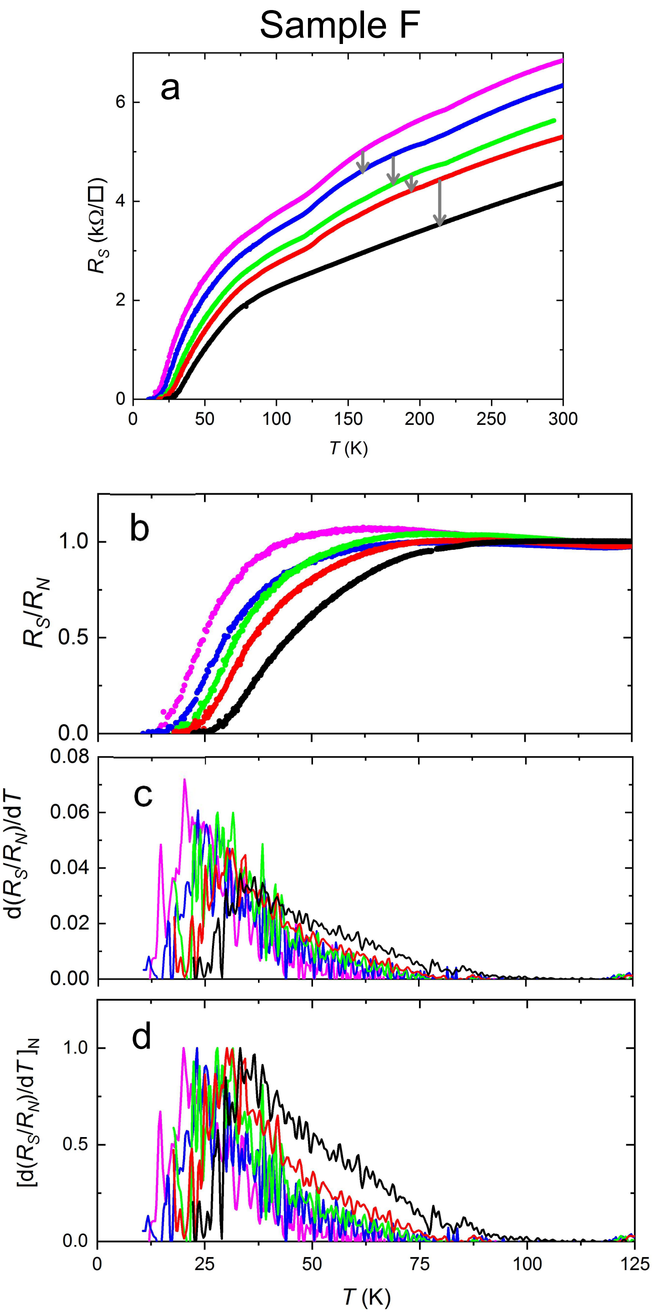

Figure 5.6: **Derivative and 2D superconductivity in highly underdoped region.** **a** Temperature dependence of sheet resistance curves $R_S(T)$ of 1 u.c. BSCCO sample labelled F from 0 to 300 K. The grey arrows from left to right indicate the order of doping. **b** Temperature dependence of the normalised sheet resistance R_S/R_N on the same sample as in **a** from 0 to 125 K. $R_N(T) = R_N(0) + aT - bT^2$ (a and b are constants). **c** Temperature derivative of the curves R_S/R_N in **b**. The curves are smoothed. **d** The maxima of curves from **c** are normalized to 1 respectively.

5.2.3 Discussion

From the earlier analysis we have extracted Δ_T and Δ_n for our samples as a function of doping. These quantities are plotted in Fig. 5.7 **b** and **c**. Below we list the principal conclusions from this analysis.

1) The first observation is already well-known from various and numerous earlier experiments, the underdoped and overdoped region of the the phase diagram of 2D-BSCCO are fundamentally different. Though the dome for the critical temperature roughly symmetrically decreases on each side of the optimal doping value, this does not indicate a symmetric behaviour for the fluctuation regime in our case.

2) As seen from both Fig. 5.7 **b** and **c**, fluctuations appear well above the critical temperature in the underdoped region, and the temperature range above which they appear with respect to T_C actually *increases* even as doping and T_C decrease.

3) In the overdoped region however, it can be seen in Fig. 5.7 **b** and **c** that as T_C decreases with increasing doping, the temperature where fluctuations appear also *decreases*, and appears to do so more and more as doping increases.

4) As discussed in the introduction to the chapter, fluctuations can provide precious information on the nature of the underlying superconducting state. In particular here we would like to concentrate on two aspects.

Firstly Δ_T andΔ_n increase by a factor of 5 to 6 as doping decreases from optimal to the underdoped limit. This implies that the temperature range over which fluctuations exist increases sharply. A possible explanation for such a dramatic increase issues from our measurements of the SIT in underdoped 2D-BSCCO (Chapter 3). These imply a bosonic transition where strongly bound Cooper pairs exist on both sides of the SIT and also above T_C. An open question is to determine whether Cooper pairs exists well above T_c even at higher doping levels close to the optimal. Indeed, **one** explanation for the appearance of the pseudo-gap in cuprates, which has been put forward in several papers [163, 164, 165], is the presence of strongly bound incoherent Cooper pairs in the normal state. The superconducting state is then reached through phase coherence of the pre-existing Cooper pairs. The fluctuations measured above T_c are then phase fluctuations of the superconducting wave function. We should however mention that, as noted is several studies [160, 166, 167, 168, 150], the temperature range for which superconducting fluctuations are measured above T_c is far lower than the temperatures at which the opening of the pseudo-gap is measured in spectroscopic experiments.

Secondly Δ_T andΔ_n remain roughly constant as doping increases from the optimal to the overdoped part of the phase diagram, even though T_C decreases. Many previous works, both theoretical and experimental (see for example [169]) assert that the overdoped part of the phase diagram corresponds to a ‘normal’ Fermi liquid. Our observations indicate that the associated fluctuation regime could correspond to fluctuations expected in a weakly coupled BCS superconductor where phase and amplitude coherence switch on simultaneously.

5) Finally, the above implies that these two regimes merge near the optimal doping. One possibility of such a scenario is provided by the BEC-BCS transition recently seen

[170] in ultra-cold atomic systems which permit the tuning of the interaction strength through an applied magnetic field. Justifying such a scenario for high Tc superconductivity would need a microscopic explanation concerning interaction strengths and their variation with doping and carrier concentration. It should also be noted [164] that the pseudogap region can be interpreted as a region between the BCS-like overdoped region and a BEC-like region which however is not attained in reality.

To conclude, it is important to point out that many theories for the existence of the pseudogap region have been established, most of them being rooted in the physics of doped Mott insulators. Notably, gaps associated to ordering (charge or spin) have been observed in high-T_c superconductors [169, 171, 172] and these gaps are thought to be related to, or responsible for, the pseudogap. It is not possible at this point to give a comprehensive explanation of our observations. However intriguing possibilities are raised by the spectacular change in fluctuation regime that we observe and it has been our endeavour to consider these.

5.3 Conclusion

In this chapter we have concentrated on the fluctuations and the HT part. We show with a number of samples (with various degrees of ihomogeneity, which does not have a big impact on the HT part of the transition) that the fluctuation regime in the underdoped part of the phase diagram is fundamentally different from that in the part where $p > 0.19$. We discussed the possible behaviour of Cooper pairs related to our experimental results, as well as one existing theoretical explanation (BEC-BCS transition).

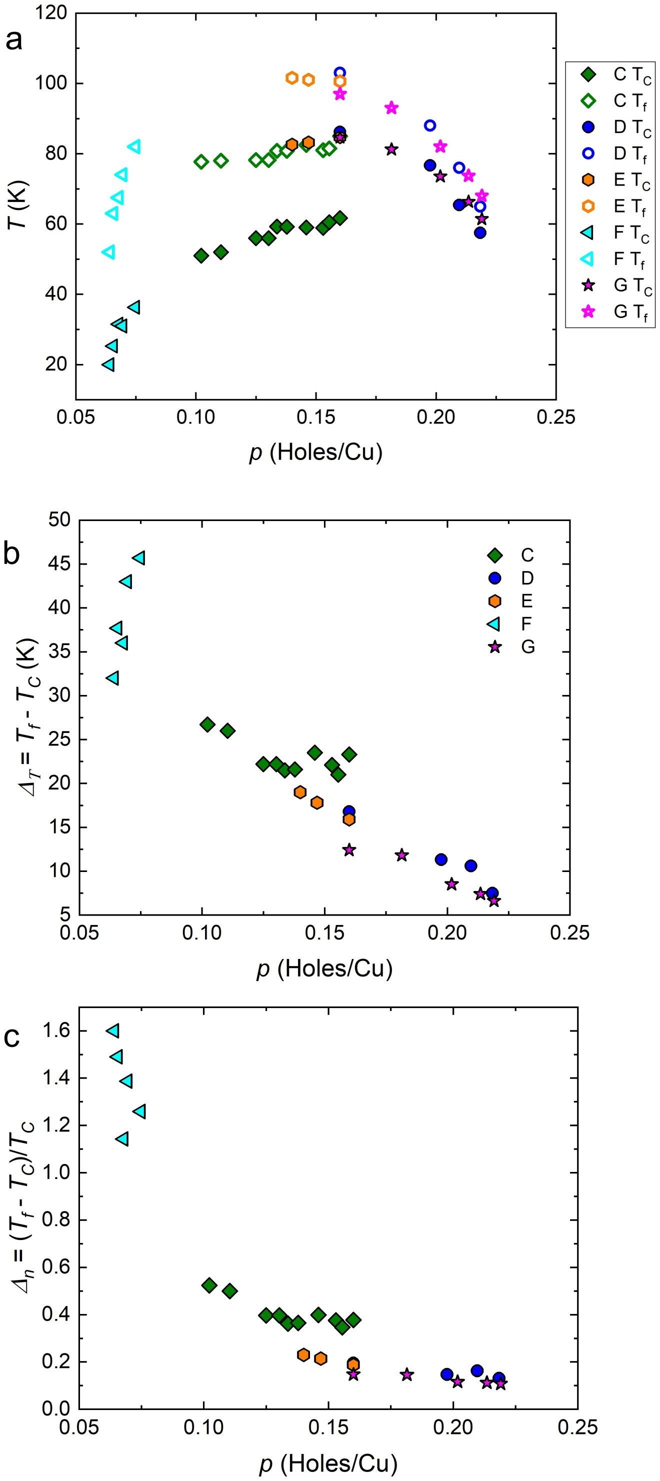

Figure 5.7: **a** Phase diagram of one u.c. BSCCO-2212 as a function of doping, T_C and T_f. **b** Doping dependence of Δ_T on five one u.c. BSCCO-2212 samples. **c** Doping dependence of Δ_n.

Conclusion

In this thesis, we studied the physics of one unit-cell (2D) BSCCO-2212 with innovative techniques for sample fabrication and electrostatic doping. We concentrated on the establishment of Superconductor-Insulator transition (SIT), and subsequently the 2D characters related with the purpose of investigating the role of fluctuations.

Firstly, a great number of one unit-cell BSCCO-2212 samples, with lateral dimensions of the order of 100 μm, were fabricated on soda-lime glass substrate by using anodic bonding method. The samples used for investigating the SIT, were first put into the oven in air for annealing to make them highly underdoped. And about 70 nm-thick of gold contacts in a van der Pauw configuration were thermally evaporated through shadow stencil masks previously aligned on the samples in the clean room. Then transport measurements, such as temperature dependence of sheet resistance measurements and Hall measurements, were carried out under a vacuum circumstance of 10^{-6} mbar.

The doping level was tuned by an effective and reversible electrostatic doping method, which we call space charge doping method. the SIT transition was revealed in one unit-cell BSCCO-2212 sample with by space charge doping. We determined the related critical parameters and developed a reliable way to estimate doping in the non-superconducting region, a crucial and central problem in these materials. Finite-size scaling analysis yields a critical doping of 0.057 holes/Cu, a critical resistance of ~6.85 kΩ and a scaling exponent product $\nu z \sim 1.57$. These results, together with earlier work in other materials, provide a coherent picture of the superconductor-insulator transition and its bosonic nature in the underdoped regime of emerging superconductivity in high critical temperature superconductors.

In chapter 4 we investigated the effects of inhomogeneity and fluctuations on the optimally doped one u.c. BSCCO-2212 samples. We prepared the groundwork and confirmed both with simulations and with analysis of sheet resistance curves as well as their temperature derivative curves. We separated the derivative curves into higher temperature part (HT) and lower temperature part (LT) by the peak of the derivative curve. Then we investigated how the derivative curve can tell us about inhomogeneity in its LT part and about fluctuations in the HT part. We did also a small analysis of the effect of inhomogeneity by comparing homogeneous and inhomogeneous samples on the one hand and an homogeneous sample in which we introduce inhomogeneity in the form of an ordered network of non-superconducting regions.

Finally in chapter 5, we focused on the effects of fluctuations and the HT part of the derivative curve. We presented with 5 one u.c. BSCCO-2212 samples (with 2 on the overdoped side, and 3 on the underdoped side) that the fluctuation regime in the underdoped part of the phase diagram is fundamentally different from that in the part where $p\ > 0.19$. We established this using the extent of the HT part of the derivative peak (extent from T_C to T_f as shown in chapter 5) plotted as a function of the doping. We then discussed the difference in the fluctuation regime may caused by the different nature of the superconducting transition. At $p\ < 0.19$, it seems that fluctuations extend over a big temperature range which seems to increase as doping and critical temperature decrease. At $p\ > 0.19$, the fluctuation temperature range seems to be constant even though T_c decreases again. This latter one is compatible with a more common scenario where amplitude fluctuations are present in a limited region above the transition. While the doping induced SIT established in this thesis is compatible with a scenario where the SIT is a boson transition where Cooper pairs existing at temperature much higher than T_c become phase coherent when superconductivity appears. The large domain of existence of fluctuations much above T_c in the underdoped part of the phase diagram can be understood in this scenario.

Finally such different regimes could be imagined in the light of BEC-BCS transition discussed in the introduction, though it is not generally thought at this time that high Tc superconductivity could be the system where such a transition could be observed.

Bibliography

[1] M. Thinkham. Introduction To Superconductivity, 1996.

[2] V. L. Ginzburg and L. D. Landau. On the Theory of Superconductivity, 2009.

[3] J. R. Schrieffer. Theory of superconductivity. *Theory Supercond.*, pages 1–332, 1957.

[4] J.G. Bednorz and K.A. Müller. Possible highT c superconductivity in the Ba−La−Cu−O system. *Zeitschrift für Physik B Condensed MatterSP*, 64:189—-193, 1986.

[5] N. Reyren, S. Thiel, A. D. Caviglia, L. Fitting Kourkoutis, G. Hammerl, C. Richter, C. W. Schneider, T. Kopp, A.-S. Rüetschi, D. Jaccard, M. Gabay, D. A. Muller, J.-M. Triscone, and J. Mannhart. Superconducting interfaces between insulating oxides. *Science*, 317(5842):1196–1199, 2007.

[6] A. Gozar, G. Logvenov, L. Fitting Kourkoutis, A. T. Bollinger, L. A. Giannuzzi, D. A. Muller, and I. Bozovic. High-temperature interface superconductivity between metallic and insulating copper oxides. *Nature*, 455(7214):782–785, Oct 2008.

[7] Matthew P. A. Fisher, G. Grinstein, and S. M. Girvin. Presence of quantum diffusion in two dimensions: Universal resistance at the superconductor-insulator transition. *Phys. Rev. Lett.*, 64:587–590, Jan 1990.

[8] Allen M. Goldman and Nina Marković. Superconductor-insulator transitions in the two-dimensional limit. *Physics Today*, 51(11):39–44, 1998.

[9] A. M. Goldman. Superconductor-insulator transitions. *International Journal of Modern Physics B*, 24(20n21):4081–4101, 2010.

[10] Yen-Hsiang Lin, J. Nelson, and A.M. Goldman. Superconductivity of very thin films: The superconductor–insulator transition. *Physica C: Superconductivity and its Applications*, 514:130–141, 2015. Superconducting Materials: Conventional, Unconventional and Undetermined.

[11] Yoichi Kamihara, Hidenori Hiramatsu, Masahiro Hirano, Ryuto Kawamura, Hiroshi Yanagi, Toshio Kamiya, and Hideo Hosono. Iron-based layered superconductor: Laofep. *Journal of the American Chemical Society*, 128(31):10012—10013, August 2006.

[12] M. M. Qazilbash, J. J. Hamlin, R. E. Baumbach, Lijun Zhang, D. J. Singh, M. B. Maple, and D. N. Basov. Electronic correlations in the iron pnictides. *Nature Physics*, 5(9):647–650, Jul 2009.

[13] Davide Costanzo, Sanghyun Jo, Helmuth Berger, and Alberto F Morpurgo. Gate-induced superconductivity in atomically thin mos2 crystals. *Nature nanotechnology*, 11(4):339—344, April 2016.

[14] Qing-Yan Wang, Zhi Li, Wen-Hao Zhang, Zuo-Cheng Zhang, Jin-Song Zhang, Wei Li, Hao Ding, Yun-Bo Ou, Peng Deng, Kai Chang, Jing Wen, Can-Li Song, Ke He, Jin-Feng Jia, Shuai-Hua Ji, Ya-Yu Wang, Li-Li Wang, Xi Chen, Xu-Cun Ma, and Qi-Kun Xue. Interface-Induced High-Temperature Superconductivity in Single Unit-Cell FeSe Films on $SrTiO_3$. *Chinese Physics Letters*, 29(3):037402, 2012.

[15] Yuan Cao, Valla Fatemi, Shiang Fang, Kenji Watanabe, Takashi Taniguchi, Efthimios Kaxiras, and Pablo Jarillo-Herrero. Unconventional superconductivity in magic-angle graphene superlattices. *Nature*, 556(7699):43–50, Mar 2018.

[16] T. Uchihashi. Two-dimensional superconductors with atomic-scale thickness. *Supercond. Sci. Technol.*, 30(1):1–39, 2017.

[17] A. Shalnikov. Superconducting thin films. *Nature*, 36(1):316, 1938.

[18] J. M. Graybeal and M. R. Beasley. Localization and interaction effects in ultrathin amorphous superconducting films. *Phys. Rev. B*, 29(9):4167–4169, 1984.

[19] B. G. Orr, H. M. Jaeger, and A. M. Goldman. Local superconductivity in ultrathin sn films. *Phys. Rev. B*, 32:7586–7589, 1985.

[20] H. M. Jaeger, D. B. Haviland, A. M. Goldman, and B. G. Orr. Threshold for superconductivity in ultrathin amorphous gallium films. *Phys. Rev. B*, 34:4920–4923, Oct 1986.

[21] Yu Saito, Tsutomu Nojima, and Yoshihiro Iwasa. Highly-crystalline 2D superconductors. *arXiv*, 16094, 2016.

[22] Fong-Chi Hsu, Jiu-Yong Luo, Kuo-Wei Yeh, Ta-Kun Chen, Tzu-Wen Huang, Phillip M. Wu, Yong-Chi Lee, Yi-Lin Huang, Yan-Yi Chu, Der-Chung Yan, and Maw-Kuen Wu. Superconductivity in the PbO-type structure α-FeSe. *Proceedings of the National Academy of Sciences*, 105(38):14262–14264, 2008.

[23] Jian-Feng Ge, Zhi-Long Liu, Canhua Liu, Chun-Lei Gao, Dong Qian, Qi-Kun Xue, Ying Liu, and Jin-Feng Jia. Superconductivity above 100 K in single-layer FeSe films on doped SrTiO3. *Nat. Mater.*, 14(3):285–289, 2015.

[24] Jerzy Mizia and Grzegorz Górski. Chapter 10 - itinerant superconductivity. In Jerzy Mizia and Grzegorz Górski, editors, *Models of Itinerant Ordering in Crystals*, pages 227–285. Elsevier Science Ltd, Oxford, 2007.

[25] M. K. Wu, J. R. Ashburn, C. J. Torng, P. H. Hor, R. L. Meng, L. Gao, Z. J. Huang, Y. Q. Wang, and C. W. Chu. Superconductivity at 93 K in a new mixed-phase Y-Ba-Cu-O compound system at ambient pressure. *Phys. Rev. Lett.*, 58:908–910, Mar 1987.

[26] Shinobu Hikami, Takashi Hirai, and Seiichi Kagoshima. High Transition Temperature Superconductor: Y-Ba-Cu Oxide. *Japanese Journal of Applied Physics*, 26(Part 2, No. 4):L314–L315, apr 1987.

[27] H. M. Duan, L. Lu, X. M. Wang, S. Y. Lin, and D. L. Zhang. Hall effect of the high Tc superconducting Y-Ba-Cu-O compound. *Solid State Communications*, 64(4):489–491, 1987.

[28] T. Terashima, K. Shimura, Y. Bando, Y. Matsuda, A. Fujiyama, and S. Komiyama. Superconductivity of one-unit-cell thick $YBa_2Cu_3O_7$ thin film. *Phys. Rev. Lett.*, 67:1362–1365, 1991.

[29] P. J. M. Wöltgens, C. Dekker, R. H. Koch, B. W. Hussey, and A. Gupta. Finite-size effects on the vortex-glass transition in thin $YBa_2Cu_3O_{7-\delta}$ films.

[30] H. Maeda, Y. Tanaka, M. Fukutomi, and T. Asano. A New High-TcOxide Superconductor without a Rare Earth Element. *Japanese Journal of Applied Physics*, 27:209–210, feb 1988.

[31] Z. Z. Sheng and A. M. Hermann. Bulk superconductivity at 120 K in the Tl–Ca/Ba–Cu–O system. 332:138–139, 1988.

[32] D. Jiang, T. Hu, L. You, Q. Li, A. Li, H. Wang, G. Mu, Z. Chen, H. Zhang, G. Yu, J. Zhu, Q. Sun, C. Lin, H. Xiao, X. Xie, and M. Jiang. High-T c superconductivity in ultrathin Bi 2 Sr 2 CaCu 2 O 8+x down to half-unit-cell thickness by protection with graphene. *Nat. Commun.*, 5:1–6, 2014.

[33] A. T. Bollinger and I. Božović. Two-dimensional superconductivity in the cuprates revealed by atomic-layer-by-layer molecular beam epitaxy. *Supercond. Sci. Technol.*, 29(10), 2016.

[34] H. Eschrig. High-tc superconductors: Electronic structure. In *Encyclopedia of Materials: Science and Technology*, pages 1–10. Elsevier, Oxford, 2004.

[35] N. Barisic, M. K. Chan, Y. Li, G. Yu, X. Zhao, M. Dressel, A. Smontara, and M. Greven. Universal sheet resistance and revised phase diagram of the cuprate high-temperature superconductors. *Proc. Natl. Acad. Sci. U. S. A.*, 110(30):12235–12240, 2013.

[36] B. Keimer, S. A. Kivelson, M. R. Norman, S. Uchida, and J. Zaanen. From quantum matter to high-temperature superconductivity in copper oxides. *Nature*, 518(7538):179–186, 2015.

[37] A R Schmidt, K Fujita, E-A Kim, M J Lawler, H Eisaki, S Uchida, D-H Lee, and J C Davis. Electronic structure of the cuprate superconducting and pseudogap phases from spectroscopic imaging STM. *New Journal of Physics*, 13(6):065014, jun 2011.

[38] M. R. Norman and C. Pépin. The electronic nature of high temperature cuprate superconductors. *Reports on Progress in Physics*, 66(10):1547–1610, Sep 2003.

[39] Nikolay Plakida. Antiferromagnetism in Cuprate Superconductors. In *High-Temperature Cuprate Superconductors: Experiment, Theory, and Applications*, pages 51–120. Springer Berlin Heidelberg, 2010.

[40] Masatoshi Imada, Atsushi Fujimori, and Yoshinori Tokura. Metal-insulator transitions. *Rev. Mod. Phys.*, 70:1039–1263, Oct 1998.

[41] L.H.C.M. Nunes, A.W. Teixeira, and E.C. Marino. Antiferromagnetic phase diagram of the cuprate superconductors. *Solid State Communications*, 251:5–9, 2017.

[42] S Hüfner, M A Hossain, A Damascelli, and G A Sawatzky. Two gaps make a high-temperature superconductor? *Reports on Progress in Physics*, 71(6):062501, May 2008.

[43] D. Fournier, G. Levy, Y. Pennec, J. L. McChesney, A. Bostwick, E. Rotenberg, R. Liang, W. N. Hardy, D. A. Bonn, I. S. Elfimov, and A. Damascelli. Loss of nodal quasiparticle integrity in underdoped YBa 2 Cu 3 O 6+x. *Nat. Phys.*, 6(11):905–911, 2010.

[44] M. A. Hossain, J. D.F. Mottershead, D. Fournier, A. Bostwick, J. L. McChesney, E. Rotenberg, R. Liang, W. N. Hardy, G. A. Sawatzky, I. S. Elfimov, D. A. Bonn, and A. Damascelli. In situ doping control of the surface of higherature superconductors. *Nat. Phys.*, 4(7):527–531, 2008.

[45] M.R. Presland, J.L. Tallon, R.G. Buckley, R.S. Liu, and N.E. Flower. General trends in oxygen stoichiometry effects on Tc in Bi and Tl superconductors. *Physica C: Superconductivity*, 176(1):95–105, 1991.

[46] C. M. Varma, P. B. Littlewood, S. Schmitt-Rink, E. Abrahams, and A. E. Ruckenstein. Phenomenology of the normal state of Cu-O high-temperature superconductors. *Phys. Rev. Lett.*, 63:1996–1999, Oct 1989.

[47] R. M. Hazen, C. T. Prewitt, R. J. Angel, N. L. Ross, L. W. Finger, C. G. Hadidiacos, D. R. Veblen, P. J. Heaney, P. H. Hor, R. L. Meng, Y. Y. Sun, Y. Q. Wang, Y. Y. Xue, Z. J. Huang, L. Gao, J. Bechtold, and C. W. Chu. Superconductivity in the high-T_c Bi-Ca-Sr-Cu-O system: Phase identification. *Phys. Rev. Lett.*, 60:1174–1177, Mar 1988.

[48] Apoorv Jindal, DIgambar A. Jangade, Nikhil Kumar, Jaykumar Vaidya, Ipsita Das, Rudheer Bapat, Jayesh Parmar, Bhagyashree A. Chalke, Arumugam Thamizhavel, and Mandar M. Deshmukh. Growth of high-quality Bi2Sr2 CaCu2O8+δ whiskers and electrical properties of resulting exfoliated flakes. *Sci. Rep.*, 7(1):1–8, 2017.

[49] Y He, TS Nunner, PJ Hirschfeld, and HP Cheng. Local electronic structure of near oxygen dopants: a window on the high-Tc pairing mechanism. *Physical review letters*, 96(19):197002, May 2006.

[50] P Badica, K Togano, S Awaji, K Watanabe, and H Kumakura. Review on Bi–Sr–Ca–Cu–O whiskers. *Superconductor Science and Technology*, 19(10):R81–R99, aug 2006.

[51] K. S. Novoselov, A. K. Geim, S. V. Morozov, D. Jiang, Y. Zhang, S. V. Dubonos, I. V. Grigorieva, and A. A. Firsov. Electric Field Effect in Atomically Thin Carbon Films. *Science*, 306(5696):666–669, 2004.

[52] X. Wang, L.X. You, D.K. Liu, C.T. Lin, X.M. Xie, and M.H. Jiang. Thin-film-like BSCCO single crystals made by mechanical exfoliation. *Physica C: Superconductivity*, 474:13–17, 2012.

[53] Yijun Yu, Liguo Ma, Peng Cai, Ruidan Zhong, Cun Ye, Jian Shen, G D Gu, Xian Hui Chen, and Yuanbo Zhang. High-temperature superconductivity in monolayer Bi2Sr2CaCu2O8+δ. *Nature*, 575(7781):156–163, 2019.

[54] E. Arrigoni, E. Fradkin, and S. A. Kivelson. Mechanism of high-temperature superconductivity in a striped hubbard model. *Phys. Rev. B*, 69:214519, Jun 2004.

[55] E. Carlson, V. Emery, S. Kivelson, and D. Orgad. Concepts in high temperature superconductivity. 06 2002.

[56] Emanuel Maxwell. Isotope effect in the superconductivity of mercury. *Phys. Rev.*, 78:477–477, May 1950.

[57] Takashi Yanagisawa. Mechanism of high-temperature superconductivity in correlated-electron systems. *Condensed Matter*, 4(2), 2019.

[58] Patrick A. Lee, Naoto Nagaosa, and Xiao-Gang Wen. Doping a mott insulator: Physics of high-temperature superconductivity. *Rev. Mod. Phys.*, 78:17–85, Jan 2006.

[59] J. Orenstein and A. J. Millis. Advances in the physics of high-temperature superconductivity. *Science*, 288(5465):468–474, 2000.

[60] Jordens Robert, Niels Strohmaier, Kenneth Gu, Henning Moritz, and Tilman Esslinger. LETTERS A Mott insulator of fermionic atoms in an optical lattice. 455(September):1–5, 2008.

[61] J. Hubbard and Brian Hilton Flowers. Electron correlations in narrow energy bands. *Proceedings of the Royal Society of London. Series A. Mathematical and Physical Sciences*, 276(1365):238–257, 1963.

[62] Takeshi Nakanishi, Kunihiko Yamaji, and Takashi Yanagisawa. Variational monte carlo indications of d-wave superconductivity in the two-dimensional hubbard model. *Journal of the Physical Society of Japan*, 66(2):294–297, 1997.

[63] G. Logvenov, A. Gozar, and I. Bozovic. High-temperature superconductivity in a single copper-oxygen plane. *Science*, 326(5953):699–702, 2009.

[64] T. M. Hardy, J. P. Hague, J. H. Samson, and A. S. Alexandrov. Superconductivity in a hubbard-fröhlich model and in cuprates. *Phys. Rev. B*, 79:212501, Jun 2009.

[65] Astrid T. Rømer, Thomas A. Maier, Andreas Kreisel, Ilya Eremin, P. J. Hirschfeld, and Brian M. Andersen. Pairing in the two-dimensional hubbard model from weak to strong coupling. *Physical Review Research*, 2(1), Jan 2019.

[66] M. Aichhorn, E. Arrigoni, M. Potthoff, and W. Hanke. Antiferromagnetic to superconducting phase transition in the hole- and electron-doped hubbard model at zero temperature. *Phys. Rev. B*, 74:024508, Jul 2006.

[67] P. W. ANDERSON. The resonating valence bond state in la2cuo4 and superconductivity. *Science*, 235(4793):1196–1198, 1987.

[68] M Aichhorn and E Arrigoni. Weak phase separation and the pseudogap in the electron-doped cuprates. *Europhysics Letters (EPL)*, 72(1):117–123, oct 2005.

[69] David Sénéchal, P.-L. Lavertu, M.-A. Marois, and A.-M. S. Tremblay. Competition between antiferromagnetism and superconductivity in high-T_c cuprates. *Phys. Rev. Lett.*, 94:156404, Apr 2005.

[70] D. J. Scalapino. A common thread: The pairing interaction for unconventional superconductors. *Reviews of Modern Physics*, 84(4):1383–1417, Oct 2012.

[71] S. Raghu, S. A. Kivelson, and D. J. Scalapino. Superconductivity in the repulsive hubbard model: An asymptotically exact weak-coupling solution. *Phys. Rev. B*, 81:224505, Jun 2010.

[72] Takashi Yanagisawa. Crossover from weakly to strongly correlated regions in the two-dimensional hubbard model — off-diagonal wave function monte carlo studies of hubbard model ii —. *Journal of the Physical Society of Japan*, 85(11):114707, 2016.

[73] F. London. The λ-phenomenon of liquid helium and the bose-einstein degeneracy. *nat.*, 141(3571):643–644, apr 1938.

[74] *Bose-Einstein Condensation.* Cambridge University Press, 1995.

[75] Yuji Nakagawa, Yuichi Kasahara, Takuya Nomoto, Ryotaro Arita, Tsutomu Nojima, and Yoshihiro Iwasa. Gate-controlled bcs-bec crossover in a two-dimensional superconductor. *Science*, 372(6538):190–195, 2021.

[76] Vsevolod F Gantmakher and Valery T Dolgopolov. Superconductor-insulator quantum phase transition. *Physics-Uspekhi*, 53(1):1–49, jan 2010.

[77] D. M. Eagles. Possible pairing without superconductivity at low carrier concentrations in bulk and thin-film superconducting semiconductors. *Phys. Rev.*, 186:456–463, Oct 1969.

[78] Vadim M. Loktev, Rachel M. Quick, and Sergei G. Sharapov. Phase fluctuations and pseudogap phenomena. *Physics Reports*, 349(1):1–123, 2001.

[79] Mohit Randeria and Edward Taylor. Crossover from bardeen-cooper-schrieffer to bose-einstein condensation and the unitary fermi gas. *Annual Review of Condensed Matter Physics*, 5(1):209–232, 2014.

[80] AT Bollinger, G Dubuis, J Yoon, D Pavuna, J Misewich, and I Božović. Superconductor-insulator transition in la2 - xsrxcuo4 at the pair quantum resistance. *Nature*, 472(7344):458—460, April 2011.

[81] N. Marković, C. Christiansen, and A. M. Goldman. Thickness–magnetic field phase diagram at the superconductor-insulator transition in 2d. *Phys. Rev. Lett.*, 81:5217–5220, Dec 1998.

[82] Xiang Leng, Javier Garcia-Barriocanal, Shameek Bose, Yeonbae Lee, and A. M. Goldman. Electrostatic control of the evolution from a superconducting phase to an insulating phase in ultrathin yba$_2$cu$_3$o$_{7-x}$ films. *Phys. Rev. Lett.*, 107:027001, Jul 2011.

[83] H. Aubin, C. A. Marrache-Kikuchi, A. Pourret, K. Behnia, L. Bergé, L. Dumoulin, and J. Lesueur. Magnetic-field-induced quantum superconductor-insulator transition innb0.15si0.85. *Physical Review B*, 73(9), Mar 2006.

[84] Myles A. Steiner, Nicholas P. Breznay, and Aharon Kapitulnik. Approach to a superconductor-to-bose-insulator transition in disordered films. *Phys. Rev. B*, 77:212501, Jun 2008.

[85] V. F. Gantmakher, S. N. Ermolov, G. E. Tsydynzhapov, A. A. Zhukov, and T. I. Baturina. Suppression of 2d superconductivity by the magnetic field: Quantum corrections vs. the superconductor-insulator transition. *Journal of Experimental and Theoretical Physics Letters*, 77(8):424–428, Apr 2003.

[86] N E Hussey. Phenomenology of the normal state in-plane transport properties of high-tccuprates. *Journal of Physics: Condensed Matter*, 20(12):123201, Feb 2008.

[87] Jan Zaanen. Planckian dissipation, minimal viscosity and the transport in cuprate strange metals. *SciPost Physics*, 6(5), May 2019.

[88] D. Pelc, M. J. Veit, C. J. Dorow, Y. Ge, N. Barišić, and M. Greven. Resistivity phase diagram of cuprates revisited. *Phys. Rev. B*, 102:075114, Aug 2020.

[89] Yoichi Ando, Seiki Komiya, Kouji Segawa, S. Ono, and Y. Kurita. Electronic phase diagram of high-T_c cuprate superconductors from a mapping of the in-plane resistivity curvature. *Phys. Rev. Lett.*, 93:267001, Dec 2004.

[90] J Custers, P Gegenwart, H Wilhelm, K Neumaier, Y Tokiwa, O Trovarelli, C Geibel, F Steglich, C Pépin, and P Coleman. The break-up of heavy electrons at a quantum critical point. *Nature*, 424(6948):524—527, July 2003.

[91] N. E. Hussey. *Normal State Transport Properties*, pages 399–425. Springer New York, New York, NY, 2007.

[92] A. Kaminski, S. Rosenkranz, H. M. Fretwell, Z. Z. Li, H. Raffy, M. Randeria, M. R. Norman, and J. C. Campuzano. Crossover from coherent to incoherent electronic excitations in the normal state of $\mathrm{bi_2sr_2cacu_2o_{8+\delta}}$. *Phys. Rev. Lett.*, 90:207003, May 2003.

[93] S. Nakamae, K. Behnia, N. Mangkorntong, M. Nohara, H. Takagi, S. J. C. Yates, and N. E. Hussey. Electronic ground state of heavily overdoped nonsuperconducting $\mathrm{la}_{2-x}\mathrm{sr}_x\mathrm{cuo}_4$. *Phys. Rev. B*, 68:100502, Sep 2003.

[94] Edoardo Sterpetti, Johan Biscaras, Andreas Erb, and Abhay Shukla. Comprehensive phase diagram of two-dimensional space charge doped bi2sr2cacu2o8+x. *Nature Communications*, 8, 12 2017.

[95] S. Ono, Seiki Komiya, and Yoichi Ando. Strong charge fluctuations manifested in the high-temperature hall coefficient of high-T_c cuprates. *Phys. Rev. B*, 75:024515, Jan 2007.

[96] I. Tsukada and S. Ono. Negative hall coefficients of heavily overdoped $\mathrm{la}_{2-x}\mathrm{sr}_x\mathrm{Cuo}_4$. *Phys. Rev. B*, 74:134508, Oct 2006.

[97] Adrian Balan, Rakesh Kumar, Mohamed Boukhicha, Olivier Beyssac, Jean-Claude Bouillard, Dario Taverna, William Sacks, Massimiliano Marangolo, Emanuelle Lacaze, Roger Gohler, Walter Escoffier, Jean-Marie Poumirol, and Abhay Shukla.

Anodic bonded graphene. *Journal of Physics D: Applied Physics*, 43(37):374013, sep 2010.

[98] Karim Gacem, Mohamed Boukhicha, Zhesheng Chen, and Abhay Shukla. High quality 2d crystals made by anodic bonding: a general technique for layered materials. *Nanotechnology*, 23(50):505709, nov 2012.

[99] Zhesheng Chen, Karim Gacem, Mohamed Boukhicha, Johan Biscaras, and Abhay Shukla. Anodic bonded 2d semiconductors: from synthesis to device fabrication. *Nanotechnology*, 24(41):415708, sep 2013.

[100] Johan Biscaras, Zhesheng Chen, Andrea Paradisi, and Abhay Shukla. Onset of two-dimensional superconductivity in space charge doped few-layer molybdenum disulfide. *Nature Communications*, 6:8826, November 2015.

[101] H Mehrer, A W Imre, and E Tanguep-Nijokep. Diffusion and ionic conduction in oxide glasses. *Journal of Physics: Conference Series*, 106:012001, mar 2008.

[102] George Wallis and Daniel I. Pomerantz. Field assisted glass-metal sealing. *Journal of Applied Physics*, 40(10):3946–3949, 1969.

[103] Abhay Shukla, Rakesh Kumar, Javed Mazher, and Adrian Balan. Graphene made easy: High quality, large-area samples. *Solid State Communications*, 149(17):718–721, 2009.

[104] G. Binnig, C. F. Quate, and Ch. Gerber. Atomic force microscope. *Phys. Rev. Lett.*, 56:930–933, Mar 1986.

[105] B. Cappella and G. Dietler. Force-distance curves by atomic force microscopy. *Surface Science Reports*, 34(1):1–104, 1999.

[106] L. J. van der PAUW. *A METHOD OF MEASURING SPECIFIC RESISTIVITY AND HALL EFFECT OF DISCS OF ARBITRARY SHAPE*, pages 174–182.

[107] F. S. Oliveira, R. B. Cipriano, F. T. da Silva, E. C. Romão, and C. A.M. dos Santos. Simple analytical method for determining electrical resistivity and sheet resistance using the van der Pauw procedure. *Sci. Rep.*, 10(1):1–8, 2020.

[108] Winston K. Chan. On the calculation of the geometric factor in a van der pauw sheet resistance measurement. *Review of Scientific Instruments*, 71(10):3964–3965, 2000.

[109] S. Badoux, W. Tabis, F. Laliberté, G. Grissonnanche, B. Vignolle, D. Vignolles, J. Béard, D. A. Bonn, W. N. Hardy, R. Liang, and et al. Change of carrier density at the pseudogap critical point of a cuprate superconductor. *Nature*, 531(7593):210–214, Feb 2016.

[110] Edoardo Sterpetti, Johan Biscaras, Andreas Erb, and Abhay Shukla. Crossover to strange metal phase: quantum criticality in one unit cell $\mathrm{bi}_2\mathrm{sr}_2\mathrm{cacu}_2\mathrm{o}_{x+8}$. *Journal of Physics: Condensed Matter*, 32(4):045601, oct 2019.

[111] Andrea Paradisi, Johan Biscaras, and Abhay Shukla. Space charge induced electrostatic doping of two-dimensional materials: Graphene as a case study. *Applied Physics Letters*, 107(14):143103, 2015.

[112] Guy Dubuis, Yizhak Yacoby, Hua Zhou, Xi He, Anthony T. Bollinger, Davor Pavuna, Ron Pindak, and Ivan Božović. Oxygen displacement in cuprates under ionic liquid field-effect gating. *Scientific Reports*, 6(1), 8 2016.

[113] Fang Wang, Johan Biscaras, Andreas Erb, and Abhay Shukla. Superconductor-insulator transition in space charge doped one unit cell Bi2.1Sr1.9CaCu2O8+x. *Nature Communications*, 12:2926, 2021.

[114] S. L. Sondhi, S. M. Girvin, J. P. Carini, and D. Shahar. Continuous quantum phase transitions. *Rev. Mod. Phys.*, 69:315–333, Jan 1997.

[115] A. M. Goldman. Superconductor-insulator transitions in the two-dimensional limit. *Phys. E Low-Dimensional Syst. Nanostructures*, 18(1-3):1–6, 2003.

[116] Johan Biscaras, Nicolas Bergeal, A. Kushwaha, Thomas Wolf, A Rastogi, R. C. Budhani, and Jérome Lesueur. Two-dimensional superconductivity at a mott insulator/band insulator interface $\mathrm{LaTiO}_3/\mathrm{SrTiO}_3$. *Nature Communications*, 1(7):89, 2010.

[117] J. Biscaras, N. Bergeal, S. Hurand, C. Feuillet-Palma, A. Rastogi, R. C. Budhani, M. Grilli, S. Caprara, and J. Lesueur. Multiple quantum criticality in a two-dimensional superconductor. *Nat. Mater.*, 12(6):542–548, 2013.

[118] Nicolas Doiron-Leyraud, Mike Sutherland, S. Y. Li, Louis Taillefer, Ruixing Liang, D. A. Bonn, and W. N. Hardy. Onset of a boson mode at the superconducting critical point of underdoped YBa2Cu3Oy. *Phys. Rev. Lett.*, 97(20):14–17, 2006.

[119] J. T. Ye, S. Inoue, K. Kobayashi, Y. Kasahara, H. T. Yuan, H. Shimotani, and Y. Iwasa. Liquid-gated interface superconductivity on an atomically flat film. *Nat. Mater.*, 9(2):125–128, 2010.

[120] X. Leng, J. Garcia-Barriocanal, J. Kinney, B. Yang, Y. Lee, and A. M. Goldman. Electrostatic tuning of the electrical properties of YBa2Cu3O7-x using an ionic liquid. *Eur. Phys. J. Spec. Top.*, 222(5):1203–1215, 2013.

[121] Xiang Leng, Javier Garcia-Barriocanal, Boyi Yang, Yeonbae Lee, J. Kinney, and A. M. Goldman. Indications of an electronic phase transition in two-dimensional superconducting YBa 2Cu 3O 7-x thin films induced by electrostatic doping. *Physical Review Letters*, 108(6):1–5, 2012.

[122] Ana M. Perez-Muñoz, Pedro Schio, Roberta Poloni, Alejandro Fernandez-Martinez, Alberto Rivera-Calzada, Julio C. Cezar, Eduardo Salas-Colera, German R. Castro, Joseph Kinney, Carlos Leon, Jacobo Santamaria, Javier Garcia-Barriocanal, and Allen M. Goldman. In operando evidence of deoxygenation in ionic liquid gating of YBa2Cu3O7-X. *Proc. Natl. Acad. Sci. U. S. A.*, 114(2):215–220, 2016.

[123] M. Runde, J. L. Routbort, S. J. Rothman, K. C. Goretta, J. N. Mundy, X. Xu, and J. E. Baker. Tracer diffusion of oxygen in $\mathrm{bi_2sr_2cacu_2o_x}$. *Phys. Rev. B*, 45:7375–7382, Apr 1992.

[124] Hélène Raffy, Valentin Toma, Christopher Murrills, and Zhi Zhong Li. c-axis resistivity of Bi2Sr2CaCu2Oy thin films at various oxygen doping: Phase diagram and scaling law. *Physica C: Superconductivity*, 460-462(SPEC. ISS.):851–853, sep 2007.

[125] Z. Konstantinović, Z.Z. Li, and H. Raffy. Evolution of the resistivity of single-layer Bi2Sr1.6La0.4CuOy thin films with doping and phase diagram. *Physica C: Superconductivity*, 351(2):163–168, mar 2001.

[126] Panpan Zhou, Liyang Chen, Yue Liu, Ilya Sochnikov, Anthony T. Bollinger, Myung Geun Han, Yimei Zhu, Xi He, Ivan Bozović, and Douglas Natelson. Electron pairing in the pseudogap state revealed by shot noise in copper oxide junctions. *Nature*, 572(7770):493–496, 2019.

[127] Aharon Kapitulnik, Steven A. Kivelson, and Boris Spivak. Colloquium: Anomalous metals: Failed superconductors. *Reviews of Modern Physics*, 91(1):11002, 2019.

[128] Dung-Hai Lee, Ziqiang Wang, and Steven Kivelson. Quantum percolation and plateau transitions in the quantum hall effect. *Phys. Rev. Lett.*, 70:4130–4133, Jun 1993.

[129] Ying-Hong Li and S. Teitel. Finite-size scaling study of the three-dimensional classical xy model. *Phys. Rev. B*, 40:9122–9125, Nov 1989.

[130] Nicholas P. Breznay, Myles A. Steiner, Steven Allan Kivelson, and Aharon Kapitulnik. Self-duality and a Hall-insulator phase near the superconductor-to-insulator transition in indium-oxide films. *Proceedings of the National Academy of Sciences of the United States of America*, 113(2):280–285, 2016.

[131] K. M. Lang, V. Madhavan, J. E. Hoffman, E. W. Hudson, H. Eisaki, S. Uchida, and J. C. Davis. Imaging the granular structure of high-tc superconductivity in underdoped bi2sr2cacu2o8+δ. *Nature*, 415(6870):412–416, Jan 2002.

[132] V. L. Berezinsky. Destruction of Long-range Order in One-dimensional and Two-dimensional Systems Possessing a Continuous Symmetry Group. II. Quantum Systems. *Sov. Phys. JETP*, 34(3):610, 1972.

[133] J. M. Kosterlitz and D. J. Thouless. Ordering, metastability and phase transitions in two-dimensional systems. *J. Phys. C Solid State Phys.*, 6(7):1181–1203, 1973.

[134] J M Kosterlitz. The critical properties of the two-dimensional xy model. *Journal of Physics C: Solid State Physics*, 7(6):1046–1060, mar 1974.

[135] D. J. Bishop and J. D. Reppy. Study of the superfluid transition in two-dimensional ^{4}he films. *Phys. Rev. Lett.*, 40:1727–1730, Jun 1978.

[136] W. Dürr, M. Taborelli, O. Paul, R. Germar, W. Gudat, D. Pescia, and M. Landolt. Magnetic phase transition in two-dimensional ultrathin fe films on au(100). *Phys. Rev. Lett.*, 62:206–209, Jan 1989.

[137] A. M. Kadin, K. Epstein, and A. M. Goldman. Renormalization and the kosterlitz-thouless transition in a two-dimensional superconductor. *Phys. Rev. B*, 27:6691–6702, Jun 1983.

[138] R. W. Crane, N. P. Armitage, A. Johansson, G. Sambandamurthy, D. Shahar, and G. Grüner. Fluctuations, dissipation, and nonuniversal superfluid jumps in two-dimensional superconductors. *Phys. Rev. B*, 75:094506, Mar 2007.

[139] S. Misra, L. Urban, M. Kim, G. Sambandamurthy, and A. Yazdani. Measurements of the magnetic-field-tuned conductivity of disordered two-dimensional $mo_{43}ge_{57}$ and ino_x superconducting films: Evidence for a universal minimum superfluid response. *Phys. Rev. Lett.*, 110:037002, Jan 2013.

[140] L. Benfatto, C. Castellani, and T. Giamarchi. Broadening of the berezinskii-kosterlitz-thouless superconducting transition by inhomogeneity and finite-size effects. *Phys. Rev. B*, 80:214506, Dec 2009.

[141] P. G. Baity, Xiaoyan Shi, Zhenzhong Shi, L. Benfatto, and Dragana Popović. Effective two-dimensional thickness for the berezinskii-kosterlitz-thouless-like transition in a highly underdoped $\mathrm{la}_{2-x}\mathrm{sr}_x\mathrm{cuo}_4$. *Phys. Rev. B*, 93:024519, Jan 2016.

[142] Lara Benfatto, Claudio Castellani, and Thierry Giamarchi. *Berezinskii–Kosterlitz–Thouless Transition within the Sine-Gordon Approach: The Role of the Vortex-Core Energy*, pages 161–199.

[143] G. Venditti, J. Biscaras, S. Hurand, N. Bergeal, J. Lesueur, A. Dogra, R. C. Budhani, Mintu Mondal, John Jesudasan, Pratap Raychaudhuri, S. Caprara, and L. Benfatto. Nonlinear i-v characteristics of two-dimensional superconductors: Berezinskii-kosterlitz-thouless physics versus inhomogeneity. *Phys. Rev. B*, 100:064506, Aug 2019.

[144] Zoran Hadzibabic, Peter Krüger, Marc Cheneau, Baptiste Battelier, and Jean Dalibard. Berezinskii-Kosterlitz-Thouless Crossover in a Trapped Atomic Gas. *Nature*, 441:1118, 2006.

[145] Mintu Mondal, Sanjeev Kumar, Madhavi Chand, Anand Kamlapure, Garima Saraswat, G. Seibold, L. Benfatto, and Pratap Raychaudhuri. Role of the vortex-core energy on the berezinskii-kosterlitz-thouless transition in thin films of nbn. *Phys. Rev. Lett.*, 107:217003, Nov 2011.

[146] Anand Kamlapure, Mintu Mondal, Madhavi Chand, Archana Mishra, John Jesudasan, Vivas Bagwe, L. Benfatto, Vikram Tripathi, and Pratap Raychaudhuri. Measurement of magnetic penetration depth and superconducting energy gap in very thin epitaxial nbn films. *Applied Physics Letters*, 96(7):072509, 2010.

[147] TODOR MISHONOV and EVGENI PENEV. Thermodynamics of gaussian fluctuations and paraconductivity in layered superconductors. *International Journal of Modern Physics B*, 14(32):3831–3879, Dec 2000.

[148] G. Balestrino, A. Nigro, R. Vaglio, and M. Marinelli. Thermodynamic fluctuations in the 110-k bi-sr-ca-cu-o superconductor: Evidence for two-dimensional behavior. *Phys. Rev. B*, 39:12264–12266, Jun 1989.

[149] S. Caprara, M. Grilli, B. Leridon, and J. Lesueur. Extended paraconductivity regime in underdoped cuprates. *Phys. Rev. B*, 72:104509, Sep 2005.

[150] N. Coton, M. V. Ramallo, and F. Vidal. Critical temperatures for superconducting phase-coherence and condensation in la2-xsrxcuo4, 2013.

[151] B. I. Halperin and David R. Nelson. Resistive transition in superconducting films. *Journal of Low Temperature Physics*, 36(5-6):599–616, September 1979.

[152] S. Pan, Jared O'Neal, R. Badzey, C. Chamon, Hanjie Ding, J. Engelbrecht, Zhijun Wang, H. Eisaki, Shin-ichi Uchida, Anjan Gupta, K.-W Ng, Eric Hudson, Kristine Lang, and J. Davis. Microscopic electronic inhomogeneity in the high-tc superconductor bi2sr2cacu2o8+x. *Nature*, 413:282–285, 09 2001.

[153] B. Sacépé, C. Chapelier, T. I. Baturina, V. M. Vinokur, M. R. Baklanov, and M. Sanquer. Disorder-induced inhomogeneities of the superconducting state close to the superconductor-insulator transition. *Phys. Rev. Lett.*, 101:157006, Oct 2008.

[154] Kenjiro K. Gomes, Abhay N. Pasupathy, Aakash Pushp, Shimpei Ono, Yoichi Ando, and Ali Yazdani. Visualizing pair formation on the atomic scale in the high-tc superconductor bi2sr2cacu2o8+δ. *Nature*, 447(7144):569–572, May 2007.

[155] C. Carbillet, S. Caprara, M. Grilli, C. Brun, T. Cren, F. Debontridder, B. Vignolle, W. Tabis, D. Demaille, L. Largeau, K. Ilin, M. Siegel, D. Roditchev, and B. Leridon. Confinement of superconducting fluctuations due to emergent electronic inhomogeneities. *Phys. Rev. B*, 93:144509, Apr 2016.

[156] S Caprara, D Bucheli, N Scopigno, N Bergeal, J Biscaras, S Hurand, J Lesueur, and M Grilli. Inhomogeneous multi carrier superconductivity at LaXO3/SrTiO3(x

= al or ti) oxide interfaces. *Superconductor Science and Technology*, 28(1):014002, nov 2014.

[157] L. Benfatto, C. Castellani, and T. Giamarchi. Doping dependence of the vortex-core energy in bilayer films of cuprates. *Physical Review B*, 77(10), Mar 2008.

[158] Olivier Cyr-Choinière, R. Daou, Francis Laliberté, David LeBoeuf, Nicolas Doiron-Leyraud, J. Chang, J.-Q. Yan, J.-G. Cheng, J.-S. Zhou, J. B. Goodenough, and et al. Enhancement of the nernst effect by stripe order in a high-tc superconductor. *Nature*, 458(7239):743–745, Apr 2009.

[159] Nicolas Doiron-Leyraud, S. Lepault, O. Cyr-Choinière, B. Vignolle, G. Grissonnanche, F. Laliberté, J. Chang, N. Barišić, M. K. Chan, L. Ji, X. Zhao, Y. Li, M. Greven, C. Proust, and Louis Taillefer. Hall, seebeck, and nernst coefficients of underdoped hgba2cuo4+δ: Fermi-surface reconstruction in an archetypal cuprate superconductor. *Phys. Rev. X*, 3:021019, Jun 2013.

[160] M. S. Grbić, M. Požek, D. Paar, V. Hinkov, M. Raichle, D. Haug, B. Keimer, N. Barišić, and A. Dulčić. Temperature range of superconducting fluctuations above tc in yba2cu3o7$-\delta$ single crystals. *Physical Review B*, 83(14), Apr 2011.

[161] Chandra M Varma. Quantum-critical fluctuations in 2d metals: strange metals and superconductivity in antiferromagnets and in cuprates. *Reports on Progress in Physics*, 79(8):082501, jul 2016.

[162] Marcel Franz. Superconductivity: Importance of fluctuations. *Nature Physics*, 3:686–687, 10 2007.

[163] Øystein Fischer, Martin Kugler, Ivan Maggio-Aprile, Christophe Berthod, and Christoph Renner. Scanning tunneling spectroscopy of high-temperature superconductors. *Rev. Mod. Phys.*, 79:353–419, Mar 2007.

[164] Q. Chen, K. Levin, and J. Stajic. Applying bcs–bec crossover theory to high-temperature superconductors and ultracold atomic fermi gases (review article). *Low Temperature Physics*, 32(4):406–423, 2006.

[165] Nandini Trivedi, Yen Lee Loh, Karim Bouadim, and Mohit Randeria. Emergent granularity and pseudogap near the superconductor-insulator transition. *Journal of Physics: Conference Series*, 376:012001, jul 2012.

[166] N. Bergeal, Jerome Lesueur, M. Aprili, G. Faini, J. Contour, and B. Leridon. Pairing fluctuations in the pseudogap state of copper-oxide superconductors probed by the josephson effect. *NATURE PHYSICS*, 4:608–611, 08 2008.

[167] John Corson, Richard Mallozzi, J. Orenstein, James Eckstein, and Ivan Bozovic. Vanishing of phase coherence in underdoped bi2sr2cacu2o8+d. 10 1998.

[168] Yayu Wang, Lu Li, and N. P. Ong. Nernst effect in high-T_c superconductors. *Phys. Rev. B*, 73:024510, Jan 2006.

[169] Makoto Hashimoto, Inna M. Vishik, Rui-Hua He, Thomas P. Devereaux, and Zhi-Xun Shen. Energy gaps in high-transition-temperature cuprate superconductors. *Nature Physics*, 10(7):483–495, Jun 2014.

[170] Markus Greiner, Cindy A Regal, and Deborah S Jin. Emergence of a molecular bose-einstein condensate from a fermi gas. *Nature*, 426(6966):537—540, December 2003.

[171] B. Loret, N. Auvray, Y. Gallais, M. Cazayous, A. Forget, D. Colson, M.-H. Julien, I. Paul, M. Civelli, and A. Sacuto. Intimate link between charge density wave, pseudogap and superconducting energy scales in cuprates. *Nature Physics*, 15(8):771–775, Apr 2019.

[172] S. A. Kivelson, I. P. Bindloss, E. Fradkin, V. Oganesyan, J. M. Tranquada, A. Kapitulnik, and C. Howald. How to detect fluctuating stripes in the high-temperature superconductors. *Rev. Mod. Phys.*, 75:1201–1241, Oct 2003.